

FELIPE MACHINI MALACHIAS MARQUES

MODELING, SIMULATION AND CONTROL OF A GENERIC  
TILTING ROTOR MULTI-COPTER



FEDERAL UNIVERSITY OF UBERLÂNDIA  
SCHOOL OF MECHANICAL ENGINEERING

2018

FELIPE MACHINI MALACHIAS MARQUES

**MODELING, SIMULATION AND CONTROL OF A GENERIC TILTING ROTOR  
MULTI-COPTER**

**Master** Thesis presented to the  
Mechanical Engineering Graduate  
Program of the Federal University of  
Uberlândia, as a partial fulfillment of the  
requirements for the degree of **MASTER  
IN MECHANICAL ENGINEERING**

Focus Area: Solid Mechanics and  
Vibrations

Advisor: Prof. Dr. Leonardo Sanches

Co-advisor: Prof. Dr. Roberto Mendes  
Finzi Neto

Uberlândia – MG  
2018



SERVIÇO PÚBLICO FEDERAL  
MINISTÉRIO DA EDUCAÇÃO  
UNIVERSIDADE FEDERAL DE UBERLÂNDIA  
FACULDADE DE ENGENHARIA MECÂNICA  
PROGRAMA DE PÓS-GRADUAÇÃO EM ENGENHARIA  
MECÂNICA



**ALUNO:** Felipe Machini Malachias Marques

**NÚMERO DE MATRÍCULA:** 11612EMC006

**ÁREA DE CONCENTRAÇÃO:** Mecânica dos Sólidos e Vibrações

**LINHA DE PESQUISA:** Dinâmica de Sistemas Mecânicos

**PÓS-GRADUAÇÃO EM ENGENHARIA MECÂNICA:** NÍVEL MESTRADO

**TÍTULO DA DISSERTAÇÃO:**

***“Modeling, Simulation and Control of a  
Generic Tilting Rotor Multi-copter”***

**ORIENTADOR:** Prof. Dr. Leonardo Sanches

**CO-ORIENTADOR:** Prof. Dr. Roberto Mendes Finzi Neto

A Dissertação foi **APROVADA** em reunião pública, realizada na Sala 313 - Bloco 1M, Campus Santa Mônica, em 16 de março de 2018, às 14:00 horas, com a seguinte Banca Examinadora:

NOME	ASSINATURA
Prof. Dr. Leonardo Sanches	UFU
Prof. Dr. Roberto Mendes Finzi Neto	UFU
Prof. Dr. Rogério Sales Gonçalves	UFU
Prof. Dr. Edson Hideki Koroishi	UTFPR

Uberlândia, 16 de março de 2018

Dados Internacionais de Catalogação na Publicação (CIP)  
Sistema de Bibliotecas da UFU, MG, Brasil.

---

M357m    Marques, Felipe Machini Malachias, 1992-  
2018       Modeling, simulation and control of a generic tilting rotor multi-  
copter / Felipe Machini Malachias Marques. - 2018.  
112 f. : il.

Orientador: Leonardo Sanches.

Coorientador: Roberto Mendes Finzi Neto.

Dissertação (mestrado) - Universidade Federal de Uberlândia,  
Programa de Pós-Graduação em Engenharia Mecânica.

Disponível em: <http://dx.doi.org/10.14393/ufu.di.2018.1135>

Inclui bibliografia.

1. Engenharia mecânica - Teses. 2. Veículo aéreo não tripulado -  
Teses. 3. Rotor de inclinação - Teses. I. Sanches, Leonardo. II. Finzi  
Neto, Roberto Mendes. III. Universidade Federal de Uberlândia.  
Programa de Pós-Graduação em Engenharia Mecânica. IV. Título.

---

CDU: 621

Maria Salete de Freitas Pinheiro – CRB6/1262



*“You must not let your life run in the ordinary way; do something that nobody else has done, something that will dazzle the world. Show that God’s creative principle works in you” – Paramahansa Yogananda*

## Acknowledgments

This work is a result of years of hard working which initiated as a pioneering research project from the Federal University of Uberlândia Aeronautical Engineering undergraduate course on unmanned aerial system. The project was conducted by Prof Dr Leonardo Sanches and Prof Dr Roberto Mendes Finzi Neto to whom I express my gratitude for the opportunity, confidence and support through the project development.

After three years from the project beginning a vision has become true when the Aeronautical Engineering course direction has given a reserved place to develop our researches and experiments which now developed to the *Laboratório de Aeronaves Autônomas*. I also thank all the people involved who made it possible. Further, I show my gratitude to my research lab colleagues Ivan Tarifa, Matheus Amarante, Bruno Luiz Pereira and Douglas Lopes Silva for the support and teamwork and my classmates Marcelo Samora for his friendship from so many years.

To the Federal University of Uberlândia and the School of Mechanical Engineering of the opportunity to take this course and the mission to guide me through the scientific path and human development.

To the Brazilian research agency CNPq (National Council for Scientific and Technological Development) for the financial support.

Finally, I want to express my eternal gratitude to my family Pedro, Deisi, João Pedro and Maria Cleide for all the love they have given to me.

MARQUES, F. M. M. **Modeling, Simulation and Control of a Generic Til-rotor Multi-copter.** 2018, 99p. Master Thesis, Federal University of Uberlândia, Uberlândia – MG, Brazil

## Abstract

In general, standard multi-copters are classified as underactuated systems since their number of control inputs are insufficient to allow the control of position and orientation independently. In this context, this work deals with the dynamical modeling of a generic of a tilted rotor multi-copter aerial vehicle and the design of a trajectory tracking controller using modern control techniques. The dynamical model is developed using Newton-Euler equations of motion considering the aircraft as a six degrees of freedom rigid body and also assuming that each rotor is capable of two independent movements (tilt laterally and longitudinally) introducing more control inputs to the system.

Later, the equations of motion are linearized around the desired trimmed operating conditions, considering small perturbations, based on the mission application so that the linear modern control techniques can be applied. The control method applied is a Linear Quadratic Tracking (LQT) controller formulated as a servomechanism problem permitting the controller to be designed for different reference input signals based on their time differential equations. The dynamical model and control law were validated using Matlab/Simulink® environment assuming all the deriving non-linear effects caused by tilt actuation using as research object a real quadcopter model developed by the Laboratório de Aeronaves Autônomas from the Federal University of Uberlândia.

Finally, the stability conditions of the system are tested for different scenarios (tilt configurations and reference input signals) through pole and zeros mapping and time response analysis. The simulations have shown that the lateral tilt mechanism can be profitable for trajectory tracking applications once it improves the system controllability principally on the yaw dynamics. However, the tilt mechanism may be used wisely since their actuation amplifies the dynamical non-linear effects, such as the gyroscopic ones, which are not predicted by the linearized model and can make its response diverges.

---

Keywords: *Unmanned Aerial Vehicle, multi-copter, tilt rotor, Linear Quadratic Regulator*

MARQUES, F. M. M. **Modelagem Simulação e Controle de uma aeronave Multirrotora com Configuração *Tilt-rotor***. 2018, 99p. Dissertação de Mestrado, Universidade Federal de Uberlândia, Uberlândia – MG, Brasil

## Resumo

Em geral, aeronaves multirrotoras convencionais são classificadas como sistemas dinâmicos subatuados uma vez que seu número de variáveis de controle é insuficiente para permitir que posição e atitude sejam controladas de forma independente. Desta forma, este trabalho trata da modelagem dinâmica genérica de uma aeronave multirrotora com configuração *tilt-rotor* e a aplicação das técnicas de controle moderno de forma a viabilizar o sistema a seguir uma trajetória. A modelagem dinâmica é feita baseada nas equações do movimento de Newton-Euler considerando a aeronave como um corpo rígido com seis graus de liberdade e ainda assumindo que cada motor seja capaz de executar dois tipos de movimento independentes (lateralmente ou longitudinalmente) introduzindo mais sinais de controle ao sistema.

Em seguida, as equações do movimento são linearizadas utilizando a teoria de pequenas perturbações em torno de uma posição de equilíbrio baseada na missão requerida de forma que as teorias de controle moderno possam ser aplicadas. A técnica de controle empregada é a *Linear Quadratic Tracking* (LQT) formulada como um problema de servomecanismo permitindo que o controlador seja projetado para diferentes sinais de entrada baseados em suas equações diferenciais. O modelo dinâmico e a lei de controle são validadas utilizando o ambiente do Matlab/Simulink® considerando os efeitos não lineares causados pelo mecanismo de *tilt rotor* utilizando como objeto de estudo um modelo quadrirrotor real desenvolvido pelo Laboratório de Aeronaves Autônomas da Universidade Federal de Uberlândia.

Por fim, as condições de estabilidade do sistema são avaliadas para diferentes cenários variando as configurações de *tilt rotor* como também os sinais de entrada a partir do mapeamento de polos e zeros assim como a resposta temporal do sistema. As simulações mostram que a aeronave contendo um mecanismo lateral de *tilt rotor* possui vantagens para aplicações de seguidores de trajetória uma vez que melhora a controlabilidade do sistema principalmente no movimento de guinada. Porém, o mecanismo de *tilt* lateral deve ser utilizado com cautela uma vez que sua atuação amplifica os efeitos não lineares, como por exemplo os giroscópios, que não são previstos pelo modelo linear e podem divergir a resposta do sistema.

## List of symbols

$A$	state matrix
$A_{cl}$	closed loop state matrix
$A_{prop}$	propeller blade section area
$b$	propeller drag coefficient
$BCS$	Body Coordinate System
$B$	input matrix
$C$	output state matrix
$C_D$	propeller section drag coefficient
$CG$	aircraft center of gravity
$C_T$	aerodynamic thrust coefficient
$C_Q$	aerodynamic torque coefficient
$g$	gravity
$ICS$	Inertial Coordinate System
$J_m$	propeller moment of inertia w.r.t. its rotating axis
$J_{xx}, J_{yy}, J_{zz}$	aircraft moments of inertia
$J_{xy}, J_{yz}, J_{zx}$	aircraft products of inertia
$k$	thrust factor
$k_d$	aircraft drag coefficient
$K_\tau$	torque constant
$K_v$	voltage constant
$K_t$	electrical torque constant
$l$	multi-copter arm length
$m_{air}$	air mass
$MCS$	Motor Coordinate System
$n$	number of rotors

$n_t$	number of the tilting mechanisms
$n_s$	number of states
$O_b$	observability matrix
$O_B$	body coordinate frame origin
$O_E$	inertial coordinate frame origin
$O_M$	motor coordinate frame origin
$P, Q, R$	body coordinate frame angular velocities
$P_w$	power consumption
$Q_k$	state weighting matrix
$R_k$	control effort weighting matrix
$R_p$	propeller radius.
$\vec{u}$	input vector
$\vec{u}_{opt}$	optimum input vector
$U$	controllability matrix
$v_{prop}$	propeller blade velocity w.r.t wind
$V_x, V_y, V_z$	velocity components on inertial coordinate system
$\vec{x}$	state vector
$x_B, y_B, z_B$	position in the body coordinate frame
$x_E, y_E, z_E$	position in earth coordinate frame
$x_m, y_m, z_m$	position in motor coordinate frame
$z_{CG_i}$	vertical center of gravity position
$\phi$	roll angle
$\theta$	pitch angle
$\psi$	yaw angle
$\alpha$	longitudinal tilt angle
$\beta$	lateral tilt angle
$\gamma$	rotor position angle w.r.t $x_B$ axis

$\rho$	air density
$\rho_k$	rotor weighting matrix
$\zeta$	damping ratio
$\sigma_k$	tilting mechanism weighting matrix
$\Omega$	propeller angular speed
$\Omega_0$	trimmed propeller angular speed
$\omega_n$	natural frequency

## Summary

1. Introduction.....	1
1.1 Motivations and Objectives .....	1
1.2 Unmanned Aerial Vehicles (UAVs).....	2
1.3 MAVs Classification .....	4
1.4 The Multi-rotors .....	7
1.4.1 Number of rotors.....	7
1.4.2 Actuation Mechanism .....	8
1.5 Control Techniques .....	10
2. System Modeling .....	12
2.1 Reference Frames and Kinematic Relations.....	12
2.2 Equations of Motion .....	16
2.3 External Forces .....	19
2.3.1 Thrust .....	19
2.3.2 Drag.....	22
2.3.3 Gravitational Force .....	23
2.4 External Moments .....	23
2.4.1 Thrust Vector Torque.....	23
2.4.2 Gyroscopic Effect .....	25
2.4.3 Fan Torque .....	26
2.5 Final Dynamical Model .....	27
2.6 Linearization .....	28
3. Modern Control .....	31
3.1 Controllability and Observability .....	32



3.2 Linear Quadratic Regulator .....	33
3.2.1 Quadratic Performance Index .....	33
3.2.2 The Regulator Problem .....	35
3.3 Tracking a Command .....	37
4. Apparatus and Procedures .....	41
4.1 The Multi-rotor .....	41
4.1.1 Quadcopter Structure .....	42
4.1.2 Propulsion System .....	42
4.1.3 Microcontroller .....	43
4.1.4 The Tilting Mechanism .....	44
4.1.5 Inertial Measuring Unit .....	46
4.2 Numerical Simulations .....	46
5. Results and Discussions .....	49
5.1 Checking Controllability and Observability .....	49
5.2 Step Input Position Signal .....	52
5.2.1 Choice of Weighting Matrices .....	52
5.2.2 Pole and Zeros Location Analysis .....	53
5.2.2 Time Response Analysis .....	57
5.3 Ramp Input Signal .....	68
5.3.1 Choice of Weighting Matrices .....	69
5.3.2 Poles and Zeros Analyses .....	69
5.3.3 Time Response Analysis .....	71
5.4 Sinusoidal Input Signal .....	74
5.4.1 Poles and Zeros Analysis .....	74
5.4.2 Time Domain Analysis .....	75
5.5 Random Space Trajectory .....	83
5.6 Conclusions and Highlights .....	88
6. General Conclusions .....	90

6.1 Overview .....	90
6.2 Dynamical Model .....	90
6.3 Control Design.....	91
6.4 The Multi-copter.....	92
6.5 Simulations .....	92
6.6 Future Work.....	93
References ... ..	94
Appendix A .....	98

# Chapter 1

## Introduction

In this introductory chapter, first, the motivations and objectives which gave support to this work are outlined. Later, general information and definitions about unmanned aerial vehicles (UAVs) are presented highlighting their benefits for miniaturization. Further, a brief comparison of different types of aircraft configurations and applied control techniques, including the actuation mechanisms already developed in other works, are presented aiming the UAV control state of art.

### 1.1 Motivations and Objectives

The main aim and motivation of this present work is to investigate the dynamical behavior of a multi-rotor UAV considering a tilt-rotor actuation configuration. Later, a control law based on modern control theory is applied so that the aircraft is able to operate autonomously. Finally, the stability and efficiency of the closed loop system are analyzed aimed at different tilting mechanisms configurations and operational conditions.

On a practical point of view, the development of the project stands on the uprising UAV market share on the global scenario, and also on the upward demand for more efficient and versatile aircrafts for military and civilian applications. Based on current UAV applications, it can be observed that there is constant seek for aircrafts with better endurance, range, stability and capability to perform autonomous flights.

Besides, on a scientific point of view, aircrafts with conventional actuation system (fixed brushless DC motors) are classified as underactuated system and, thus, are not capable to control attitude and position independently (Badr et al, 2016 e Ryll et al, 2012). Hence, the tilt-rotor

configuration is a possibility to solve the problem and also reduce the control energy of the spinning propellers so that the motors do not operate on saturation level (Cutler et al, 2011).

Regarding the control application, some recent works on tilting rotor UAVs proposed linear (Rajappa et al, 2015; Badr et al, 2016; Oosedo et al, 2015) and nonlinear (Ryll et al, 2012; Kendoul et al, 2006) control techniques for autonomous flight applications. However, there are also other control techniques which have shown good performance for fixed rotor multi-copters applications as compared on Bouabdallah (2007) and Suiçmez (2014) works.

Finally, the work yearns to contribute for the development of the recently created *Laboratório de Aeronaves Autônomas* of Federal University of Uberlândia and the Aeronautical Engineering course. The laboratory aims to build its own multi-copter for multi tasks purposes. Most of commercially available platforms does not contemplate a detailed stability analysis based on the system response. Thus, checking the viability of the control law including a tilting-rotor mechanism through the design process can be crucial to increase the aircraft performance.

## **1.2 Unmanned Aerial Vehicles (UAVs)**

In the last few years, unmanned aerial vehicles (UAVs) have made a great impact on aviation. As defined in Nonami et al (2013), an UAV is a powered aerial vehicle that does not carry an onboard crew, can operate with varying degrees of autonomy, and can be expendable and reusable. Usually, the vehicle is controlled remotely via a radio transmitter or an onboard control system. Considering safety and cost, UAVs are a turning point compared to manned air vehicles since it is not dependent of pilot. Thus, they can avoid risking human lives specially for dangerous situations such as, search and rescue, military operations, firefighting, etc; and also favors aircraft miniaturization.

According to Valavanis (2007) the UAVs were first introduced during World War I (1917) by the American army which developed an aerial torpedo capable of guiding itself autonomously to a defined target. Those early systems were considered unreliable and inaccurate and their usefulness were neglected in the battlefields. However, with the development of the gyroscope and new control techniques, the UAVs have begun to attract the attention of military and research community. Hence, several government agencies started to fund research projects to explore this new technology so that unmanned aerial vehicles began to be widely used on military operations as the Vietnam war and lately on Iraq and Afghanistan missions. Bearing in mind that these aircrafts dispensed an onboard crew, they become a valuable tool for surveillance and recognition missions.

Stimulated by the technological progress on electronics and control, the UAV technology became more feasible and, thus, their applications expanded from restrictedly military missions to

a very versatile tool which could be applied on quotidian activities. Among the civilian applications for UAVs, some can be highlighted such as: aerial photography and filming, surveillance, remote sensing, crop analysis, data acquisition, etc. A survey from the *BI Intelligence* enterprise (Business Insider, 2016) has shown that the UAV worldwide market share will grow from 5 billion to 12 billion dollars on military applications while the civilian will be close to 4 billion dollars from 2013 to 2024 as presented on Fig. 1.1. Also, a major part of the investments is concentrated on Europe and the USA.

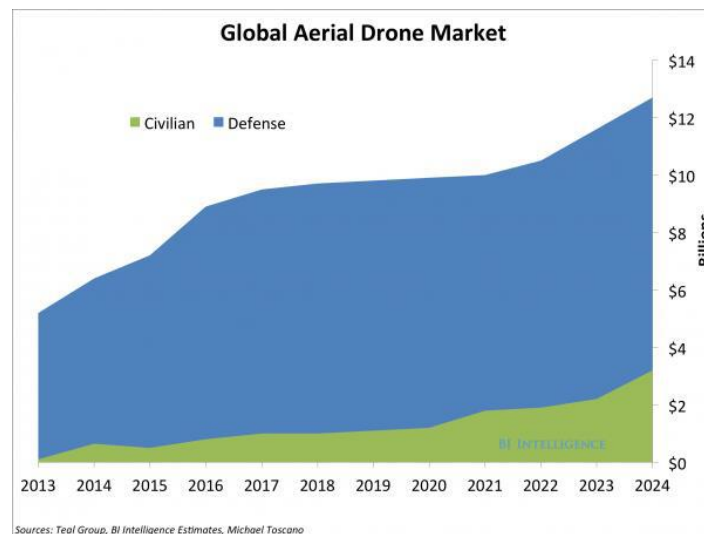


**Figure 1.1 - UAV market share forecast. (Business Insider, 2016)**

Since the applications require more versatile, smaller and lower cost aircrafts, another UAV category has been gaining prominence on the last few years which are the Micro Aerial Vehicles (MAVs). These are a class of miniature UAVs that has a size restriction and may operate autonomously. In general, these miniaturized aircrafts have low endurance, and operates in a short range. On the other hand, their main advantage is the capability to operate on restricted space environment. According to Pines and Bohorquez (2006) a short set of requirements can be set for a typical MAV urban mission in the future as presented on Table 1.1. Even though some requirements presented are still unrealistic, they provide a good guideline for future researches.

**Table 1.1 - Common MAV requirements.**

Specification	Requirements
Size	< 15 cm
Weight	<100 g
Range	1 to 10 km
Endurance	60 min
Altitude	< 150 m
Speed	15 m/s
Payload	20 g
Cost	\$ 1500.00

Notwithstanding, there are some properties which can be optimized on this aircraft category in order to make civilian applications even more feasible. Nowadays, academic researches are being developed in order to come up with MAV designs to fulfill the requirements of: endurance, range, maneuverability, low cost, better energy density (available energy/mass), autonomous flight capability, among others. Furthermore, governmental aviation agencies are working to develop a UAV specific legislation to guarantee the safety of the operations and monitor the applications. Hence, it is essential to assure that the new technologies are able to attend the legal requirements.

Thus, quite a few control techniques for better stability has been investigated to increase aircraft performance under external disturbance, parameters uncertainty, presence of sensor noise. Further, researches on electronics aim to develop compact, lighter and more efficient electrical components.

Other works explore new actuation mechanisms that can be used to control the aircraft optimizing its flight properties. One of these mechanisms is the tilt-rotor configuration where the aircraft motor is attached to the aircraft in such manner that the thrust force vector generated by the propeller can be vectorized. This configuration has been recently investigated and has shown efficient results on multi-rotor MAVs and also on Vertical Take-off and Landing (VTOL) aircrafts and, for this reason, it will serve as motivation for this present work.

### **1.3 MAVs Classification**

In general, aircraft can be divided in two major groups: lighter and heavier than air. This general classification impacts the flying principle, propulsion system characteristics and the aircraft control system. Figure 1.2 presents a general aircraft classification proposed by Bouabdallah (2007) considering the flight principle and propulsion system.

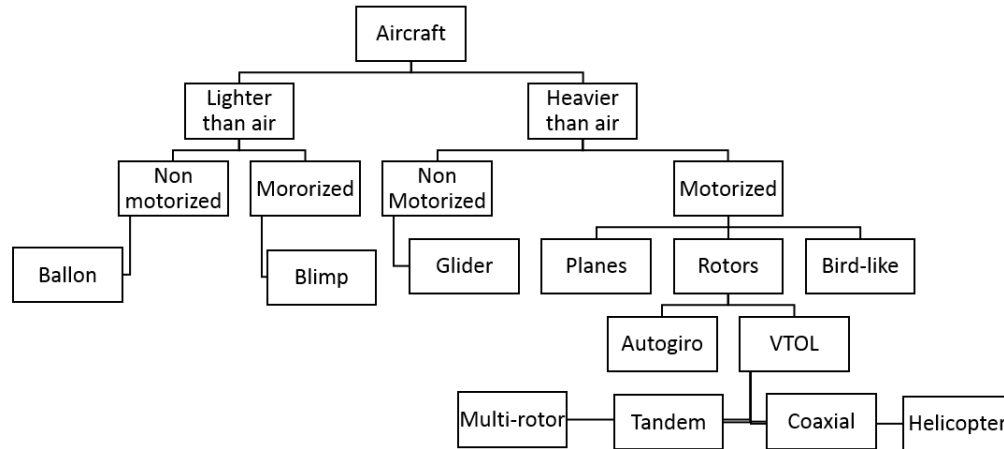


**Figure 1.2 - Aircraft general classification. Adapted from: Bouabdallah (2007).**

Even though each aircraft type has their own advantages and specific applications, just a few of them are feasible for miniaturization accounting the concept design of a MAV. Table 1.2 illustrates different state of art MAV projects highlighting their main advantages and disadvantages.

Further, according to Bouabdallah (2007), it is expected that compact, versatile and cheap MAV aircraft will correspond the major demand for UAV industry principally for quotidian civilian applications. Concerning this, the author proposes and picks out some different MAV configurations and quotes its characteristics on different aspects which should benefit the miniaturization as presented on Table 1.3. The analysis reveals that aircrafts with VTOL characteristics, including helicopters, tandem, coaxial, multi-rotors and blimps, have major advantages over the other configurations. These advantages are summarized on their hover, vertical and low speed flights, allowing them to operate in restricted space environments.

Concerning the helicopters, tandem and coaxial VTOL aircrafts, their speed, position and attitude control mechanism is based on variable pitch rotary wings, which has shown to be very mechanically complex. However, the multi-rotor VTOL configuration, in general, uses fixed pitch spinning propellers. On this case, the forces and moments control are based on the rotor angular speed variation (Suiçmez, 2014). For this reason, the multi-rotors take advantage over the other VTOL configurations due to their mechanical simplicity and also their lesser susceptibility to gyroscopic effects.

Further, the multi-rotor and coaxial VTOL presents better control capability, maneuverability and payload/volume capacity which are essential characteristics for space restricted UAV application.

Table 1.2 - Common MAV configurations. Adapted from: Bouabdallah (2007).









Configuration	Advantages	Disadvantages	Picture
Fixed Wing (Trimble UX5)	Simple mechanics, higher range and endurance	Cannot perform hovering flight	 Trimble (2017)
Helicopter (Scout B1-100)	Controllability, memorability	Complex mechanics, large rotor, tail rotor necessity	 Aeroscout (2017)
Coaxial (Modlab)	Compact geometry	Complex aerodynamics	 Paulos e Yim (2013)
Tandem (Dragonfly DP-6)	Simple aerodynamics, good controllability	Size	 Aeroscout (2017)
Multi-rotor (OS4)	Maneuverability, simple mechanics, higher payload capacity	High energy consumption	 Bouabdallah (2007)
Blimp (VAIRDO Brainbox)	Low energy consumption, higher range and endurance	Size, maneuverability, low operational speed	 Vairdo (2018)
Bird-like (Techject Dragonfly)	Compact geometry, good maneuverability	Complex mechanics / control, high energy consumption	 Techject (2018)
Hybrid VTOL (University of Calgary)	Hover flight, higher endurance and range	Complex mechanics	 Amiri, Ramirez-Serrano and Davies (2011)



Table 1.3 - Flight principle comparison (1=bad, 3=good). Adapted from: Bouabdallah (2007).

	Plane	Helicopter	Bird-Like	Auto-giro	Blimp
<b>Energy cost</b>	2	1	2	2	3
<b>Control cost</b>	2	1	1	2	3
<b>Payload/volume</b>	3	2	2	2	1
<b>Maneuverability</b>	2	3	3	2	1
<b>Hover flight</b>	1	3	2	1	3
<b>Low speed flights</b>	1	3	2	2	3
<b>Vulnerability</b>	2	2	3	2	2
<b>VTOL</b>	1	3	2	1	3
<b>Endurance</b>	2	1	2	1	3
<b>Miniaturization</b>	2	3	3	2	1
<b>Indoor operations</b>	1	3	2	1	2
<b>Total</b>	19	25	24	18	25

## 1.4 The Multi-rotors

Since the multi-rotors has shown to be a valuable candidate for many UAV applications, researchers and the industry developers have already tested many different configurations design based on missions' specifications. Thus, this aircraft category can also be classified concerning the number of rotors and the actuation mechanisms.

### 1.4.1 Number of rotors

The multi-rotors can be classified based on the number of rotors installed on their structure. The most common configurations are: the bi-copters, tri-copters, quad-copters and hexa-copters, as presented on Fig. 1.3. The number of rotors affects the stability and controllability of the system. Further, installing more rotors on the structure increases the generated thrust (payload capacity) but, on the other hand, increases structural weight and energy consumption.

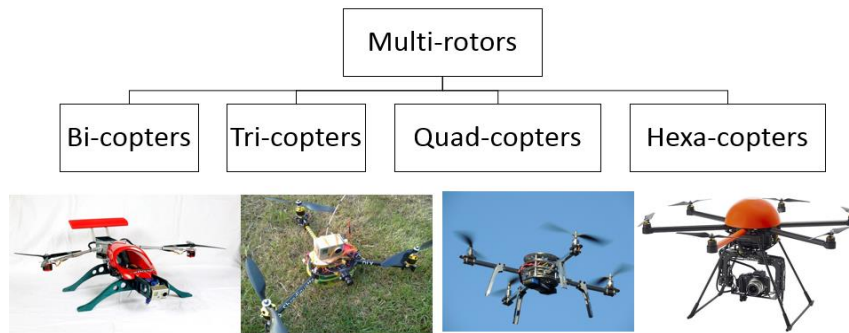


Figure 1.3- Multi-rotors classification by the number of rotors. Sources (from left to right): FPV (2018), Thielicke (2017), Introbotics (2013) and Direct Industry (2018).

### 1.4.2 Actuation Mechanism

In general, in most part of the designed multi-rotor aircrafts, the position and attitude control are based on the rotor capacity to change its rotational speed independently. On this case, the propulsion group is attached to the aircraft structure and their propeller blades have fixed pitch angle. Some research application examples can be found on Bouabdallah (2007), Fogelberg (2013) and Suiçmez (2014) as illustrated on Fig 1.4. Basically, the coordinated rotors angular speed variation generates forces and moments imbalance permitting the aircraft to control attitude and position.



Bouabdallah (2007)



Fogelberg (2013)



Suiçmez (2014)

Figure 1.4 - Fixed pitch and rotor configuration.

However, as discussed in Badr et al. (2016), attitude and position cannot be controlled independently when using this actuation mechanism. Badr et al. (2016) presents this problem as under actuation, i.e. the number of input commands on the system is lower than the number of states to be controlled. Further, on this situation, the aircraft is only capable to perform a hover flight when the roll and pitch angles are zero, meaning that the aircraft is holding a horizontal position w.r.t the inertial coordinate frame.

On this manner, researchers have proposed some strategies in order to optimize multi-rotor control actuation. One of them is the tilt-rotor mechanism which consists on the rotor rotation w.r.t to the multi-rotor arm in a fashion that the thrust vector force produced by the spinning propeller can be vectorized. For instance, Rajappa et al (2015) designed a hexa-copter structure that efficiently explores the input signals since the rotors are can rotate freely around six parallel axes, dismissing the installation of extra actuators. Then, the tilt angles are optimized for each specific mission once the user give a planned trajectory.

Ryll et al (2012) developed a system where all the rotors are capable of rotating about the fixed arm longitudinal axis and their movement are performed by actuators attached to the extremity of multi-copter arm. Similarly, Hintz et al (2014) proposed a quadcopter composed by 8 rotors installed coaxially. Each pair of 4 rotors are connected by a rotating arm in such manner that they can move w.r.t to the central body using only one actuator. This configuration permits 90 degrees hovering flights w.r.t the inertial coordinate frame thus the aircraft is able to cross straight paths.

Finally, Giribet et al (2016) and Badr et al (2016) designed a tilt configuration which the rotors are capable of tilting about an axis normal to the rotors arm. This configuration uses one extra actuator for each multi-copter arm.





Some useful conclusions can be extracted from the research works about the tilt rotors which are:

- energy consumption reduction;
- position and attitude can be controlled independently;
- better maneuverability performance;
- the controller is able to reject external perturbations and keep flight even with a rotor failure.

Another actuation strategy is to affix the propeller blades on an actuator so that their pitch angles can vary, similarly to conventional helicopters. On their work, Cutler et al (2011) observed that, using this configuration, the input control effort can be reduced compared to the conventional fixed pitch propellers. Also, the multi-rotors with this mechanism have better maneuver agility and,

since the system has a faster response compared to the fixed propeller system, the electric rotors are less susceptible to saturation on aggressive maneuvers. Finally, the aircraft is able to perform inverted flights once the propeller pitch angle is inverted. All the presented actuation mechanisms concepts are illustrated on Table 1.4.

**Table 1.4 - Multi-rotor actuator mechanisms.**

<b>Mechanism</b>	<b>Image</b>
Longitudinal tilting mechanism	 <p>Badr et al (2015)</p>
Lateral tilting mechanism	 <p>Ryll et al (2012)</p>
No additional hardware	 <p>Rajappa et al (2015)</p>
Variable pitch propeller mechanism	 <p>Cutler et al (2011)</p>

## 1.5 Control Techniques

Independently of the actuation mechanism or structural design, the multi-copter system is considered as an open-loop unstable system. Hence, it is indispensable to insert a control technique so that it can operate, either autonomously or remotely, on safe conditions. Several control strategies have already been explored and compared either to guarantee the system stability (regulators) or for autonomous flights operations (trackers).

In general, the control strategies can be classified as linear and non-linear. Once that the multi-copter dynamical model is non-linear and coupled, the equations of motion must be

linearized around an operating point (trimming conditions) so that the linear control techniques can be applied. Among the commonly used linear control techniques, the most well-known are the Proportional Integral Derivative (PID), which is a Single Input Single Output (SISO) control technique, and the Linear Quadratic Regulator (LQR) that concerns a multi-state controller. In Bouabdallah (2004), both control techniques are compared while used on the stabilization of a quad-copter attitude test-bench with 3 degrees of freedom. The same techniques are employed for trajectory tracking on Raffo et al (2008), where numerical simulations are validated via experimental results.

For autonomous flights applications, linear control techniques present some limitations once the dynamical model linearization and simplification omits some non-linear dynamical effects which can significantly affect the system behavior (Kendou et al, 2007). Furthermore, there are uncertainty parameter problems, actuators saturation, noise and external disturbances that affects the plant and can bring the system to instability condition.

Additionally, since the non-linear control techniques are based on the stability condition of the non-linear model, they can present better robustness compared to the linear. The most common are: the Backstepping,  $H_\infty$ , Feedback Linearization and Sliding Mode Control. On his work, Rich (2012) proposed a  $H_\infty$  controller to stabilize the rotation movements and a Backstepping controller to control minimizes the difference between the aircraft current and desired positions, so that it can track a pre-defined trajectory.

Even though some control techniques being able to accomplish a specific task, it is also possible to distinguish them on some features as: energy consumption, steady state error, response time, actuator saturation and disturbance rejection. For instance, on his work, Suiçmez (2014) compared linear and non-linear control techniques such as LQR, LQT and Backstepping with the purpose of evaluate their operational parameters so that the multi-copter could operate autonomously with better efficiency.

In summary, each control techniques have its own advantages and drawbacks. For instance, on his work, Suiçmez (2014) has shown that the LQT controller may present less energy consumption and better disturbance rejection over the LQR and Backstepping controller. Further, on Bouabdallah (2007) PID, LQ, Sliding Mode and Backstepping controllers were compared and, it can be inferred that a combination of PID and Backstepping (also known as Integral Backsetpping) is the best control approach for multi-copter autonomous flight.

the LQR/LQT control was chosen for this work since it is based on multi-state models, has shown good robustness and it can be easily implemented on a real microcontroller.

## Chapter 2

### System Modeling

The concept of this section is to derive the dynamical model of a generic multi-copter with  $n$  rotors such that each rotor is capable of tilting in two different directions: laterally and longitudinally with respect to the rotor's arm, introducing more control inputs to the system. First, the reference frames used to develop the equations along with their kinematic relations will be presented in section 2.1. Then, the equations of motion of a general aircraft (fixed wing or multi-copter) will be developed in Section 2.1. On sequence, the external forces and moments acting on the multi-rotor body will be explained in section 2.3. Lastly, Section 2.4 contains the full non-linear dynamical model of the aircraft, and the equations are linearized around the trimming operating conditions based on mission applications in order to allow the linear control techniques to be applied.

Some considerations must be taken before the model development which are:

- The aircraft structure is supposed rigid.
- The propellers are rigid.
- Earth's gravitational field ( $g$ ), mass of the quadrotor and body inertia matrix of the quadrotor ( $J$ ) are constants.
- Thrust factor ( $k$ ), torque factor ( $b$ ) and the drag coefficient ( $k_d$ ) are constants.
- Inertia of the rotors are neglected.

### 2.1 Reference Frames and Kinematic Relations

Before deriving the dynamical model of the multi-copter, the reference frames must be identified. In this work, three different reference frames will be used in order to model the aircraft dynamics coupled with the rotor tilting. They are: an Earth fixed reference frame designated as

Inertial Coordinate System (*ICS*), body fixed coordinate frame (*BCS*) and a motor fixed coordinate frame (*MCS*).

Figure 2.1 illustrates the three reference frames adopted. The Earth fixed reference frame can be considered as an inertial reference system since the rotation of the Earth relative to distant stars are negligible. Thus, the absolute position of the multi-copter is expressed with respect to the origin point  $O_E$  using the *ICS* coordinates  $ICS: \{O_E; x_E, y_E, z_E\}$ . The aircraft velocity with respect to an inertial observer written on the fixed reference frame is expressed by  $\vec{V}_E = [V_x \ V_y \ V_z]^T = [\dot{x}_E \ \dot{y}_E \ \dot{z}_E]^T$ , being  $V_x$ ,  $V_y$  and  $V_z$  the velocity components along  $x_E$ ,  $y_E$  and  $z_E$  axes.

Further, the body fixed reference frame  $BCS: \{O_B; x_B, y_B, z_B\}$  is attached to the aircraft translating and rotating with the body. The origin of *BCS* coincides with the aircraft center of gravity (*CG*), and its translational velocity and angular velocity vectors are denoted by  $\vec{v} = [u \ v \ w]^T$  and  $\vec{\omega} = [P \ Q \ R]^T$ , respectively, such that  $P$ ,  $Q$  and  $R$  are the angular velocities around the  $x_B$ ,  $y_B$  and  $z_B$  axis. Remarking that theses velocities are written w.r.t. a fixed observer at the *ICS*.

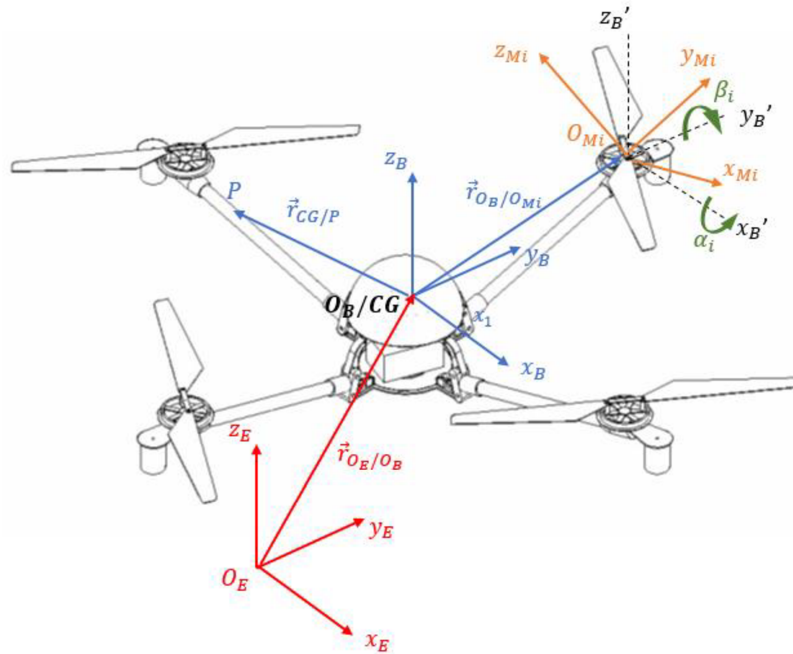


Figure 2.1 - Coordinate (ICS, BCS and MCS) frames representation.

The aircraft attitude can be defined with respect to the body fixed frame (BSC) using the Euler angles, which are represented by  $\Theta = [\phi \ \theta \ \psi]^T$  corresponding to the roll, pitch and yaw angles, respectively, as presented on Fig. 2.2. The Euler angles angular velocities are expressed as the time rate change of the Euler angles  $\dot{\Theta} = [\dot{\phi} \ \dot{\theta} \ \dot{\psi}]^T$ . It must be remarked that  $\omega \neq \dot{\Theta}$  since the  $\omega$  vector points in the rotation axis, while  $\dot{\Theta}$  only represents the time derivative of the attitude angles. However, these two vectors are correlated by a kinematic relation (Roskam, 2001):

$$\omega = \begin{bmatrix} 1 & 0 & -\sin \theta \\ 0 & \cos \phi & \cos \phi \cos \theta \\ 0 & -\sin \phi & \cos \theta \cos \phi \end{bmatrix} \dot{\Theta} \quad (2.1.1)$$

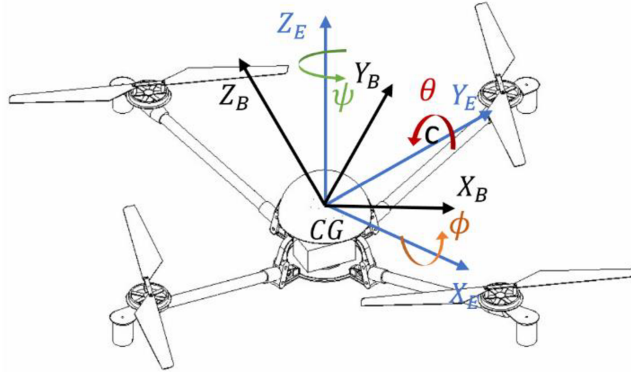


Figure 2.2 - Euler angles representation.

A vector represented on the *BCS* frame is interrelated with the *ICS* coordinate frame by the Euler angles. Using orthogonal transformation, it is possible to create a rotational matrix which relates the two coordinate frames. This matrix considers a sequence of rotations on the following order: yaw ( $R_B^I(\psi)$ ), pitch ( $R_B^I(\theta)$ ) and roll ( $R_B^I(\phi)$ ):

$$R_B^I(\psi) = \begin{bmatrix} \cos \psi & -\sin \psi & 0 \\ \sin \psi & \cos \psi & 0 \\ 0 & 0 & 1 \end{bmatrix} \quad (2.1.2)$$



$$R_B^I(\theta) = \begin{bmatrix} \cos\theta & 0 & \sin\theta \\ 0 & 1 & 0 \\ -\sin\theta & 0 & \cos\theta \end{bmatrix} \quad (2.1.3)$$

$$R_B^I(\phi) = \begin{bmatrix} 1 & 0 & 0 \\ 0 & \cos\phi & -\sin\phi \\ 0 & \sin\phi & \cos\phi \end{bmatrix} \quad (2.1.4)$$

The rotation matrix  $R_B^I$  is obtained by multiplying Eqs. (2.1.2), (2.1.3) and (2.1.4), extricly on this order as presented previously. Hence, any vector in the *BCS* coordinate frame can be written in the *ICS* by the relation:

$$\vec{q}_I = R_B^I \cdot \vec{q}_B \quad (2.1.5)$$

where  $\vec{q}_I$  and  $\vec{q}_B$  are vectors in the *ICS* and *BCS*, respectively.

Since the  $R_B^I$  is orthogonal, its inverse is equivalent to its transpose; thus, the transformation from the *ICS* to the *BCS* is given by (Marques, 2016):

$$\vec{q}_B = R_B^I \cdot \vec{q}_I = (R_B^I)^{-1} \cdot \vec{q}_I = (R_B^I)^T \cdot \vec{q}_I \quad (2.1.6)$$

The motor reference axis  $MCS : \{O_{Mi}; x_{m_i}, y_{m_i}, z_{m_i}\}$ ,  $i = 1 \dots n$  is the frame attached to the  $i$ -th propulsive group, with  $x_{m_i}$  representing the laterally tilting actuation axis,  $y_{m_i}$  the longitudinally tilting actuation axis and  $z_{m_i}$  the propeller spinning axis that is coincident with the thrust force direction (Ryll et al, 2012). The vectoring rotors are located at the extremities of the UAV's arms at  $P$  by an angle  $\gamma_i = \frac{\pi}{n}(2i-1)$ ,  $i = 1 \dots n$  w.r.t the  $x_B$  axis direction of the *BCS*. Also, the *MCS* translates with the aircraft and the orientation of the  $i$ -th propeller group can be represented on the *BCS* using the following rotation matrices:

$$R_M^B(\gamma_i) = \begin{bmatrix} \cos\gamma_i & -\sin\gamma_i & 0 \\ \sin\gamma_i & \cos\gamma_i & 0 \\ 0 & 0 & 1 \end{bmatrix} \quad (2.1.7)$$

$$R_M^B(\alpha_i) = \begin{bmatrix} \cos\alpha_i & 0 & \sin\alpha_i \\ 0 & 1 & 0 \\ -\sin\alpha_i & 0 & \cos\alpha_i \end{bmatrix} \quad (2.1.8)$$

$$R_M^B(\beta_i) = \begin{bmatrix} 1 & 0 & 0 \\ 0 & \cos\beta_i & -\sin\beta_i \\ 0 & \sin\beta_i & \cos\beta_i \end{bmatrix} \quad (2.1.9)$$

where  $\alpha_i$  and  $\beta_i$  represent the longitudinal and the lateral tilting angles about axis  $x_{m_i}$  and  $y_{m_i}$ , respectively

As illustrated on Fig. 2.1, the  $\{x_b', y_b', z_b'\}$  coordinate frame represents the *BCS* rotated by  $\gamma_i$  so that  $y_b'$  is pointed on the multi-copter arm direction. This coordinate system is related with *BCS* by Eq. (2.1.7). Thus, the tilting angles  $\alpha_i$  and  $\beta_i$  represents a longitudinal and lateral rotation of the *MCS* w.r.t.  $x_b'$  and  $y_b'$  direction axis, respectively.

Consequently, a vector on the *MCS* can be written on the *BCS* using the relation presented on Eq. (2.1.6), where the rotational matrix  $R_M^B$  is the multiplication of (2.1.9), (2.1.8) and (2.1.7) matrices, respectively, as follows:

$$\vec{q}_B = R_M^B(\gamma).R_M^B(\alpha_i).R_M^B(\beta_i).\vec{q}_M \quad (2.1.10)$$

## 2.2 Equations of Motion

According to Valavanis (2007), for any aircraft configuration (either rotary or fixed wing), the equations of motion can be derived using Newton-Euler formulation applied to a rigid body having six degrees of freedom (three translations and three rotations). Further, in this circumstance, Newton's second law is described on the body coordinate frame, so the vectors on *MCS* and *ICS* coordinate systems can be written on *BCS* using the orientation matrices  $R_M^B$  and  $R_I^B$ . Moreover, one is motivated to describe the derivative terms with respect to an observer at the *BCS* to distinguish the effects of magnitude and orientation variation. The external forces acting on the

body  $CG$  are denoted by the vector  $\vec{F} = [F_x \ F_y \ F_z]^T$  while the external moments by  $\vec{M} = [M_x \ M_y \ M_z]^T$ . The angular velocities and moment components are considered counter-clockwise positive w.r.t their rotation axes.

As illustrated on Fig. 2.1, the position of the aircraft  $CG$  on the  $ICS$  is represented by the vector  $\vec{r}_{O_E/cg}$  while the position of any rigid point  $O_B$  with an infinitesimal mass  $dm$  w.r.t the  $BCS$  is represented by  $\vec{r}_{cg/p}$ . Thus, the position of point  $P$  on the  $ICS$  ( $\vec{r}$ ) will be:

$$\vec{r} = \vec{r}_{o/cg} + \vec{r}_{cg/p} \quad (2.2.1)$$

Moreover, the velocity of point  $P$  is obtained taking the time derivative of Eq. (2.2.1):

$$\vec{v}_p = \frac{d\vec{r}}{dt} \Big|_{ICS} = \frac{d\vec{r}_{o/cg}}{dt} \Big|_{ICS} + \frac{d\vec{r}_{cg/p}}{dt} \Big|_{ICS} \quad (2.2.2)$$

where the subscript (i.e.: the  $ICS$ ) indicates which observer the time derivative is taken in account.

On Eq. (2.2.2),  $\frac{d\vec{r}_{o/cg}}{dt} \Big|_{ICS}$  denotes the velocity of the aircraft  $CG$  while the time derivative of  $\vec{r}_{cg/p}$  is given by:

$$\frac{d\vec{r}_{cg/p}}{dt} \Big|_{ICS} = \frac{d\vec{r}_{cg/p}}{dt} \Big|_{BCS} + \vec{\omega} \times \vec{r}_{cg/p} \quad (2.2.3)$$

where,  $\vec{\omega}$  is the angular velocity vector as defined previously and  $\frac{d\vec{r}_{cg/p}}{dt} \Big|_{BCS}$  is the time derivative of vector  $P$  w.r.t the  $BCS$ . Since the body is considered rigid, it can be inferred that  $\frac{d\vec{r}_{cg/p}}{dt} \Big|_{BCS} = 0$ . Then, any point attached to the aircraft has the velocity described as:

$$\vec{v}_p = \frac{d\vec{r}_{o/cg}}{dt} \Big|_{ICS} + \vec{\omega} \times \vec{r}_{cg/p} \quad (2.2.4)$$

Analogously to Eq. (2.2.2), the acceleration of any arbitrary point can be obtained taking the time derivative of Eq. (2.2.4) w.r.t the  $ICS$ :

$$\vec{a}_p = \frac{d\vec{v}_p}{dt} \Big|_{ICS} = \frac{d\vec{v}_p}{dt} \Big|_{BCS} + \vec{\omega} \times \vec{v}_p \quad (2.2.5)$$

The term  $\left. \frac{d\vec{v}_p}{dt} \right|_{BCS}$  in the above equation represents the time derivative of the aircraft velocity ( $\vec{v}$ ) w.r.t  $BCS$ . Thus, the acceleration vector can be written as:

$$\vec{a} = \begin{bmatrix} \vec{a}_x \\ \vec{a}_y \\ \vec{a}_z \end{bmatrix} = \begin{bmatrix} \dot{u} - Rv + Qw \\ \dot{v} - Pw + Ru \\ \dot{w} - Qu + Pv \end{bmatrix} \quad (2.2.6)$$

Applying Newton's Second Law:

$$\sum F = m\vec{a} \rightarrow \begin{bmatrix} \sum F_x \\ \sum F_y \\ \sum F_z \end{bmatrix} = m \begin{bmatrix} \dot{u} - Rv + Qw \\ \dot{v} - Pw + Ru \\ \dot{w} - Qu + Pv \end{bmatrix} \quad (2.2.7)$$

Now, regarding the dynamical equations of the angular motion, it is known that the resultant angular momentum acting on the center of the gravity w.r.t  $BCS$ , given the assumptions described previously, can be written as:

$$\vec{H} = J\omega \rightarrow \begin{bmatrix} h_x \\ h_y \\ h_z \end{bmatrix} = J \begin{bmatrix} P \\ Q \\ R \end{bmatrix} \quad (2.2.8)$$

where  $J$  is the aircraft inertia tensor written on the  $BCS$  represented by:

$$J = \begin{bmatrix} J_{xx} & -J_{xy} & -J_{xz} \\ -J_{yx} & J_{yy} & -J_{yz} \\ -J_{zx} & -J_{zy} & J_{zz} \end{bmatrix} \quad (2.2.9)$$

In general, most of the multi-rotor UAV configurations have two symmetry planes, thus it can be inferred about the products of inertia that  $J_{yx} = J_{xy} = 0$ ,  $J_{yz} = J_{zy} = 0$  and  $J_{zx} = J_{xz} = 0$ . Furthermore, the moments of inertia ( $J_{xx}$ ,  $J_{yy}$  and  $J_{zz}$ ) are considered constant since it is assumed that there is no mass variation along the aircraft flight and that the tilting angles variations are small so that their effect over the inertia properties are negligible.

Furthermore, taking the time derivative of Eq. (2.2.8) w.r.t  $ICS$ :

$$\left. \frac{d\vec{H}}{dt} \right|_{ICS} = \left. \frac{d\vec{H}}{dt} \right|_{BCS} + \vec{\omega} \times \vec{H} \quad (2.2.10)$$

while the angular momentum time derivative w.r.t  $BCS$  is:

$$\left. \frac{d\vec{H}}{dt} \right|_{BCS} = J \begin{bmatrix} \dot{P} \\ \dot{Q} \\ \dot{R} \end{bmatrix} = \begin{bmatrix} \dot{h}_x \\ \dot{h}_y \\ \dot{h}_z \end{bmatrix} = \begin{bmatrix} J_{xx}\dot{P} \\ J_{yy}\dot{Q} \\ J_{zz}\dot{R} \end{bmatrix} \quad (2.2.11)$$

Hence, from Newton-Euler Second Law, the external moments applied to the aircraft *CG* written on the *BCS* is associated to the angular velocities time derivatives by the following expression:

$$\sum M = \frac{d\vec{H}}{dt} \rightarrow \begin{bmatrix} \sum M_x \\ \sum M_y \\ \sum M_z \end{bmatrix} = \begin{bmatrix} J_{xx}\dot{P} + QR(J_{zz} - J_{yy}) \\ J_{yy}\dot{Q} + PR(J_{xx} - J_{zz}) \\ J_{zz}\dot{R} + PQ(J_{yy} - J_{xx}) \end{bmatrix} \quad (2.2.12)$$

## 2.3 External Forces

The motion of an aircraft on space is caused by a series of controlled forces and moments which are necessary to counteract those which are perturbing the system. Generally, multi-rotor UAVs are equipped with a motor-propulsive system, which is the source of thrust required to overcome or equilibrate aircraft's weight and drag. Also, in this work will be considered an actuation system which enable the motor-propulsive system to tilt longitudinally and laterally w.r.t the multi-rotor arm. Further, it's assumed that each rotor is independently actuated.

In this section, the external forces associated with the environment physical effects are presented. They are: the thrust force from the motor-propulsive system considering the tilting mechanism in two different directions, the aircraft weight and the aerodynamic drag.

### 2.3.1 Thrust

Micro autonomous flying vehicles typically utilize a motor-propulsive set, consisted by spinning rotors equipped with propellers, for actuation. In particular, brushless motors have become the standard for multi-rotor vehicles with a weight greater than about 100 grams, while brushed motors are still used for the smallest vehicles (Conroy, Humbert and Nothwang, 2014).

A typical UAV electric propulsion system is shown on Fig. 2.3. Each rotor of the multi-rotor has a separate powertrain. Designating  $\mu$  as the requested input signal,  $\Omega$  as the output rotational velocity of the motor and  $T$  as the thrust force produced by the propeller.

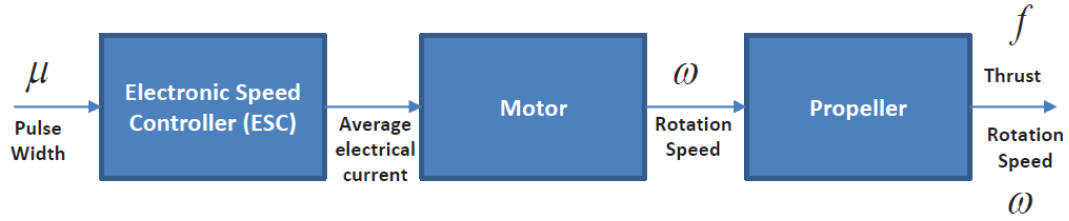


Figure 2.3 -Typical Brushless Motor Powertrain (Conroy, Humbert and Nothwang, 2014).

The system mechanism can be described as follows: the electronic speed control (ESC) accepts an input signal and is responsible for controlling the commutation of the motor; the ESC input signal is typically supplied by a vehicle autopilot, most often in the form of a pulse-width modulated (PWM) or I<sup>2</sup>C signal. The input value determines the average current the ESC should provide to the motor. The motor uses the electrical power to spin the propeller at a desired speed. The propeller, since it has an aerodynamic shape, generates lift, consequently, producing a thrust vector normal to the propeller radius.

It is known that the motor power consumption ( $P_w$ ) during a given interval, ideally, can be transferred to mechanical power produced by the spinning propeller generating thrust ( $T$ ). From energy conservation:

$$P_w \cdot dt = F dx \quad \rightarrow \quad P_w = F \frac{dx}{dt} \quad \rightarrow \quad P_w = T v_h \quad (2.3.1)$$

being  $dx$  the travel distance of an air particle w.r.t the disc and  $v_h$  the air induced velocity when the aircraft is hovering.

Assuming a steady and calm environment, where  $v_\infty = 0$ , the air mass ( $m_{air}$ ) flow crossing the propeller disc is given by:

$$\dot{m}_{air} = \rho \pi R_p^2 v_h \quad (2.3.2)$$

where  $\rho$  is the air density and  $R_p$  the propeller radius.

From Rankine-Froude theory (Asselin, 1965), the thrust force produced by the propeller is:

$$T = m_{air} \frac{dV}{dt} = \dot{m}_{air} \Delta V = 2 \rho \pi R_p^2 v_h^2 \quad (2.3.3)$$

Hence, isolating the hovering velocity on Eq. (2.3.3) and substituting it on Eq. (2.3.1), the power produced by the motor in watts ( $W$ ) is:

$$P_w = \frac{T^{\frac{3}{2}}}{\sqrt{2\rho\pi R_p^2}} \quad (2.3.4)$$

Regarding the aerodynamic behavior of the propeller blade, from the momentum blade theory (Magnusson, 2014), it is possible to write the thrust force and torque generated by the spinning propeller which are presented, respectively, as:

$$T = C_T \rho R_p^4 \pi \Omega^2 \quad (2.3.5)$$

$$\tau = C_Q \rho R_p^5 \pi \Omega^2 \quad (2.3.6)$$

where  $C_T$  and  $C_Q$  are aerodynamic constants for thrust and torque, respectively, which depends on the blade section.

Moreover, considering that the produced torque is proportional to the thrust force by a constant  $K_\tau$  :

$$K_\tau = \frac{C_Q R_p}{C_T} \quad (2.3.7)$$

Now, bearing in mind the electrical behavior of the motor, the torque ( $\tau$ ) produced by a brushless motor is proportional, by a constant ( $K_t$ ), to the motor's input current ( $i$ ). However, it must be accounted a residual current ( $i_0$ ) corresponding to the current when there is no load in the motor. Thus,

$$\tau = K_t (i - i_0) \quad (2.3.8)$$

Further, the voltage ( $V$ ) applied to the motor considering the resistive loss, is given by:

$$V = iR_m + K_v \Omega \quad (2.3.9)$$

$R_m$  and  $K_v$  being the motor electrical resistance and a proportional constant between the applied voltage and the motor's shaft angular speed.

Hence, the motor's electrical power is obtained from Eqs. (2.3.8) and (2.3.9):

$$P_w = iV = \frac{(\tau + K_t i_0)(K_t i_0 R_m + \tau R_m + K_t K_v \Omega)}{K_t^2} \quad (2.3.10)$$

In order to simplify the model, the following assumptions can be made without great losses:  
(i) the motor electrical resistance is negligible ( $R_m \rightarrow 0$ ); (ii)  $\tau \gg K_t i_0$  since  $i_0$  is the current when

there is no load and is, consequently, small. Finally, the motor electrical power can be stated as follows:

$$P_w \sim \frac{K_v}{K_t} \tau \Omega \quad (2.3.11)$$

Thus, assuming that all the driver shaft is transferred to the propeller, Eq. (2.3.10) can substitute on Eq. (2.3.4) and isolating the thrust ( $T$ ) gives:

$$T = \left( \frac{K_\tau K_v \sqrt{2\rho\pi R_m^2}}{K_t} \Omega \right)^2 = k\Omega^2 \quad (2.3.12)$$

In conclusion, the thrust force produced by each rotor is proportional to the square of the angular speed of the rotor propeller by a constant  $k$ . So, the thrust vector generated by the  $n$  motor-propulsive group, written on the  $MCS$ , is:

$$T_{MCS} = \sum_{i=1}^n T_i = \begin{bmatrix} 0 \\ 0 \\ \sum k\Omega_i^2 \end{bmatrix} \quad (2.3.13)$$

The thrust vector can be oriented on the  $BCS$  applying the rotational matrix transformation from Eq. (2.1.10) on Eq. (2.3.13). Hence,

$$T_{BCS} = \begin{bmatrix} \sum_{i=1}^n (\sin(\gamma_i) \sin(\beta_i) + \cos(\gamma_i) \sin(\alpha_i) \cos(\beta_i)) k\Omega_i^2 \\ \sum_{i=1}^n (-\cos(\gamma_i) \sin(\beta_i) + \sin(\gamma_i) \sin(\alpha_i) \cos(\beta_i)) k\Omega_i^2 \\ \sum_{i=1}^n \cos(\alpha_i) \cos(\beta_i) k\Omega_i^2 \end{bmatrix} \quad (2.3.14)$$

### 2.3.2 Drag

In this model, the drag due to the incoming viscous flow will be considered. For small multi-rotor applications, the viscous drag can be considered as proportional, by a constant  $k_d$ , to the linear velocity w.r.t the  $BCS$  on the three directions (Fogelberg, 2013). Hence, the drag force vector, acting on the  $CG$ , is represented by:



$$F_D^{BCS} = -k_d \vec{v} = \begin{bmatrix} -k_{dx}u \\ -k_{dy}v \\ -k_{dz}w \end{bmatrix} \quad (2.3.15)$$

### 2.3.3 Gravitational Force

Since the aircraft operates in Earth magnetic field, the gravitational force will be always acting on the body's *CG* on negative  $z$  direction of the *ICS*. Additionally, once the multi-rotor operates at low altitudes, this force can be assumed constant. Therefore, the gravitational force vector on the *ICS* is:

$$F_{grav}^{ICS} = \begin{bmatrix} 0 \\ 0 \\ -mg \end{bmatrix} \quad (2.3.16)$$

Applying the rotational matrix transformation from the *ICS* to the *BCS* (Eq. (2.1.6)), the gravitational force vector can be oriented on the *BCS*, resulting in:

$$F_{grav}^{BCS} = (R_B^I)^T \cdot F_{grav}^{ICS} = \begin{bmatrix} mg \sin \theta \\ -mg \sin \phi \cos \theta \\ -mg \cos \phi \cos \theta \end{bmatrix} \quad (2.3.17)$$

## 2.4 External Moments

After describing the external forces acting on the multi-rotor UAV, the moments produced by these forces are presented in this section. Since the gravitational and drag forces act on the body center of gravity, they do not produce torque on the aircraft. However, the thrust force from the motor-propulsive system generates a torque associated with the multi-rotor position w.r.t the aircraft *CG* (moment arm). Henceforth, the torques are detailed subsequently. They are: the torque due the thrust force variation (inertial), gyroscopic effect torque and torque due to propeller drag.

### 2.4.1 Thrust Vector Torque

As presented previously, the propeller produces a thrust force vector on the  $z_m$  direction of the *MCS*. Thus, each motor-propeller group produces a torque, at the UAV center *CG*, which can be defined as the cross product of the force vector and the moment arm. In this case, the moment arm represents the spatial position of the motor on the *BCS*. From Fig. 2.4, the moment arm vector  $\vec{d}$  can be written as:

$$\vec{d}_i = \begin{bmatrix} l \cos \gamma_i & l \sin \gamma_i & z_{CG_i} \end{bmatrix}^T \quad (2.4.1)$$

where  $l$  is the multi-rotor arm length and  $z_{CG_i}$  the vertical distance of the rotor from the  $CG$ .

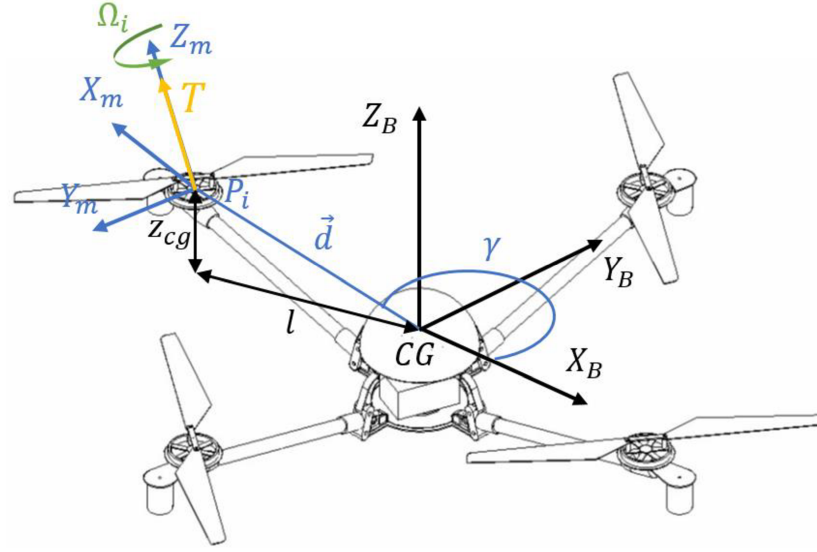


Figure 2.4 - Position of the  $i$ -th rotor w.r.t the  $CG$ .

Now, the resultant torque due to thrust force is determined taking the cross-product of the moment arm (Eq.(2.4.1)) and the thrust vector force on the  $BCS$  (Eq. (2.3.14)). Considering  $\sin(x) = s(x)$  and  $\cos(x) = c(x)$ :

$$\vec{\tau}_T = \vec{d}_i \times \vec{T}_{BCS} \quad (2.4.2)$$

$$\vec{\tau}_T = \begin{bmatrix} \sum_{i=1}^n \left( l s(\gamma_i) c(\alpha_i) c(\beta_i) - z_{CG} (s(\gamma_i) s(\alpha_i) c(\beta_i) - c(\gamma_i) s(\beta_i)) \right) k \Omega_i^2 \\ \sum_{i=1}^n \left( -l c(\gamma_i) c(\alpha_i) c(\beta_i) + z_{CG} (c(\gamma_i) s(\alpha_i) c(\beta_i) + s(\gamma_i) s(\beta_i)) \right) k \Omega_i^2 \\ \sum_{i=1}^n \left( l c(\gamma_i) (s(\gamma_i) s(\alpha_i) c(\beta_i) - c(\gamma_i) s(\beta_i)) - l s(\gamma_i) (c(\gamma_i) s(\alpha_i) c(\beta_i) + s(\gamma_i) s(\beta_i)) \right) k \Omega_i^2 \end{bmatrix} \quad (2.4.3)$$

The torque vector  $\vec{\tau}_T$  has three components along  $x_B$ ,  $y_B$  and  $z_B$  axes which are known as roll, pitch and yaw torque, respectively. Note that, for fixed rotor multi-rotors, the yaw torque is zero, and roll and pitch torques depend on the position and the propeller angular speed of each rotor. Thus, the combination of angular speed variation allows the aircraft to change attitude and, consequently, shift on  $x_E$  and  $y_E$ .

### 2.4.2 Gyroscopic Effect

In some works (Oosedo et al, 2015; Rajappa et al, 2015; Ryll, Bulthoff and Giordano, 2012) the resultant gyroscopic torque is neglected since it is considered that the aircraft angular speed and thrust force vector direction variations are small. Besides, on other works, such as Bouabdallah, 2007, the gyroscopic effect is accounted on the dynamical model. However, as presented in Roskam (2001), the gyroscopic effect plays a major role on vectorizing thrust propulsion system, such as the tilting rotors considered on this work. Hence, the phenomenon will be accounted with the purpose of increasing the model fidelity.

Since the aircraft angular speed varies while the aircraft's propellers are spinning, the gyroscopic effect will be present on the model as a consequence of propeller's angular momentum variation during flight. As a result, a gyroscopic torque is produced acting on the aircraft center of gravity of the aircraft.

Thus, the angular momentum produced by the  $n$  propellers, w.r.t their own rotation axis  $z_{m_i}$ , is given by:

$$\vec{H} = \begin{bmatrix} 0 \\ 0 \\ \sum_{i=1}^n J_{Mi} \vec{\Omega}_i \end{bmatrix} \quad (2.4.4)$$

where  $J_{Mi}$  is the  $i$ -th propeller's moment of inertia w.r.t its rotating axis.

Further, the angular momentum on the  $BCS$  is obtained applying the rotational transformation (2.1.10) on Eq. (2.4.4). Hence,

$$\vec{H}_{BCS} = \begin{bmatrix} \sum_{i=1}^n (\sin(\gamma_i) \sin(\beta_i) + \cos(\gamma_i) \sin(\alpha_i) \cos(\beta_i)) J_{mi} \Omega_i \\ \sum_{i=1}^n (-\cos(\gamma_i) \sin(\beta_i) + \sin(\gamma_i) \sin(\alpha_i) \cos(\beta_i)) J_{mi} \Omega_i \\ \sum_{i=1}^n \cos(\alpha_i) \cos(\beta_i) J_{mi} \Omega_i \end{bmatrix} \quad (2.4.5)$$

The gyroscopic torque is obtained taking the time derivative of Eq. (2.4.4) analogously to Eq. (2.2.2):

$$\tau_G = \left( \dot{\vec{H}} \right)_{ICS} = \left( \frac{d\vec{H}}{dt} \right)_{BCS} + \omega_B \times \vec{H} \quad (2.4.6)$$

being  $\omega_B$  the angular velocity felt by each rotor considering the tilting mechanism. The rotor angular velocity on the *MCS* is given by:

$$\omega_m = \begin{bmatrix} \dot{\beta}_i & \dot{\alpha}_i & 0 \end{bmatrix}^T \quad (2.4.7)$$

Applying the rotational transformation, Eq.(2.1.10), and adding the body angular velocity on the body coordinate frame ( $\omega$ ) :

$$\omega_B = \begin{bmatrix} \cos(\alpha_i) \dot{\beta}_i + P & \dot{\alpha}_i + Q & -\sin(\alpha_i) + R \end{bmatrix}^T \quad (2.4.8)$$

Considering that the propeller angular speed variation is negligible and the propeller moment of inertia is constant, then  $\left( \frac{d\vec{H}}{dt} \right)_{BCS}$ . Henceforth, the gyroscopic torque is obtained substituting Eqs. (2.4.5) and (2.4.5) on Eq, (2.4.6):

$$\vec{\tau}_G = \begin{bmatrix} \sum_{i=1}^n \left( (\dot{\alpha}_i + Q) \cos(\alpha_i) \cos(\beta_i) - (R - \sin(\alpha_i)) (-\cos(\gamma_i) \sin(\beta_i) + \sin(\gamma_i) \sin(\alpha_i) \cos(\beta_i)) \right) J_{mi} \Omega_i \\ \sum_{i=1}^n \left( -(\cos(\alpha_i) \dot{\beta}_i + P) \cos(\alpha_i) \cos(\beta_i) + (-\sin(\alpha_i) + R) (\sin(\gamma_i) \sin(\beta_i) + \cos(\gamma_i) \sin(\alpha_i) \cos(\beta_i)) \right) J_{mi} \Omega_i \\ \sum_{i=1}^n \left( \cos(\alpha_i) \dot{\beta}_i + P \right) (-\cos(\gamma_i) \sin(\beta_i) + \sin(\gamma_i) \sin(\alpha_i) \cos(\beta_i)) - (\dot{\alpha}_i + Q) (\sin(\gamma_i) \sin(\beta_i) + \cos(\gamma_i) \sin(\alpha_i) \cos(\beta_i)) J_{mi} \Omega_i \end{bmatrix} \quad (2.4.9)$$

### 2.4.3 Fan Torque

The fan torque is a consequence of the aerodynamic drag force produced by the propeller when it is rotating around its spinning axis. According to Asselin (1965), the drag force ( $F_D$ ) acting on the spinning propeller is given by:

$$F_D = \frac{1}{2} \rho C_D A_{prop} v_{prop}^2 \quad (2.4.10)$$

where  $A_{prop}$  is the propeller blade section area,  $\rho$  is the air density,  $C_D$  the drag coefficient and  $v_{prop}$  the propeller blade velocity w.r.t wind.

Considering that the resultant drag force along the propeller blade acts on the blade tip, the fan torque, for a propeller of radius  $\beta$  spinning on a velocity  $\Omega_i$ , is given by:

$$\tau_D = \frac{1}{2} R_m \rho C_D A v^2 \rightarrow \tau_D = \frac{1}{2} R_m \rho C_D A (\Omega R_m)^2 \rightarrow \tau_D = b \Omega^2 \quad (2.4.11)$$

Hence, the drag torque on the propeller is proportional to the square of the angular speed by a constant  $b$ . Thus, the resultant drag torque on the motor reference frame is:

$$\vec{\tau}_{F_{MCS}} = \begin{bmatrix} 0 & 0 & \sum_{i=1}^n -b \Omega_i^2 \end{bmatrix}^T \quad (2.4.12)$$

Finally, using transformation (2.1.10) on Eq. (2.4.12), the fan torque on the *BCS* is obtained:

$$\vec{\tau}_F = \begin{bmatrix} \sum_{i=1}^n -\text{sign}(\Omega_i) (\sin(\gamma_i) \sin(\beta_i) + \cos(\gamma_i) \sin(\alpha_i) \cos(\beta_i)) b \Omega_i^2 \\ \sum_{i=1}^n -\text{sign}(\Omega_i) (-\cos(\gamma_i) \sin(\beta_i) + \sin(\gamma_i) \sin(\alpha_i) \cos(\beta_i)) b \Omega_i^2 \\ \sum_{i=1}^n -\text{sign}(\Omega_i) \cos(\alpha_i) \cos(\beta_i) b \Omega_i^2 \end{bmatrix} \quad (2.4.13)$$

Note that, the fan torque produced by each propeller depends on the spinning direction but, since the propeller angular speed is squared, the torque from each rotor has no sign differentiation. Thus, the *sign* function is added on Eq. (2.4.13) in order to define if the torque is clockwise or counter-clockwise.

## 2.5 Final Dynamical Model

Now, the forces and moments equations previously presented can be replaced on the Newton-Euler equations for linear and angular movement in order to obtain the full 6 D.O.F rigid body model written on the *BCS* (Eqs. (2.2.7) and (2.2.12)):

$$m \begin{bmatrix} \dot{u} - Rv + Qw \\ \dot{v} - Pw + Ru \\ \dot{w} - Qu + Pv \end{bmatrix} = \vec{T}_{BCS} + \vec{F}_D^{BCS} + \vec{F}_{grav}^{BCS} \quad (2.5.1)$$

$$\begin{bmatrix} J_{xx}\dot{P} + QR(J_{zz} - J_{yy}) \\ J_{yy}\dot{Q} + PR(J_{xx} - J_{zz}) \\ J_{zz}\dot{R} + PQ(J_{yy} - J_{xx}) \end{bmatrix} = \vec{\tau}_T + \vec{\tau}_G + \vec{\tau}_F \quad (2.5.2)$$

The six equations from (2.5.1) and (2.5.2) represents the translational and rotational aircraft dynamical model, respectively. Notwithstanding, the problem has 6 equations and 9 unknowns. In order to have a possible solution, the kinematic relations (Eq. (2.1.1)) are integrated to model completing the 9 equations. Further, the rotational matrices transformation ((2.1.6)) can be used to describe the aircraft movement in terms of the inertial coordinate system.

## 2.6 Linearization

As stated previously, the aircraft dynamical behavior is represented by Eqs. (2.5.1), (2.5.2) and (2.1.1), which are very coupled, nonlinear set of equations. However, in order to investigate the system performance and apply modern control techniques, the equations of motion must be linearized (Burns, 2001).

The linearization procedure is based on the small perturbation theory in which the aircraft is assumed slightly perturbed from its steady operating service (trimmed condition). Thus, the equations are expanded using Taylor Series truncated on first order derivatives, so that a general variable might be expressed as:

$$f = f_0 + \tilde{f} \quad (2.6.1)$$

where  $f_0$  is the reference trimmed value and  $\tilde{f}$  is the perturbed variable. The above relation is substituted in the nonlinear equations of motions and the  $(\sim)$  is later eliminated from the equations for the sake of simplicity.

In most of the applications concerning trajectory-tracking problems (Valavanis, 2007), the position of the aircraft with respect to the ICS is needed. In order to include the vehicle position as a generalized coordinate of the dynamical problem, three new relations are added to the equations of motion. They concern the linear velocities  $(u, v, w)$  that are written as a function of the temporal derivatives of  $(x, y, z)$  (Etkin, 1995) .

After the nonlinear equations were linearized and written as a set of first order differential equations, the system can be characterized in the matrix space state form as:

$$\dot{\vec{x}} = A\vec{x} + B\vec{u} \quad (2.6.2)$$



$$B = \begin{bmatrix} 0 & \frac{k \sin \gamma_{i_{t1}} k \Omega_{0_{i_{t1}}}^2}{m} & \frac{k \cos \gamma_{i_{t1}} k \Omega_{0_{i_{t1}}}^2}{m} \\ 0 & \frac{k \cos \gamma_{i_{t1}} k \Omega_{0_{i_{t1}}}^2}{m} & \frac{k \sin \gamma_{i_{t1}} k \Omega_{0_{i_{t1}}}^2}{m} \\ 2k\Omega_{0_i} & 0 & 0 \\ \frac{2l_i \sin \gamma_i k \Omega_{0_i}}{J_{xx}} & \frac{b \sin \gamma_{i_{t1}} \Omega_{0_{i_{t1}}}^2}{J_{xx}} & \frac{b \cos \gamma_{i_{t1}} \Omega_{0_{i_{t1}}}^2}{J_{xx}} \\ \frac{2l_i \cos \gamma_i k \Omega_{0_i}}{J_{yy}} & \frac{b \cos \gamma_{i_{t1}} \Omega_{0_{i_{t1}}}^2}{J_{yy}} & \frac{b \sin \gamma_{i_{t1}} \Omega_{0_{i_{t1}}}^2}{J_{xx}} \\ \frac{2b\Omega_{0_i}}{J_{zz}} & \frac{-(\sin \gamma_{i_{t1}} + l_{i_{t1}} \cos \gamma_{i_{t1}}) l_{i_{t1}} k \Omega_{0_{i_{t1}}}^2}{J_{zz}} & 0 \\ 0 & 0 & 0 \\ 0 & 0 & 0 \\ 0 & 0 & 0 \\ 0 & 0 & 0 \\ 0 & 0 & 0 \\ 0 & 0 & 0 \end{bmatrix} \quad (2.6.7)$$

The state space model presented on Eqs. (2.6.2) and (2.6.3) represents a Multi-Input Multi-Output (*MIMO*), Linear Time Invariant (*LTI*) system containing 12 outputs and  $n + n_t$  inputs, which depends on the aircraft configuration. Now, modern control techniques can be applied in order to guarantee system stability and/or to track a desired command. The system analysis and control application are discussed on the next sections.



## Chapter 3

### Modern Control

Modern Control Theory has shown to be a valuable tool in aerospace industries for aircraft dynamic stabilization or autonomous flight operations. This control technique has efficiently been applied on commercial and military aircrafts, for instance, the Boeing 767 and the F-16 (Stevens and Lewis, 1992). Also, for MAVs application, the technique has revealed to be a valuable tool in the development of autonomous systems (Suiçmez, 2014).

Differently from fixed wing aircrafts, the multi-rotors are open-loop unstable and, therefore, must have a control loop integrated in order to make the flight possible. As presented in the previous chapter, the multi-rotor dynamics are represented as a *MIMO* system containing a large number of states and inputs. Therefore, the application of classic control techniques as PID control are unfeasible, since the controller is based on successively *SISO* transfer function closed loops. In this case, each loop gain should be selected individually by the designer using trial and error methods or optimization algorithms so that the design procedure becomes difficult.

According to Stevens and Lewis (1992), there are two central concepts to modern control system design. The first is that the design is based directly on the state-variable model introduced by Kalman (1960) (Eqs. (2.6.2) and (2.6.3)) and, just as stated by the authors, contains more information about the system than the input-output description.

The second central concept is the expression of performance specifications in terms of a mathematically precise criterion which then yields matrix equations for the control gains. These matrix equations are solved using computer algorithms so that all the loop control gains are computed simultaneously, guaranteeing the closed loop stability. In this case, the fundamental engineering decision is the selection of the suitable performance criterion based on the system response.

Practically speaking, the multi-copter system by itself is an unstable system which requires an embedded controller in order flight safely. For remotely controlled UAV applications, the

controller shall be designed to guarantee that the system maintain stability when a set of commands are given by the user. Also, the system must return to an equilibrium condition when there is no input command. Hence, on this application, a regulator controller may be useful.

On the other hand, there are some mission tasks on which it is desired that the aircraft is capable to operate autonomously. On this case, it is highly recommended to design a controller able to follow a desired reference trajectory in space or, in other words, the system shall be able to track a set of reference inputs signals.

In conclusion, since the autonomous flight operations has been one of the turning points of UAV applications, on this work, the modern control techniques are explored so that a multi-rotor is capable to track a desired trajectory on space.

Hence, this section deals with the formulation of modern control theory and its application on MAVs autonomous flight. For this, the minimum conditions of controllability and observability are presented in Section 3.1. Later, the Linear Quadratic Regulator problem is described in Section 3.2; then, on Section 3.3 the Linear Quadratic Tracking controller is derived using the servomechanism model considering that the system will be able to track different input signals.

### 3.1 Controllability and Observability

The concepts of controllability and observability were introduced by Kalman (1960) and play an important role in the control of multivariable systems.

According to Lewis and Stevens (1992), a system is said controllable when all its modes are affected by the control inputs  $\vec{u}(t)$  independently. In other words, when the controllability condition is satisfied, there exists a control vector  $\vec{u}(t)$  that transfers the system from any initial state  $\vec{x}(t_0)$  to some final state  $\vec{x}(t)$  in a finite time interval.

Thus, considering a state space system described by Eqs. (2.6.2) and (2.6.3); then, the controllability  $n_s \times n_s$  matrix is given by:

$$U = \begin{bmatrix} B & AB & A^2B & \cdots & A^{n_s-1}B \end{bmatrix} \quad (3.1.1)$$

Hence, for a system with  $n_s$  states, the system is controllable if the matrix  $U$  contains  $n_s$  linearly independents columns or rows, in other words,  $U$  has full rank  $n_s$ .

Similarly, a system is said observable if at time  $t_0$ , the system state  $\vec{x}(t_0)$  can be exactly determined from observation of the output  $\vec{y}(t)$  over a finite time interval. The system is completely observable if the  $n_s \times n_s$  observability matrix

$$O_b = \begin{bmatrix} C^T & A^T C^T & \dots & (A^T)^{n_s-1} C^T \end{bmatrix} \quad (3.1.2)$$

is of rank  $n_s$ , i.e. is non-singular having a non-zero determinant.

In order to design a controller based on modern control techniques, the conditions of observability and controllability must be satisfied and considered to ensure that the cost function is bounded on the domain (Burns, 2001).

### 3.2 Linear Quadratic Regulator

According to Lawretsky and Wise (2013), the Linear Quadratic Regulator (LQR) is one of the most widely used control design methods in aerospace. Several research studies have been performed comparing properties of controllers and have shown that the LQR method have some advantages as: good performance, robustness, and control usage minimization. In summary, the LQR controller provides an optimal control law for a linear system that satisfies a performance index condition.

#### 3.2.1 Quadratic Performance Index

The choice of the performance index depends upon the nature of the control problem. Lawretsky and Wise (2013) states that the notion of optimality is defined through the integral cost performance index ( $J$ ),

$$J = \int_{t_0}^T L(\vec{x}(\tau), \vec{u}(\tau), \tau) d\tau + S(\vec{x}(T)) \quad (3.2.1)$$

evaluated along the system trajectories  $\vec{x}(t)$  due to applied control input  $\vec{u}(t)$ . The instant cost  $L(\vec{x}, u, \tau)$  and the terminal cost  $S(\vec{x}(T))$  are defined as scalar nonnegative functions (e.g. quadratic functions) such that the cost  $J$  is a cumulative measure of the overall efforts (controls) and the state-energy spent to drive the system from its initial state  $\vec{x}_0$  to a neighborhood of the terminal condition  $S(\vec{x}(T)) = 0$ .

The minimization problem can be solved using the Principle of Optimality developed by Richard Ernest Bellman in the late 1950s, which states that: “an optimal policy has the property that whatever the initial state and initial decision are, the remaining decisions must constitute an optimal policy with regard to the state resulting from the first decision” (Bellman, 2003).

The main idea of the solution is to divide the minimization integral into time intervals and then each interval chose the optimal control input ( $u(t)$ ) that minimizes the overall cost  $J$ .

Considering the multi-rotor linearized dynamic model developed on Chapter 2, it is appropriate to adopt a quadratic performance index such as:

$$J = \int_0^{t_1} (x^T Q_k x + u^T R_k u) dt \quad (3.2.2)$$

being  $Q_k$  and  $R_k$  the state and control weighting matrices, which are always square and symmetric.

It is important to note that Eq. (3.2.2) considers the performance index for an infinite time minimization problem ( $t_1 \rightarrow \infty$ ); thus, the terminal condition is zero ( $S(x(T)) = 0$ ).

Briefly, there are three main reasons for the choice of the quadratic performance index function:

- the adopted function is always nonnegative on its domain;
- the energy associated to the system response and the input demand becomes more apparent;
- there are well known solutions for this type of function in the literature such as the Riccati equations.

Another quadratic cost function advantage is that, for linear systems, the solution is a linear control law defined by:

$$\vec{u}(t) = -K\vec{x}(t) \quad (3.2.3)$$

where  $[K]_{n_u \times n_x}$  is a constant matrix gain containing all the  $LQR$  optimal feedback gains.

Additionally, the weighting matrices  $Q_k$  and  $R_k$  are chosen to be positive semidefinite, i.e. their eigenvalues of a generic  $M$  matrix are positive and the quadratic form  $\vec{x}^T M \vec{x}$  are also positive for every value of  $\vec{x}$ ; hence, the scalar  $J$  is always positive.

Since the solution of Eq. (3.2.2) is a minimization problem, the relative magnitudes of  $Q_k$  and  $R_k$  matrices becomes a trade-off relation. For instance, a larger control-weighting matrix  $R_k$  will make it necessary for  $\bar{u}(t)$  to be smaller to ensure that  $\sqrt{R_k}\bar{u}(t)$  is close to zero. Thus, the matrix  $R_k$  penalizes the controls efforts. On other hand, to make the states ( $\bar{x}(t)$ ) goes to zero more quickly with time, a larger magnitude of  $Q_k$  may be selected. In conclusion, the choices of  $Q_k$  and  $R_k$ , weights the effects of state on control variables magnitudes, affecting the position of the closed-loop poles and, consequently, the dynamical behavior of the system.

### 3.2.2 The Regulator Problem

In summary, the *LQR* problem consists in the following. Given a linear state space system, find the feedback coefficient  $K$  in the input control law that minimizes the value of the performance index Eq. (3.2.2).

Considering the quadratic performance index (Eq. (3.2.2)) on an infinite time interval where the final time is  $t_1 = \infty$  and that the system state dynamics being *LTI* (Linear Time Invariant), i.e. the state matrices  $A$  and  $B$  presented on Eqs. (2.6.6) and (2.6.7) are constant, it is possible that the corresponding Riccati equation:

$$\dot{\tilde{P}}(t) = -\tilde{P}(t)A - A^T\tilde{P}(t) - Q_k + \tilde{P}BR_k^{-1}B^T\tilde{P}(t) \quad (3.2.4)$$

being  $\tilde{P}(t) = \tilde{P}^T(t) > 0$  a  $n_s \times n_s$  matrix, with the limiting boundary condition

$$\lim_{T \rightarrow \infty} \tilde{P}(T) = 0_{n_s \times n_s} \quad (3.2.5)$$

has a unique solution (Burns, 2001).

Moreover, as  $t \rightarrow \infty$ , this solution tends to a constant symmetric matrix, which can be found by solving the algebraic Riccati equation:

$$\tilde{P}A + A^T\tilde{P} + Q_k - \tilde{P}BR_k^{-1}B^T\tilde{P} = 0 \quad (3.2.6)$$

For Eq. (3.2.6), the *LQR* optimal control policy in the feedback form is:

$$\bar{u}_{opt} = -R_k^{-1}B^T\tilde{P}\bar{x} \quad (3.2.7)$$

Comparing Eqs. (3.2.7) and (3.2.3), it can be inferred that the *LQR* optimal matrix gain is given by:

$$K = R_k^{-1} B^T \tilde{P} \quad (3.2.8)$$

The linear quadratic regulator block diagram is illustrated on Figure 3.1. From the figure, it can be noted that the closed loop structure consists on a state variable feedback system where the plant output ( $\vec{y}(t)$ ) feeds the controller input, which multiplies it by the gain matrix ( $K$ ) outputting the input command ( $\vec{u}(t)$ ) to the plant. It is important to highlight that in this case it is considered that the state vector is the same as the output vector, i.e. all the state variables can be monitored.

Also, substituting the optimal feedback control (Eq. (3.2.3)) into the open loop dynamics (Eq. (2.6.2)) gives the closed-loop system:

$$\dot{\vec{x}} = (A - BK)\vec{x} = A_{cl}\vec{x} \quad (3.2.9)$$

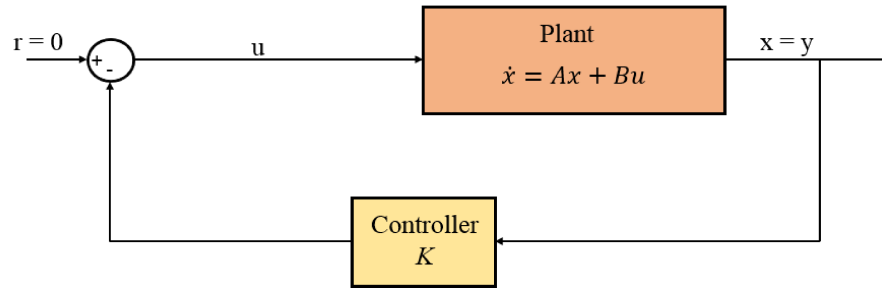


Figure 3.1 - Linear Quadratic Regulator block diagram (Adapted from Burns, 2001).

Practically speaking, the regulator controller purpose is to restore the system, which was initially perturbed from the equilibrium condition, to the equilibrium state in such a manner so as to minimize a given performance index. Thus, the *LQR* formulation guarantees that all the poles of the closed loop system (the eigenvalues of  $A_{cl}$  matrix) are stable, i.e. considering the  $\text{Im} \times \text{Re}$  plane the poles are on the left-hand side of the imaginary axis ( $\text{Re}(\lambda(A_{cl})) < 0$ ). As a consequence, the system states variables, which on this case are the perturbed state variables operating around a trimmed condition, are regulated to zero (equilibrium position). Hence,  $\vec{x} \rightarrow 0$  as  $t \rightarrow \infty$ , which implies  $\vec{u} \rightarrow 0$  as  $t \rightarrow \infty$ , forming a type 0 control system.

### 3.3 Tracking a Command

Regarding multi-rotor UAVs, for autonomous flights applications, the control system is required to accurately track a desired command or a pre-established space trajectory, which are often represented as a set of differential equations. This requirement distinguishes these problems from regulation in which the states are driven to the equilibrium point.

It is known, from classical control theory, that in order to track a constant command with zero steady state error, an integral error control action must be added into the controller, augmenting the type number of the system. This control property depends upon the order of  $p_i$  poles and represents how many integrators are present in the system. Thus, to track commands accurately, the class of commanded signals must be known, and the controller must be augmented with enough integrators to produce zero steady-state errors.

The augmentation of the system with integrators for command tracking requires embedding into the system a model of the class of signals that the system will track. This is often referred to as the *internal model principle* (Francis and Wonham, 1976).

Also, Davidson and Copeland (1985) purposes a systematic process for building an augmented state space model known as the *servomechanism design model*. Later, the system is decomposed in two main parts: a servo tracking controller for command following and a state feedback component for stabilization.

Now, considering the state-space model presented on Eqs. (2.6.2) and (2.6.3), a subset of the output vector  $y$  is selected as the desired variables to track ( $y_c$ ) the reference input vector  $r$ , which is assumed to have the dimension less than or equal to the number of the system outputs (i.e.  $n_s \geq n_r$ ). Further, the reference command can be expressed as an  $p^{th}$  order differential equation with the following model:

$${}^{(p)}r = \sum_{i=1}^p a_i {}^{p-i}r \quad (3.3.1)$$

where the scalar coefficients  $a_i$  are known and the superscript ( $i$ ) denotes the  $i^{th}$  derivative. Using the model presented on Eq. (3.3.1), examples for typical reference input signals are shown on Table 3.1.

The tracking error signal can be defined as:

$$\vec{e} = \vec{y}_c - \vec{r} \quad (3.3.2)$$

The error signal is defined as above in order to apply negative feedback of the errors and their derivatives in forming the feedback control. The output vector can be arranged so that the first  $n_r$  variables in  $y$  define  $y_c$ . Thus, the model for  $y_c$  is:

**Table 3.1 Internal model for command generation.**

Command Signal $r(t)$	Differential Equation	Model Parameters
Constant (step)	$\dot{r} = 0$	$p = 1, a_1 = 0$
Ramp	$\ddot{r} = 0$	$p = 2, a_1 = a_2 = 0$
Sinusoid	$\ddot{r} = -\omega_0^2 r$	$p = 2, a_1 = -\omega_0^2, a_2 = 0$

$$\bar{y}_c = C_c \bar{x} + D_c \bar{u} \quad (3.3.3)$$

This is the desired regulated system output, in other words, tracking  $\bar{y}_c$  is the same as regulation in  $\bar{e}$ . Therefore, the objective is to make the error approach zero  $\bar{e} \rightarrow 0$  or  $\bar{y}_c \rightarrow \bar{r}$ , as  $t \rightarrow \infty$ .

The servomechanism design model is formed by creating a new state space model, containing the error dynamics and the  $p^{\text{th}}$  time derivatives of the original state space system. So, the new state variables and control inputs can be defined as:

$$\bar{\xi} = \bar{x} - \sum_{i=1}^p a_i^{(p-i)} \bar{x} \quad (3.3.4)$$

$$\bar{\mu} = \bar{u} - \sum_{i=1}^p a_i^{(p-i)} \bar{u} \quad (3.3.5)$$

Since the system is *LTI*, the error is a linear combination of  $\bar{\xi}$  and  $\bar{\mu}$ ; hence, a new state vector  $\bar{z}$ , with dimension  $(n_s + p \times n_r)$ , is defined and its components are the errors  $\bar{e}, \dots, \bar{e}^{(p-1)}$  and the vector  $\bar{\xi}$ :

$$\bar{z} = \begin{bmatrix} \bar{e} & \dot{\bar{e}} & \dots & \bar{e}^{(p-1)} & \bar{\xi} \end{bmatrix}^T \quad (3.3.6)$$

Finally, the servomechanism design model is obtained differentiating the augmented state vector  $\bar{z}$ , so that the new space state model will be:



$$\dot{\vec{z}} = \tilde{A}\vec{z} + \tilde{B}\vec{\mu} \quad (3.3.7)$$

where  $\tilde{A}$  and  $\tilde{B}$  are respectively given by:

$$\tilde{A} = \begin{bmatrix} 0 & I & 0 & \cdots & 0 & 0 \\ 0 & 0 & I & & 0 & 0 \\ & & \ddots & & & \\ 0 & 0 & & 0 & I & 0 \\ a_p I & a_{p-1} I & \cdots & a_2 I & a_1 I & C_c \\ 0 & \cdots & \cdots & \cdots & 0 & A \end{bmatrix} \quad (3.3.8)$$

$$\tilde{B} = \begin{bmatrix} 0 \\ 0 \\ \vdots \\ 0 \\ D_c \\ B \end{bmatrix} \quad (3.3.9)$$

Assuming that the control law for the servomechanism system is represented by:

$$\vec{\mu}(t) = -K_c \vec{z}(t) \quad (3.3.10)$$

The feedback matrix gain is calculated using the optimal control policy presented in Eq. (3.2.7). The resulting  $K_c$  matrix is partitioned in the same manner as the vector  $\vec{z}$  :

$$K_c = [K_p \quad K_{p-1} \quad \cdots \quad K_1 \quad K_x] \quad (3.3.11)$$

where  $K_p \cdots K_1$  is the integral error control matrices and  $K_x$  is the stabilization matrix of the original system plant (Eqs. (2.6.6) and (2.6.7)).

Figure 3.2 illustrates the block diagram of the servomechanism system for  $p$  integrators. The control loop inside the red square represents the regulator which guarantees the states stability. On the other hand, the control loop inside the blue square contains the error integral control and that forces the desired control states ( $y_c$ ) to follow a given reference input signal. Note that the number of integrators in the control loop depends on the  $p^{th}$  order of the differential equations and all the gain matrices are obtained simultaneously as presented in Eq. (3.3.11).

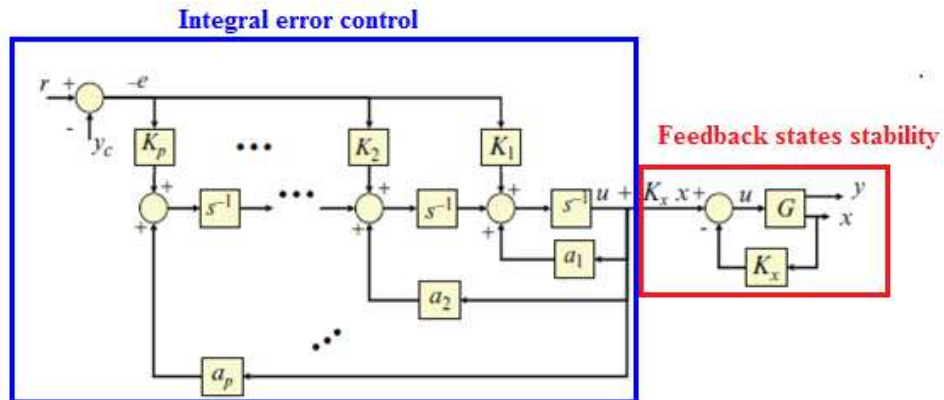


Figure 3.2 - Servomechanism system block diagram (adapted from: Lavretsky and Wise, 2013).

## Chapter 4

### Apparatus and Procedures

The derived dynamical model and control theory application will be evaluated concerning the stability properties for different input signals. Thus, a numerical simulation can be implemented using Matlab / Simulink<sup>®</sup> interface in order to obtain preliminary results which will illustrate the dynamical behavior of the open and closed loop system. The numerical platform will be constructed in such manner that different multi-copter configurations and different reference input signals can be tested.

Thus, the main goal of this section is to present the apparatus and procedures used for the model and control law validation.

#### 4.1 The Multi-rotor

For the analysis, the chosen multi-copter configuration is a quadcopter MAV, as presented in Fig. 4.1, developed by the *Laboratório de Aeronaves Autônomas* (LAA) from the Federal University of Uberlândia and has been a research object of the research group.

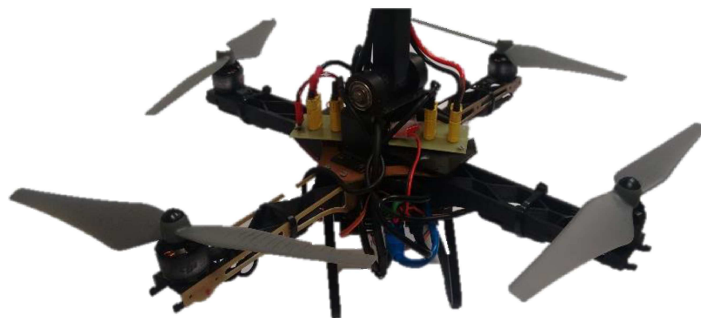


Figure 4.1 Quadcopter MAV.

### 4.1.1 Quadcopter Structure

The preliminary concept design was proposed by Costa (2016) where the mechanical optimization of the arms was explored. The platform was designed with aid of a CAD software and manufactured using Printed Circuit Boards (PCB) and ABS such that, most of the components, could be built using a 3D printer. As a result, the structure is 624 mm in span and about 135 mm in height as illustrated in Fig 4.2.

Regarding the physical properties, the quadcopter mass was measured using a scale while the inertia properties was estimated from the CAD model. The aircraft mechanical properties are summarized in Table 4.1.

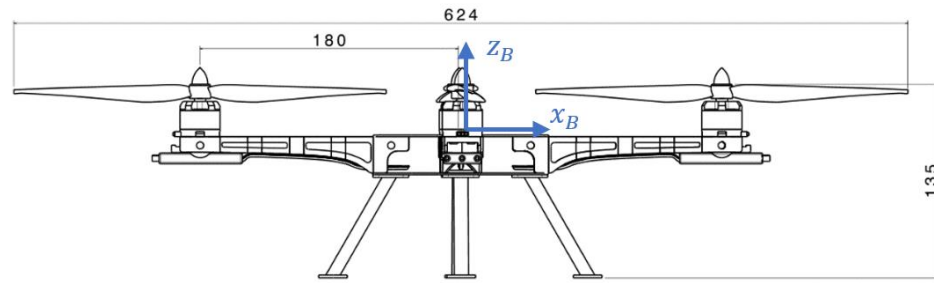


Figure 4.2 Quadcopter side view.

Table 4.1 Quadcopter parameters.

Property	Parameter	Value	Unit [SI]
Number of rotors	$n$	4	-
Mass	$m$	0.620	kg
Inertia on $x_b$ axis	$J_{xx}$	0.007	kg.m <sup>2</sup>
Inertia on $y_b$ axis	$J_{yy}$	0.007	kg.m <sup>2</sup>
Inertia on $z_b$ axis	$J_{zz}$	0.013	kg.m <sup>2</sup>
Drag coefficient	$k_d$	4.8e-3	N.s <sup>2</sup>
Arm length	$l$	0.180	m

### 4.1.2 Propulsion System

The quadcopter propulsion system is composed of 4 DJI® 2212/920 KV brushless DC motors equipped with E300 ESC system and plastic model 9443 240 mm spam propellers. The motor thrust coefficient and transfer function (Pulse Width Modulation (PWM) signal to spinning

angular speed) were obtained experimentally using a test bench as presented in Appendix A. Table 4.2 shows the E300 mechanical and operational properties.

The ESCs are connected to a power source (for external mission operations a 3S or 4S LiPo battery) and to a PWM output from the microcontroller.

**Table 2 DJI® E300 properties.**

Property	Parameter	Value	Unit [SI]
Recommended load	$T_{nom}$	300	g/axis
Maximum thrust	$T_{max}$	600	g/axis
Current	$i_m$	15	A
Voltage	$V_m$	11.1~14.8	V
Thrust coefficient	$k$	8.901e-6	Ns <sup>2</sup>
Propeller moment of inertia	$J_m$	4.025e-5	kg.m <sup>2</sup>
Propeller drag coefficient	$b$	1.1e-6	Nms <sup>2</sup>
Arm length	$l$	0.180	m

### 4.1.3 Microcontroller

For control operations, the chosen microcontroller was a BeagleBone Green board (Fig. 4.3) equipped with a Texas Instruments Sitara AM3358 processor with maximum speed of 1 GHz and a 512 MB DDR3 RAM. The board also contains 7 analog I/O pins, 65 digital I/O and 8 PWM I/O. The BeagleBone Green main advantages over others microcontrollers (Arduino, Raspberry Pi, etc.) are: the processor capability, the number of PWM outputs, the board is preloaded with a Linux operating system, the capability to interact with external sensors and an ethernet connection boosting up the communication between the microcontroller and a PC device (Kumar, 2015). As a result, the BeagleBone board is a good choice for projects that want both the functionality of Linux (such as networking and USB) and real-time behavior for controlling physical systems.

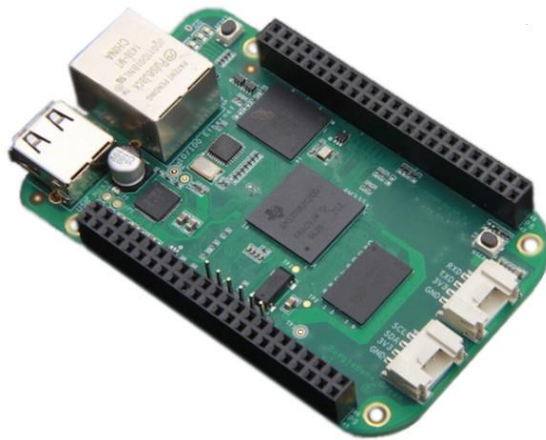


Figure 4.3 BeagleBone Green microcontroller board (Brown, 2015).

#### 4.1.4 The Tilting Mechanism

The quadcopter arm developed in Costa (2016) did not contemplate the tilting capability of the rotors. Hence, a tilting mechanism was designed so that the rotors are able to tilt longitudinally (rotation about  $y_m$  axis) with the aid of an actuator. The choice of this configuration mechanism was essentially based on construction facility once the multi-copter arm has already been manufactured. The mechanism was printed on ABS using a 3D printer and weights approximately 12 g. The mounting mechanism dimensions are presented in Fig. 4.4 and it can be attached to the quadcopter arm at the rotating point  $O_T$ . The rotor arm distance to the quadcopter  $CG$  was preserved.

So, the motor set (DC motor and propeller) is attached to the motor support (see Fig. 4.4) so that, when the actuator rotates, the connection rod rotates the motor bed around point  $O_T$ , tilting the rotor around the point. It is important to note that the distance relations from the actuator connection point and the motor  $CG$  to point  $O_T$  are related to the control effectiveness.

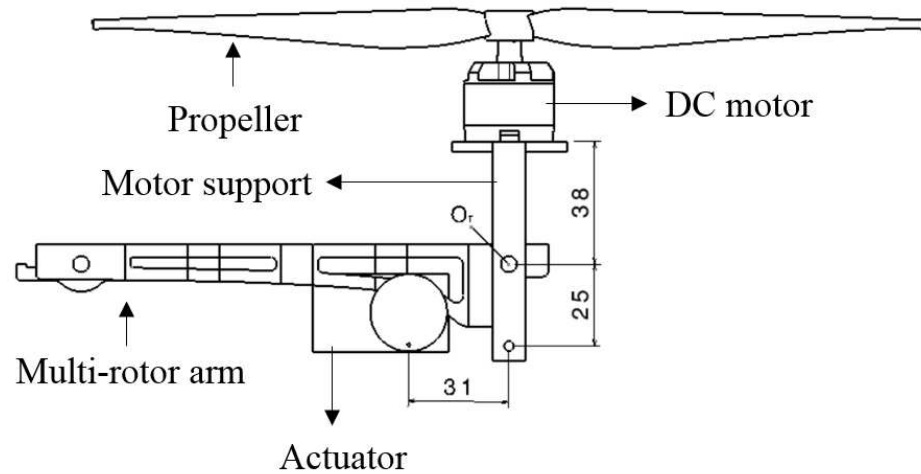


Figure 4.4 The tilting mechanism and its dimensions in *mm*.

The tilting mechanism is driven by a Hitec<sup>®</sup> HS-65MG actuator that is connected to the motor bed by a rigid rod as illustrated in Fig. 4.5 permitting the bed rotation from 25 deg (left) to -50 deg (right). Also, the actuator is connected to the PWM microcontroller output so that its position can be set varying the signal pulse-width. The actuator specifications are presented in Table 4.3.

Table 4.3 HS-65MG actuator specifications.

	At 4.8V	At 6V
Speed	0.14s/60°	0.11s/60°
Torque	1.8 kg.cm	2.2 kg.cm
Weight	12.5 g	
Dimension	23.6 x 11.6 x 24 mm	

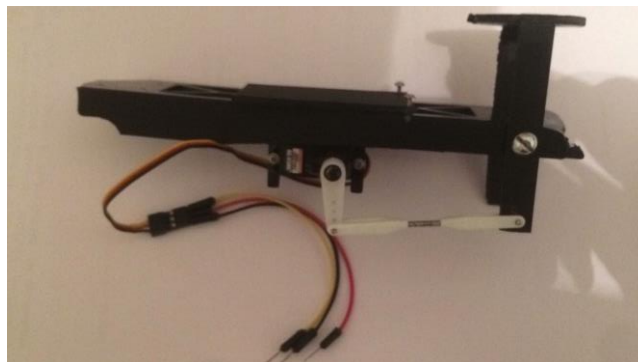


Figure 4.5 Tilt rotor mechanism assembly.

### 4.1.5 Inertial Measuring Unit

An inertial measurement unit (IMU) is an electronic device that uses a combination of accelerometers and gyroscopes to measure and report a body's specific force, angular rate and sometimes the magnetic field surrounding the body.

The MPU-60X0 (Fig. 4.6) is an integrated 6 motion tracking device that combines a 3-axis gyroscope, 3-axis accelerometer, and a digital motion processor (DMP). For precision tracking of both fast and slow motions, the parts feature a user-programmable gyroscope full-scale range of  $\pm 250$ ,  $\pm 500$ ,  $\pm 1000$ , and  $\pm 2000$  °/sec and a user-programmable accelerometer full-scale range of  $\pm 2g$ ,  $\pm 4g$ ,  $\pm 8g$ , and  $\pm 16g$ . The IMU is connected to the microcontroller via the VCC, GND, SDA and SCL pins.

Moreover, the Euler angles ( $\Theta = [\phi \ \theta \ \psi]^T$ ) and the angular velocities ( $\vec{\omega} = [P \ Q \ R]^T$ ) can be estimated from the IMU acquired data, providing attitude guidance to the aircraft. Once the obtained raw data is very noisy, the controller is not sufficiently robust to compensate the disturbance. Thus, the output signal from the IMU is filtered using a Kalman Filter.



Figure 4.6 IMU device.

## 4.2 Numerical Simulations

Initially, a Matlab<sup>®</sup> routine was developed to calculate the LQT controller gain matrix from the state space model (Eqs. (2.6.6) and (2.6.7)). As shown in the equations, the state space model depends on the aircraft physical properties, the number of actuators (electrical motors and tilting mechanisms), the trimming conditions and the type of input signal to be tracked. All these parameters must be defined by the user and, once the augmented state space model is defined, the LQR problem is solved using the Ricatti equations in order to determine the control gain matrices. Thus, this routine allows the user to test different aircraft configurations and compare their



dynamical behavior for several conditions. For instance, vary the number of tilting mechanisms, motor propulsive set and also the mechanical properties as mass, inertia, etc.

For this purpose, a Matlab/Simulink<sup>®</sup> model was designed as illustrated in Fig. 4.7. The Simulink platform disposes the “Custom Variable Mass 6 DOF” toolbox which represents the 6 DOF Newton Euler set of equations (2.1.1, 2.1.4, 2.2.7 and 2.2.12) on cartesian coordinates for a rigid body, which can be integrated over time using a standard numerical solver. In this case, the selected solver is the ODE45 which integrates the equations over time via an explicit Runge-Kutta or Dormand-Prince method with variable time steps. The output from the 6 DOF toolbox are: velocities and positions w.r.t. *ICS* ( $\vec{V}_E = [V_x \ V_y \ V_z]^T$  and  $\vec{X}_E = [x_E \ y_E \ z_E]^T$ , respectively), the Euler angles ( $\Theta = [\phi \ \theta \ \psi]^T$ ), angular and linear velocities w.r.t. *BCS* ( $\vec{\omega} = [P \ Q \ R]^T$  and  $\vec{v} = [u \ v \ w]^T$ , respectively). All the output variables complete the space state vector Eq. (2.6.4).

Meanwhile, the input for the 6 DOF toolbox are the rigid body mass and inertia properties and also external forces and moments applied to the model *CG*. Thus, on these circumstances, two Matlab<sup>®</sup> Function toolboxes were added in order to calculate the forces and moments for a given input signal from the controller respecting the formulation derived on Sections 2.3 and 2.4.

The control loop is detailed on Fig. 4.8. In the figure is represented how the reference input is compared to the feedback states values and the multiplied by the gain matrices, integrated and summed to give the output actuation control signal which goes to the Forces and Moments calculation function. It may be regarded that, even the controller being designed over a linear state space model, the simulations are performed using the non-linear model.

The output from the 6 DOF model feedbacks the controller part where it is compared to the input signal and later is multiplied by the gain matrices and integrated following the LQT rule as described on Section 3.3. The output from the controllers are the input commands (Eq. (2.6.5)) that are fed to the forces and gain block closing the loop.

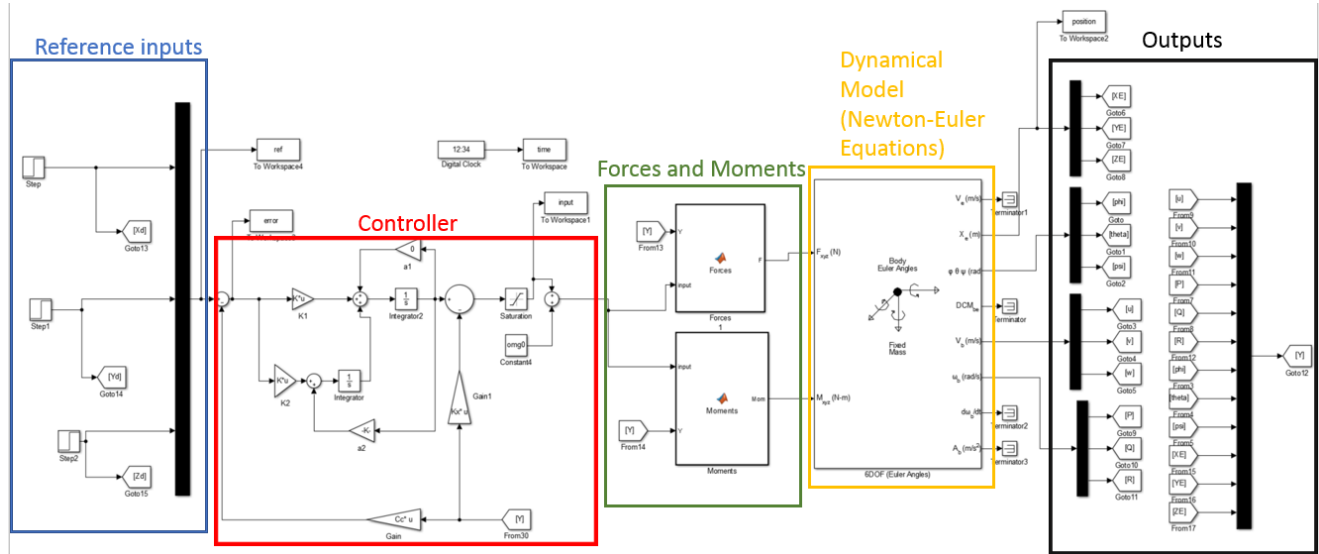


Figure 4.7 Matlab/Simulink block diagram.

In conclusion, the designed Matlab<sup>®</sup> routine permits control law gain matrices to be calculated offline for different configurations while the Simulink model enables the numerical simulation using a nonlinear model. Therefore, some physical effects that were not previewed on the linearized model will affect the controller behavior, such as the gyroscopic effect and coupled variables. Further, the numerical analysis will be closer to the real problem and the controller robustness to perturbations can be observed. However, it must be stated that, due to the non-linearity level of the plant, the simulations may be susceptible to integration or numerical errors.

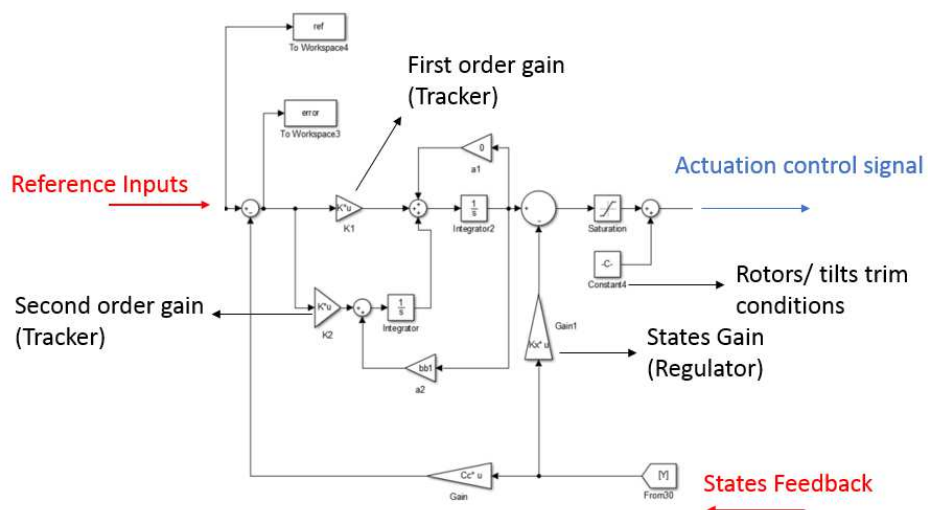


Figure 4.8 LQT controller diagram.

## Chapter 5

### Results and Discussions

In this chapter, the control technique presented on Chapter 3 will be tested by numerical simulations and the obtained results analyzed. The main goal of the analysis is to evaluate the stability and performance of the controller for different tilt-rotor configurations (no tilt mechanism, tilting laterally and tilting longitudinally) and subjected to diverse reference trajectories.

The object of study is the quad-copter aircraft described on Chapter 4 containing all physical parameters.

#### 5.1 Checking Controllability and Observability

As discussed on Chapter 3 the controllability and observability conditions of a given system must be satisfied, otherwise the control cannot stabilize the system and perform as desired. Thus, the conditions of controllability and observability were checked for three different scenarios: no tilt mechanism, 4 and 2 tilting mechanisms laterally ( $\beta$ ) and 4 and 2 tilting mechanisms longitudinally ( $\alpha$ ). It is important to state that the position of the tilting mechanism affects the system dynamics and, for the cases with only 2 tilting mechanisms, they were positioned on two arms 90 deg to each other.

The state-space system matrices ( $A$  and  $B$ ) are obtained substituting the aircraft parameters from Chapter 4 on Eqs. (2.6.6) and (2.6.7) and it is considered that all the states can be measured so matrix  $C$  is  $I_{12 \times 12}$ . Later, the controllability matrix is derived from Eq. (3.1.1). Once again, for a system with  $n_s$  states, the system is controllable and observable if the matrices  $U$  and  $O_b$  contains  $n_s$  linearly independents columns or rows, in other words,  $U$  and  $O_b$  have full rank  $n_s$ . On this case,  $n_s = 12$  assuming the state vector from Eq. (2.6.4). The rank of matrices  $U$  and  $O_b$  for all 5 scenarios are presented on Table 5.1.

It can be inferred from Table 5.1 that the system without and with longitudinal tilting mechanism does not accomplish the controllability conditions even though the observability is guaranteed. This implies that the system is not bounded and its response can diverge over time. On the other hand, the controller with lateral tilt mechanism has full rank for both 2 cases, so the system is called controllable.

**Table 5.1 - Controllability and Observability conditions.**

Configuration	Rank $O_b$	Rank $U$
No tilt	12	11
2 laterally ( $\beta$ )	12	12
4 laterally ( $\beta$ )	12	12
2 longitudinally ( $\alpha$ )	12	11
4 longitudinally ( $\alpha$ )	12	11

Analyzing only the controllability conditions, it is not possible to identify which of the states is not being controlled. However, looking at the linearized dynamical model, it can be observed that the yaw movement dynamics, including its respective angular rate, is dynamically independent from the other states. This fact can be verified looking at line 6 matrix  $A$  from Eq. (2.6.6) which is completed only by zeros.

Hence, the uncontrollability problem can be related with the yaw actuation mechanism. When the system has no tilt mechanism, the yaw torque is relied on the propeller drag coefficient ( $b$  parameter), which is very low. However, when the lateral tilt mechanism is added to on the multi-copter, the system becomes controllable since the yaw response due to the tilt angle variation is much more effective compared to the propeller drag response as observed on Fig. 5.1.

Thus, considering the stated problem, the equations for yaw movement (lines and columns 6 and 9 from matrix  $A$ ) are removed from the state-space system in a way that the LQR problem can be solved satisfactorily (controllability and observability guaranteed) and the system response converges to stability. Table 5.2 compares the observability and controllability conditions for the three uncontrollable cases considering the model without the yaw dynamics (i.e.  $\psi(t)$  and  $R(t)$ ).

Thus, as shown on Table 5.2, the controllability and observability conditions are satisfied for the three cases when the yaw dynamics are not included in the model. Nevertheless, if the system does not have a yaw control, its response will become unstable since the aircraft will be able to spin around itself freely. Hence, to solve this problem, a separate controller can be designed separately just to guarantee that the yaw movement is stable. This design will be discussed later.

**Table 5.2 - Controllability and Observability conditions without considering yaw dynamics.**

Configuration	Rank $O_b$	Rank $U$
No tilt	10	10
2 longitudinally ( $\alpha$ )	10	10
4 longitudinally ( $\alpha$ )	10	10

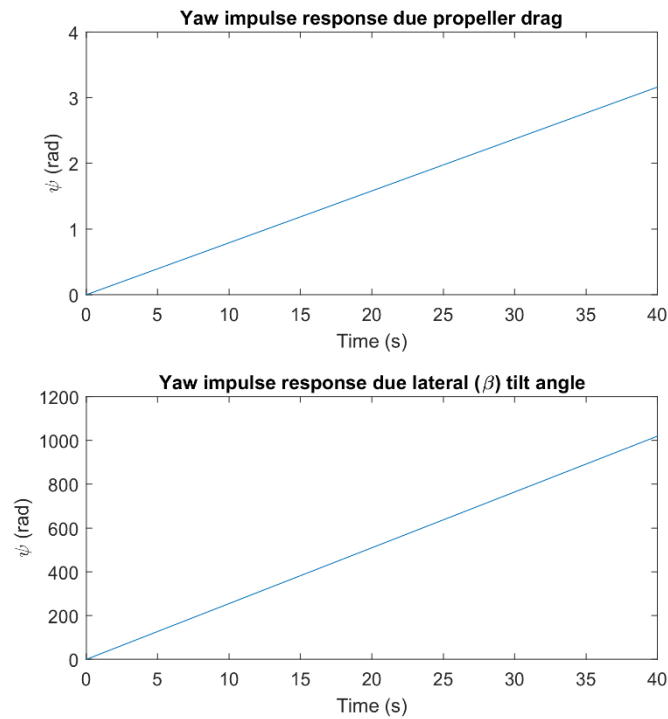


**Figure 5.1 - Yaw impulse response due propeller drag and lateral tilt deflection.**

## 5.2 Step Input Position Signal

As soon as the controllability and observability conditions were satisfied, the trajectory tracking control design can be proceeded using the servomechanism design model presented on Chapter 3. The main goal for the trajectory control is to make the aircraft to follow a reference input signal containing a set of inertial positions ( $x_E$ ,  $y_E$  and  $z_E$ ). Thus, the output matrix  $C_c$  is defined as:

$$C_c = \begin{bmatrix} [0]_{3 \times (ns-3)} & [I]_{3 \times 3} \end{bmatrix} \quad (5.2.1)$$

where  $n_s$  is the number of states to be controlled that for no tilt and longitudinal tilt is 10 and for lateral tilt is 12.

The control is designed by expanding the state vector  $\vec{x}(t)$ , considering the error dynamics represented by the difference between the reference and actual position of the aircraft, as presented on Chapter 3. Consequently, the error relies on the considered input signal differential equation as presented on Table 3.1.

The first reference command signal tested is a step input which, from Table 3.1, has the differential equation represented by  $\dot{r} = 0$  with the model parameters  $p=1$  and  $a_1 = 0$ . Now, the expanded space state matrices  $\tilde{A}$  and  $\tilde{B}$  can be written as presented on Eq. (3.3.8) and (3.3.9) considering  $D_c = [0]_{3 \times ni}$  ( $ni$  = number of input signals).

### 5.2.1 Choice of Weighting Matrices

Later, to solve the LQR problem the weighting matrices  $Q_k$  and  $R_k$  must be given. According to Steven and Lewis (1992) a good option to choose the weighting matrices is to write both as diagonal matrices and each element chosen as:

$$q_i = \frac{1}{e_{tol i}^2}, r_i = \frac{1}{inp_{tol i}^2} \quad (5.2.2)$$

where  $e_{tol i}$  is the error tolerance for each state and  $inp_{tol i}$  is the deviation tolerance for each input signal.

Even that Eq. (5.2.2) gives a good approximation for the choice of  $Q_k$  and  $R_k$  elements, good values are adjusted using trial and error method based on good tracking performance. For

comparison purposes the values of  $Q_k$  will be maintained for the three evaluated scenarios (no tilt, tilting laterally and longitudinally) while  $R_k$  diagonal values will vary according to the actuation mechanism response. Thus, on this case, from Eq. (3.3.6) the expanded state space vector is represented by:

$$\bar{z} = [e_x \ e_y \ e_z \ \dot{u} \ \dot{v} \ \dot{w} \ \dot{P} \ \dot{Q} \ \dot{R} \ \dot{\phi} \ \dot{\theta} \ \dot{\psi} \ \dot{x}_E \ \dot{y}_E \ \dot{z}_E]^T \quad (5.2.3)$$

Thus, the values for  $Q_k$  and  $R_k$  matrices chosen are:

$$Q_k = \text{diag}[0.5 \ 0.5 \ 10 \ 10 \ 10 \ 20 \ 2500 \ 250 \ 500 \ 50 \ 50 \ 50 \ 1000] \quad (5.2.4)$$

$$R_k = \text{diag}[[\rho_k]_n \ [\sigma_k]_{nt}] \quad (5.2.5)$$

where  $\rho_k$  and  $\sigma_k$  are the weighting values for each motor and tilting mechanism (either longitudinal or lateral), respectively. The chosen values are:

$$\rho_k = [0.05 \ 0.02 \ 0.008 \ 0.002] \quad (5.2.6)$$

$$\sigma_k = [50 \ 50 \ 50 \ 50] \quad (5.2.7)$$

Remembering that, for a well posed problem, it is important to check if the unstable modes are observable through the state penalty matrix, i.e. if  $\left(A_x, Q_k^{\frac{1}{2}}\right)$  is detectable. Hence, for the picked  $Q_k$  matrix, the rank of the detectability matrix is 13, meaning that the system is detectable.

### 5.2.2 Pole and Zeros Location Analysis

One method to evaluate the stability of MIMO system is to examine the poles and zeros of the closed-loop transfer function. As presented on Chapter 3, the closed-loop system is represented by Eq. (3.2.9). Then, the closed loop poles can be determined obtaining the eigenvalues ( $\lambda$ ) of the closed loop matrix ( $A_{cl}$ ) through the following eigenvalue problem:

$$A_{cl}v = \lambda v \quad (5.2.8)$$

being  $v$  the eigenvector of the closed loop system. Since linear system response is a combination of the eigen solutions, it can be stated that

$$x(t) = C_1 e^{\lambda_1 t} + C_2 e^{\lambda_2 t} + C_3 e^{\lambda_3 t} + \dots C_n e^{\lambda_n t} \quad (5.2.9)$$

being  $C_1, C_2 \dots C_n$  and  $\lambda_1, \lambda_2 \dots \lambda_n$  complex constant values.

Regarding the values of  $\lambda$ , the exponentials from Eq. (5.2.9) assumes solutions that are oscillatory and/or decaying exponentially amplitudes. Also, assuming that the frequency of the damped oscillations can be written as:

$$\lambda_j = -\omega_{nj} \left( \zeta_j \pm i \sqrt{1 - \zeta_j^2} \right) \quad (5.2.10)$$

where  $\omega_{nj}$  and  $\zeta_j$  are the natural frequencies and the damping ratios of  $i$ -th mode (eigenvector related to each eigenvalue).

On the cases where  $\zeta = 0$ , the system is considered undamped and a harmonic response is expected. If  $\lambda$  is complex and  $0 < \zeta < 1$ , the solutions are a decaying exponential combined with an oscillatory and the system is considered underdamped. Finally, when  $\lambda$  is pure real ( $\zeta > 1$ ), the solutions are simply a decaying exponential with no oscillation and the system is referred to as overdamped.

First, checking the open-loop poles of the linearized system, i.e. the eigenvalues of  $A$  matrix, it has 3 poles at  $\lambda = -0.006$  while the other are at  $\lambda = 0$  even if the yaw dynamics is included. Hence, the system has a decaying oscillatory response for some modes ( $\lambda = -0.006$ ), which may be related to the linear velocity due to drag effect, and a steady response for others ( $\lambda = 0$ ).

Moreover, Fig. 5.2 show the pole mapping for the closed loop system considering 5 different actuation mechanisms: no tilt mechanism, 2 and 4 longitudinal tilting mechanisms ( $\alpha$ ) and 2 and 4 lateral tilting mechanisms ( $\beta$ ). It is important to note that the tilt mechanism is added to the system and works together with the spinning rotors. The poles closer to the origin are presented on Fig. 5.3.

It can be concluded, from Figs. 5.2 and 5.3, that all the closed-loop poles (eigenvalues) are on the left half plane of the Real/Imaginary axis assuming real negative values. Thus, the solution is a decaying exponential (oscillatory or not) so the system converges to a finite value, i.e. the system is considered as asymptotically stable.

Now, analyzing the poles positions it can be noted that some of them have shifted their position considering different actuation configurations, which is represented by the arrows on the



figures. Adding the tilting mechanism to the system brought the poles visible on Fig. 5.2 further from the imaginary axis compared to the open-loop poles, meaning that the pole natural frequency and/or the damping ratio has increased. Thus, the system is able to respond faster and/or more smoothly.

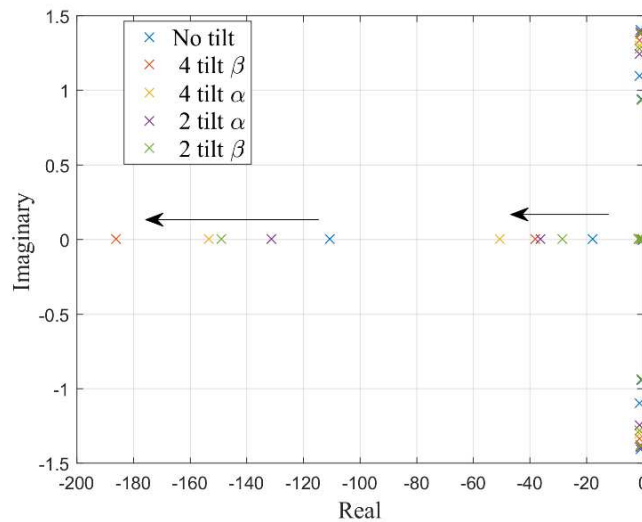


Figure 5.2 - Closed-loop poles for a first order integrator controller (step input signal) for five actuator configurations: no tilt, 4 lateral tilt, 2 lateral tilt, 4 longitudinal tilt and 2 longitudinal tilt.

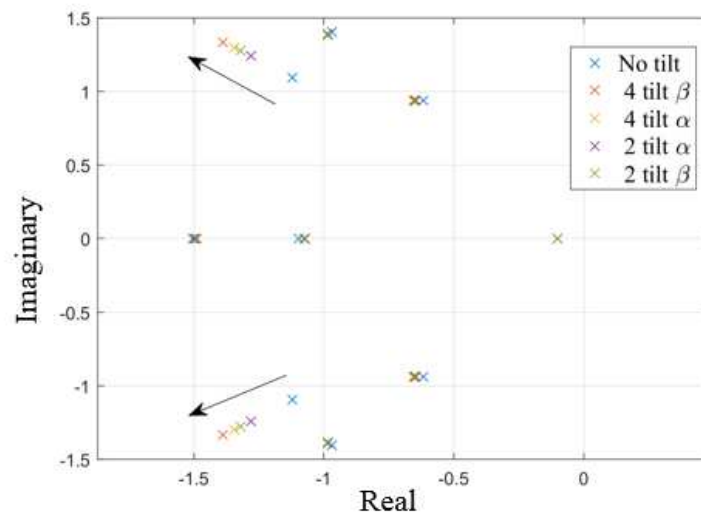


Figure 5.3 - Closed-loop poles close to origin for a first order integrator controller (step input signal) for five actuator configurations: no tilt, 4 lateral tilt, 2 lateral tilt, 4 longitudinal tilt and 2 longitudinal tilt.

Further, regarding Fig. 5.3, the poles tends to shift radially, meaning that the damping ratio is maintained while the natural frequency is increased, on this case the system will respond faster. This phenomenon is more effective when the lateral tilting mechanism is added the system and also when the number of tilting mechanisms is increased.

The zeros, or the numerator's roots of each transfer function of the closed-loop system, can also play a major role on its response. According to Hoagg and Bernstein (2007), having an open-right-plane zero, an input signal can be unbounded, a phenomenon known as *non-minimum-phase zero*, directly affecting the steady state system's response.

The zero mapping is presented on Figs. 5.4 and 5.5 for all system transfer functions five different scenarios as stated previously. One observes from the figures that the zero distribution does not follow a specific pattern. However, on Fig. 5.5, it can be seen that there are some zeros on the right half plane of the Real/Imaginary plane. This represent a *non-minimum-phase zero*, but their influence over the system shall be small since they are close to the Imaginary axis. This effect must be checked carefully via time response analysis.

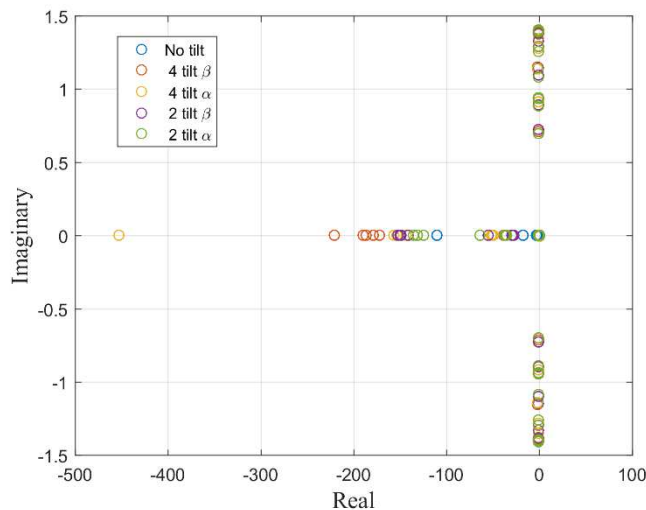


Figure 5.4 - Closed-loop zeros for a first order integrator controller (step input signal) for five actuator configurations: no tilt, 4 lateral tilt, 2 lateral tilt, 4 longitudinal tilt and 2 longitudinal tilt.

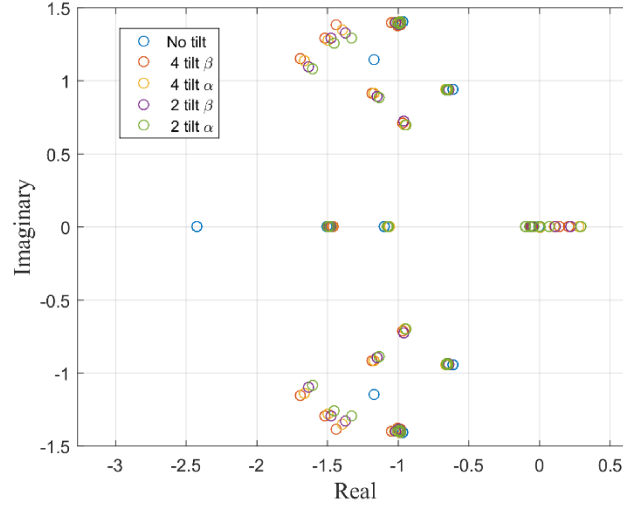


Figure 5.5 - Closed-loop zeros close to origin for a first order integrator controller (step input signal) for five actuator configurations: no tilt, 4 lateral tilt, 2 lateral tilt, 4 longitudinal tilt and 2 longitudinal tilt.

### 5.2.2 Time Response Analysis

Once the stability conditions of the system were checked, its time domain analysis can be performed in order to obtain more details about the system stability. Since the number of tilting mechanisms on the system affects only its response while the stability is maintained, only the 4-tilting cases will be available from now on omitting the analysis for 2-tilting configurations. But, as discussed earlier, the yaw angle was not included on the trajectory tracking control design for the cases of no tilt and tilting longitudinally; thus, a yaw attitude controller must be designed to guarantee stability. The reference input signal for the yaw controller will be considered as the direction to which the multi-copter is required to go.

Hence, a PID controller is designed based on the yaw angle transfer function for each rotor speed, which is given by:

$$\frac{\psi(s)}{\Omega_i(s)} = \text{sign}(\Omega_{0i}) \frac{0.0759}{s^2} \quad (5.2.11)$$

Then, the control law can be expressed as:

$$u(s) = K_p e(s) + K_d \dot{e}(s) + K_i \int e(s) \quad (5.2.12)$$

where  $K_p$ ,  $K_d$  and  $K_i$  are the PID controller constant gains. These are obtained using the *sisotool* Matlab® toolbox and the response shall be optimized in such manner that the yaw settling time is close to the other states controlled by the LQR controller.

Thus, a good step response was obtained adopting  $K_p = 1.283$ ,  $K_d = 9.296$  and  $K_i = 0.0435$ , which is illustrated on Fig. 5.6. The settling time is 12 seconds and it has 15% overshoot signal, approximately.

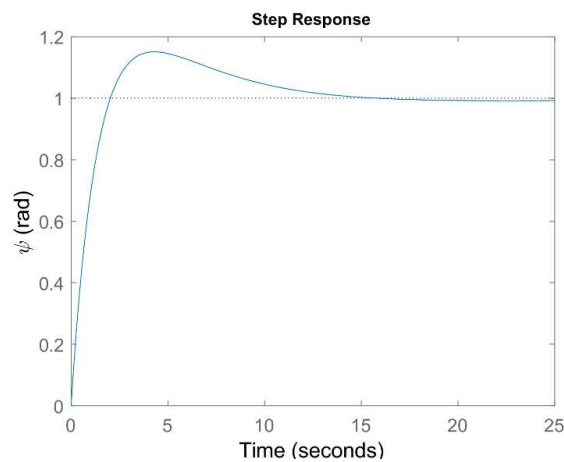


**Figure 5.6 - Closed-loop yaw step response due to rotor actuation with PID controller.**

Now, the first trajectory control attempt is to perform a position displacement on each *ICS* direction independently. The first attempt is to give a step input on the  $x_E$  direction so that the system response for 3 different tilting configurations are compared: no tilt, 4 longitudinal tilting mechanisms and 4 lateral tilting mechanisms. The states outputs are presented on Figs. 5.7 and 5.8.

From the figures, it can be observed on that all the  $x_E$  position converges to the desired value almost at the same time, and all the states converges to a value, meaning that they are stable. However, it interesting to note that the controller takes different actions for each case. Examining the Euler angles at Fig. 5.8, when there is no tilt mechanism, the aircraft only rotates about  $y_B$  axis (pitch rotation) while the other angles are kept close to zero (hovering level). On the other hand, for the two cases with the tilting mechanism the aircraft rotates about 3 directions ( $x_B$ ,  $y_B$  and  $z_B$ ) and the system equilibrium position is different from the hovering level ( $\phi = 0$  and  $\theta = 0$ ).

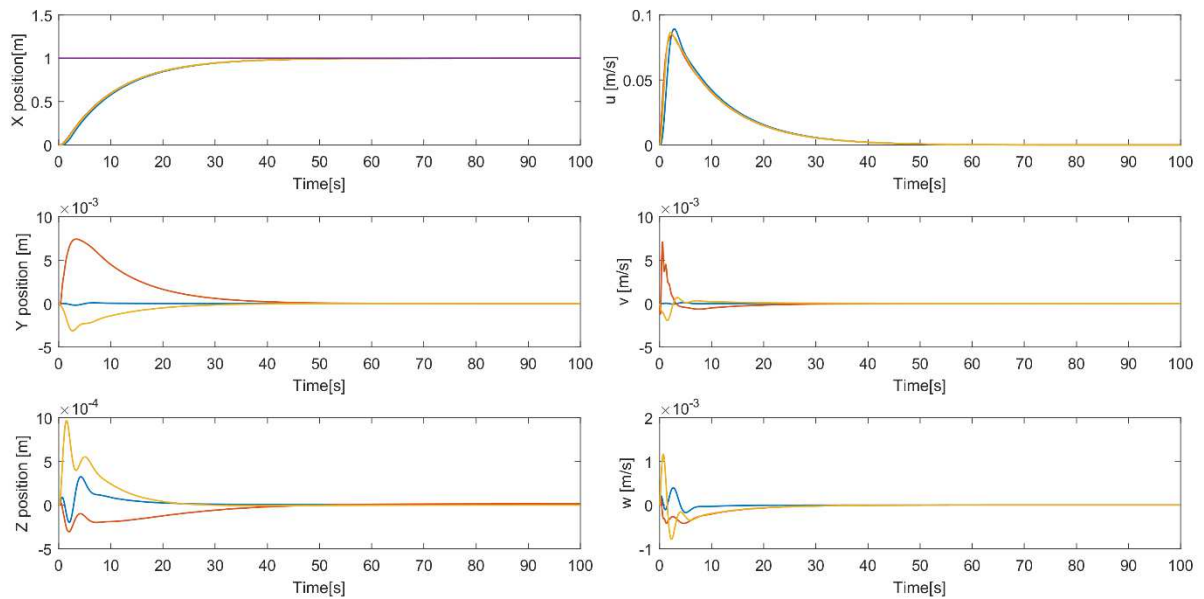


Figure 5.7- Multi-copter position (left) and velocity (right) for a unit step (purple) on the x direction for 3 different configurations: no tilt (blue), 4 longitudinal tilting mechanisms (red) and 4 lateral tilting mechanisms (yellow).

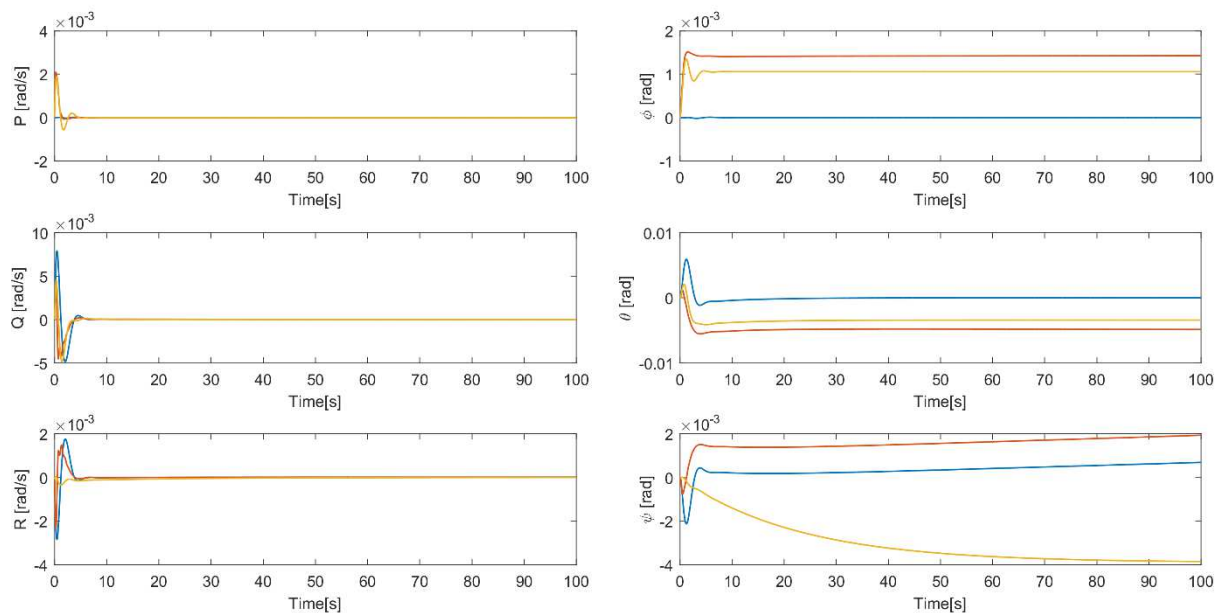
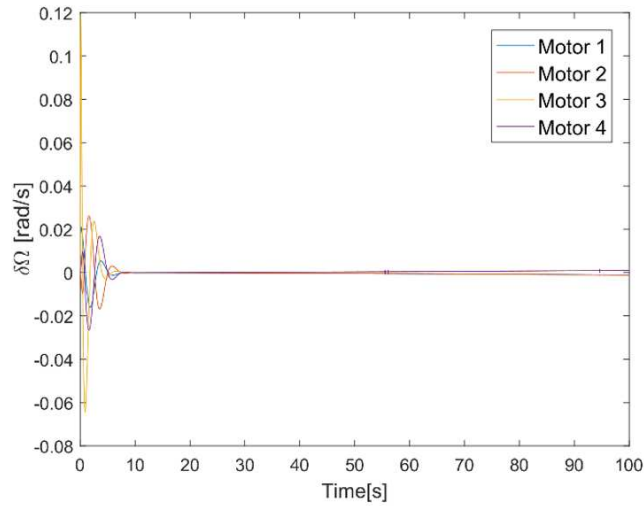


Figure 5.8 - Multi-copter angular velocity (left) and Euler angles (right) for a unit step on the x direction for 3 different configurations: no tilt (blue), 4 longitudinal tilting mechanisms (red) and 4 lateral tilting mechanisms (yellow).

Furthermore, regarding the input signal from the controller to the spinning rotors and the tilt mechanism, Figs. 5.9, 5.10 and 5.11 show that the  $\delta\Omega$  variation is larger when the system has no tilt mechanism. However, for lateral tilt mechanism, the value reached at the steady state condition is not that found at trimmed hovering rotor angular speed ( $\delta\Omega = 0$ ). Also, the tilt angle equilibrium position is not at the central position ( $\delta\alpha = 0$  and  $\delta\beta = 0$ ) for both tilting cases. Consequently, the system is able to find an equilibrium condition different from the hover flight, which is evidenced by the Euler angular equilibrium positions obtained in Fig. 5.8. This fact can be evaluated by verifying the multiples equilibrium positions of the nonlinear dynamics imposed by the tilt-mechanisms.

In conclusion, even that the multi-copter is able to reach the desired position, it may assume a different equilibrium position at the steady-state regime and it may have higher input signals to keep the stability at that position.



**Figure 5.9 - Rotor angular speed variation when the multi-rotor has no tilting mechanism for a unit step on x direction.**

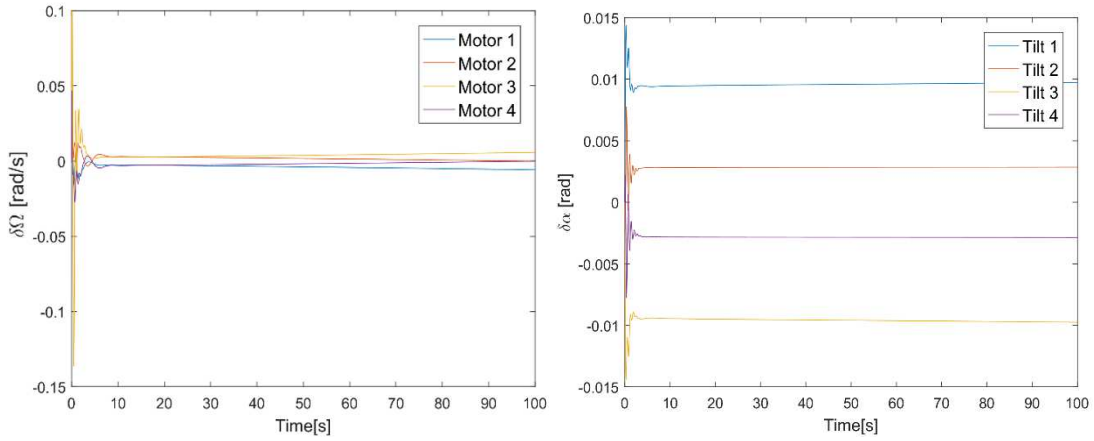


Figure 5.10 - Rotor angular speed (left) variation and tilt angle (right) when the multi-rotor has longitudinal tilting mechanism for a unit step on x direction.

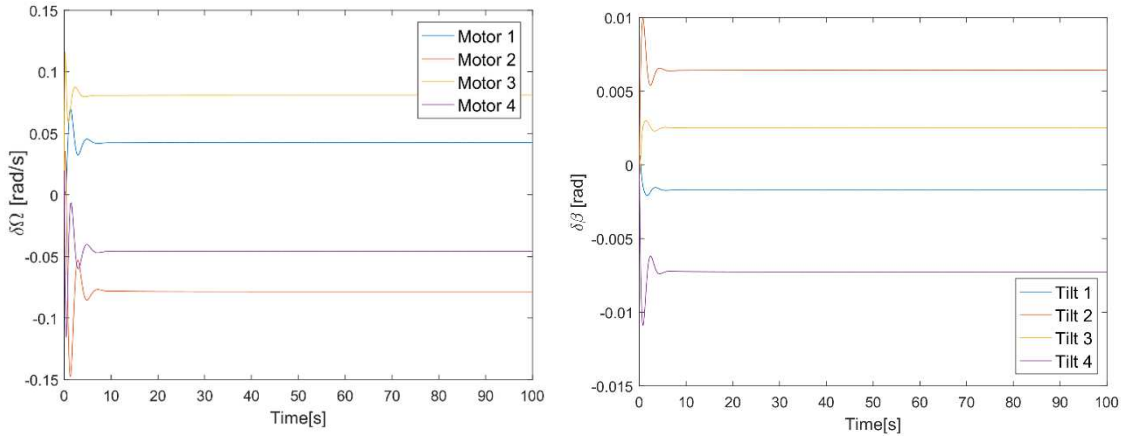
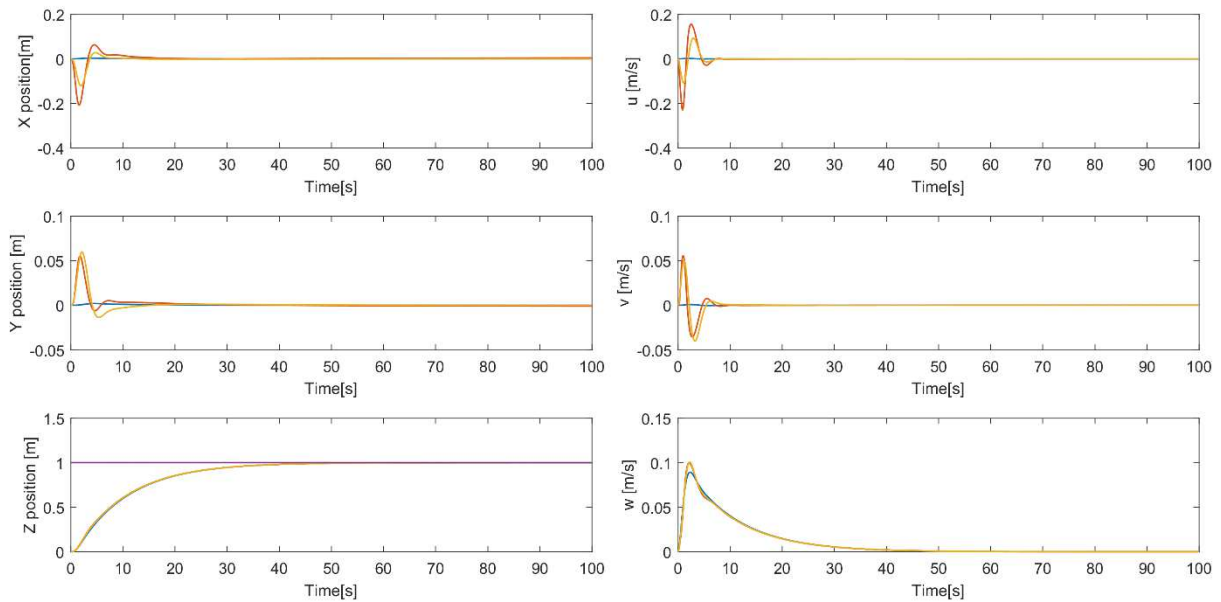


Figure 5.11- Rotor angular speed (left) variation and tilt angle (right) when the multi-rotor has lateral tilting mechanism for a unit step on x direction.

The aircraft displacement on the  $y_E$  direction is expected to be the same as the  $x_E$  considering the quad-rotor symmetry. Nevertheless, it must be noted that, since the controller is designed considering a linear model, if the yaw input is set as 90 deg, i.e. desiring that  $x_B$  axis align with the  $y_E$  direction, the yaw angle will be out of the linearity condition and the system response will become unstable. Hence, to avoid this problem it is interesting to align the aircraft with the trajectory direction as an initial condition, so that the small perturbation theory is valid.

Further, the next reference signal is a step input in the  $z_E$  direction, or an ascending position. The state responses for the three considered configurations are presented on Figs. 5.12 and 5.13.

Again, analyzing the states on Figs. 5.12 and 5.13 it can be concluded that the multi-rotor displaces on all 3 directions when equipped with both tilting mechanisms, even that, practically speaking, it would not be necessary. However, the settling time on  $z_E$  direction is the same for the three cases. One important thing to note is that the even with the separated controller, the yaw angle increases with time for the longitudinal (4 tilt  $\alpha$ ) case even though the system is dynamically stable (all forces and moments are zero). This problem is caused by the zeros at the right half plane of the Real/Imaginary plane known as *non-minimum phase*, which is also confirmed observing the longitudinal tilt actuation on Fig. 5.15. On this case, as the yaw angle increases, even at a small rate, as illustrated on Fig. 5.13 (right), so the control input continues increasing even that the equilibrium position has already been reached (zero steady state error and constant angular speed  $R$ ). The effect is not observed when the multi-copter has none or a lateral tilt mechanism.



**Figure 5.12-** Multi-copter position (left) and velocity (right) for a unit step (purple) on the  $z$  direction for 3 different configurations: no tilt (blue), 4 longitudinal tilting mechanisms (red) and 4 lateral tilting mechanisms (yellow).



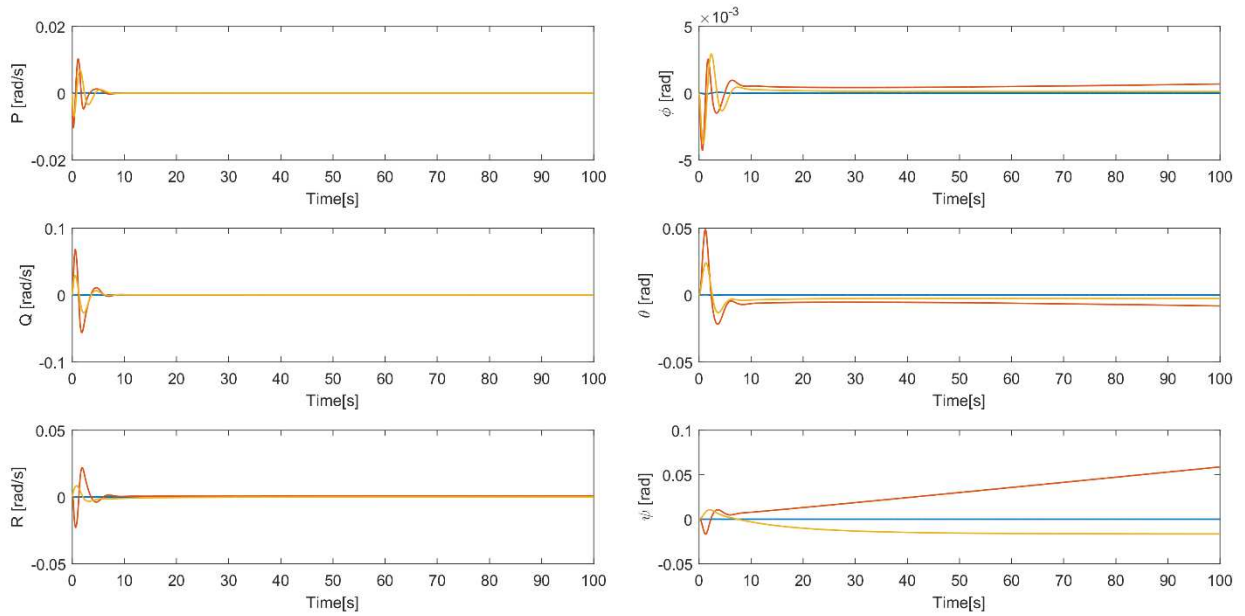


**Figure 5.13 - Multi-copter angular velocity (left) and Euler angles (right) for a unit step on the z direction for 3 different configurations: no tilt (blue), 4 longitudinal tilting mechanisms (red) and 4 lateral tilting mechanisms (yellow).**

Looking the control effort for the system without tilt, it can be concluded that the angular speed inputs are the same on absolute value for motors 1 and 3 and also for 2 and 4. On this manner, the system is capable to maintain the equilibrium and hold the produced torques as zero. This fact is not so evident when the system has lateral tilting mechanism (Fig. 5.16 left). On this case, the control compensates the disequilibrium varying the tilt mechanism angle.

Evaluating the control effort for all three scenarios on Figs. 5.14, 5.15 and 5.16, it is evident that the angular speed inputs were lower when the system had no tilt mechanism. Hence, the tilt mechanism is irrelevant when performing an ascendant trajectory since the propeller thrust variation is much more effective.

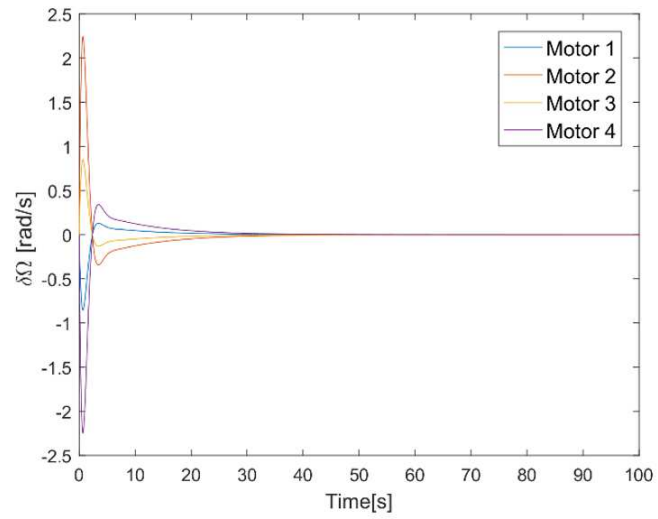


Figure 5.14 - Rotor angular speed variation when the multi-rotor has no tilting mechanism for a unit step on z direction.

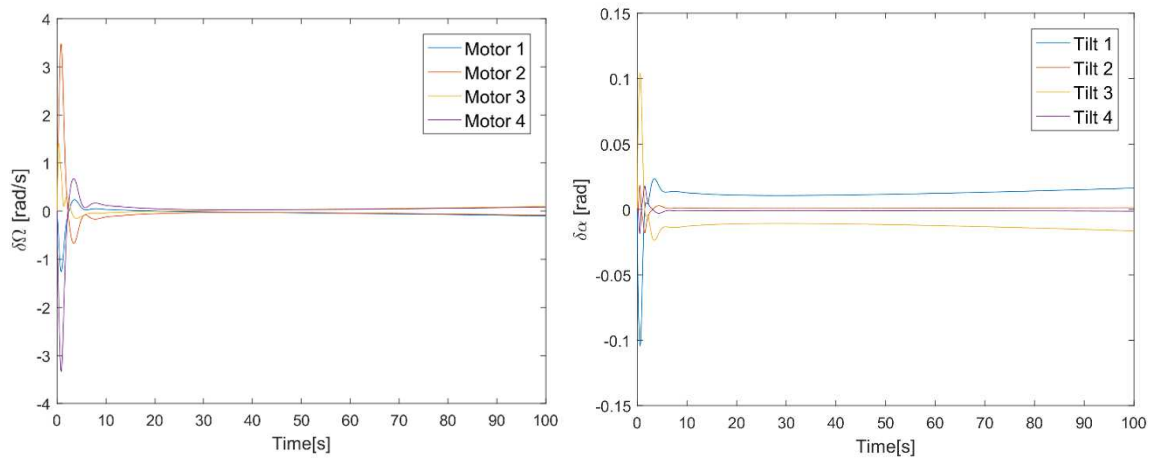
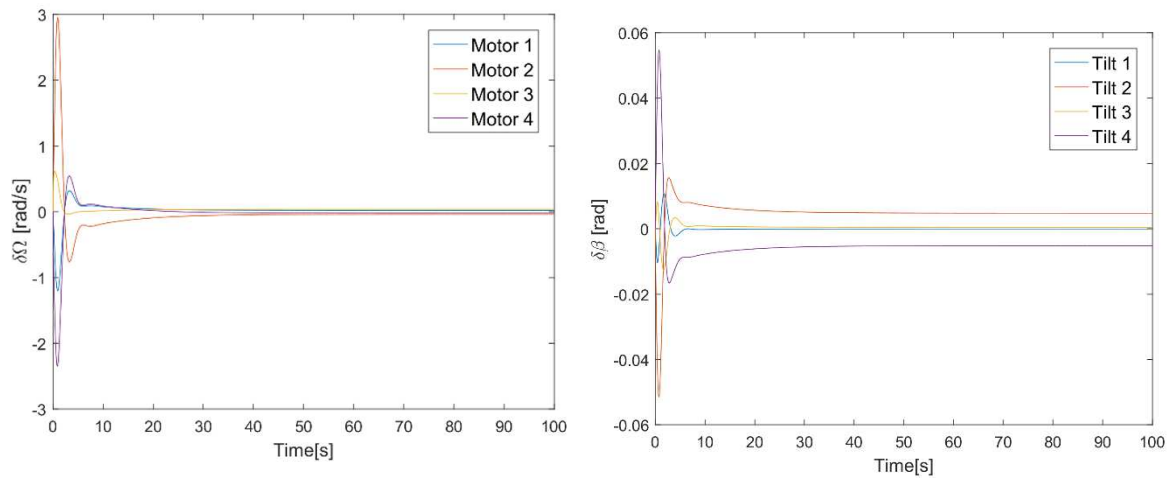


Figure 5.15 - Rotor angular speed (left) variation and tilt angle (right) when the multi-rotor has longitudinal tilting mechanism for a unit step on z direction.



**Figure 5.16 - Rotor angular speed (left) variation and tilt angle (right) when the multi-rotor has lateral tilting mechanism for a unit step on z direction.**

Once the multi-rotor displacement on each inertial direction was investigated, the system behavior will be tested for a unitary step on all three directions simultaneously. The position and Euler angles responses are illustrated on Fig. 5.17 and 5.18, respectively and also the linear and angular velocities. Higher oscillations on the y-direction response when the system is not equipped with tilt mechanism.

The figures show that the velocities converge to zero as soon as the position goes to the reference value. Once again is noted that the final angular positions are different from zero when the quadcopter is equipped with the tilting mechanism. It is also important to remark that, for the 4-longitudinal tilt case, even that the initial yaw angle is 45 deg, the angle converges to zero where it stays at equilibrium as presented on Fig. 5.18. Finally, on Fig. 5.17, it is observed that the system equipped with the tilting mechanism had lower oscillations on velocity principally on  $y_E$  direction.

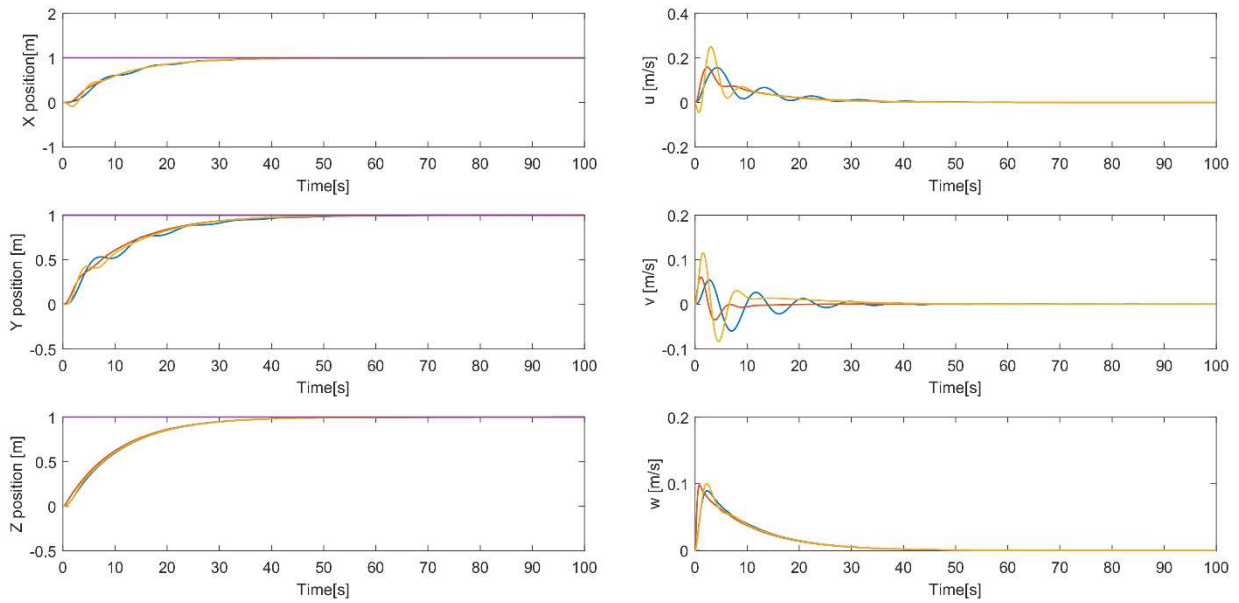


**Figure 5.17 - Multi-copter position (left) and velocity (right) for a unit step (purple) on the on all three directions x, y, and z for 3 different configurations: no tilt (blue), 4 longitudinal tilting mechanisms (red) and 4 lateral tilting mechanisms (yellow).**

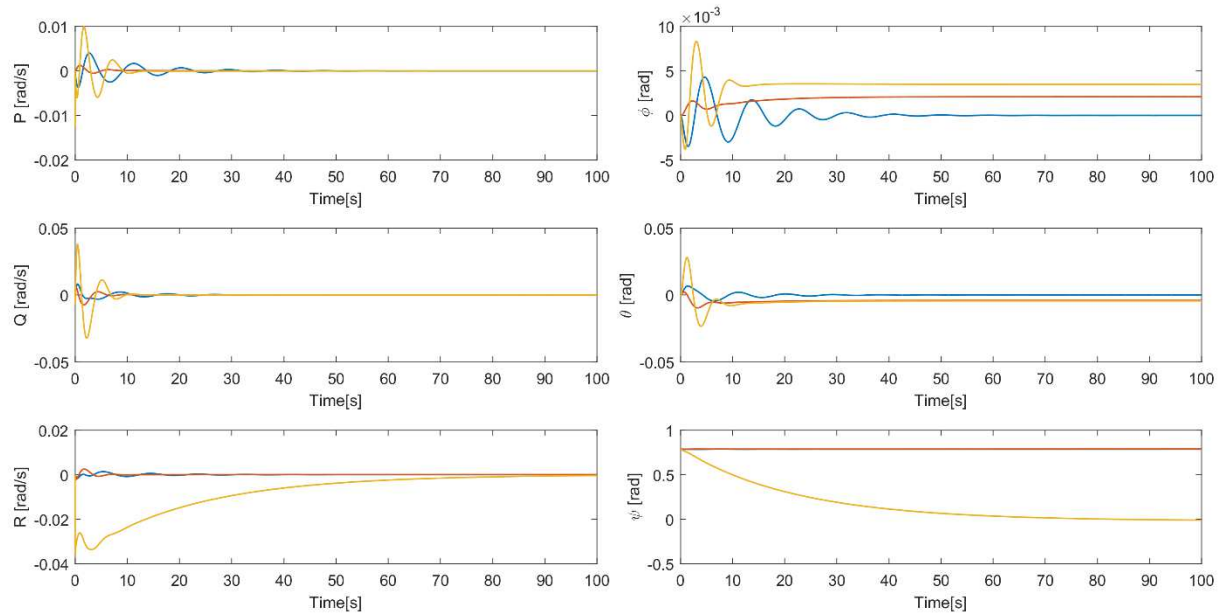


**Figure 5.18 - Multi-copter angular velocity (left) and Euler angles (right) for a unit step on all three directions (x, y, and z) for 3 different configurations: no tilt (blue), 4 longitudinal tilting mechanisms (red) and 4 lateral tilting mechanisms (yellow).**

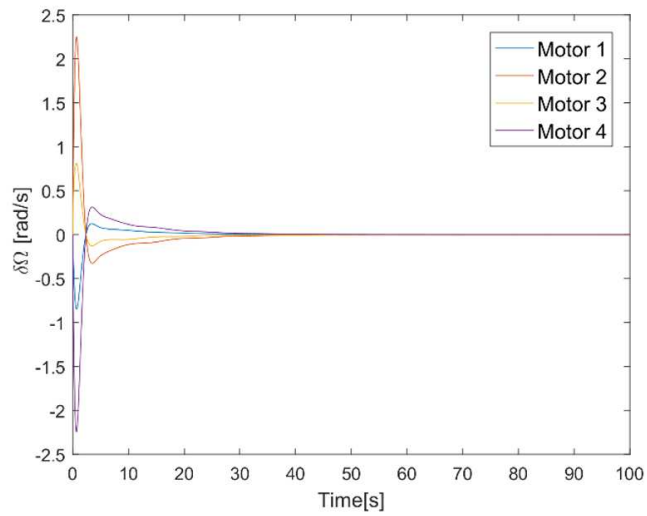


Figure 5.19 - Rotor angular speed variation when the multi-rotor has no tilting mechanism for a unit step on x, y and z directions.

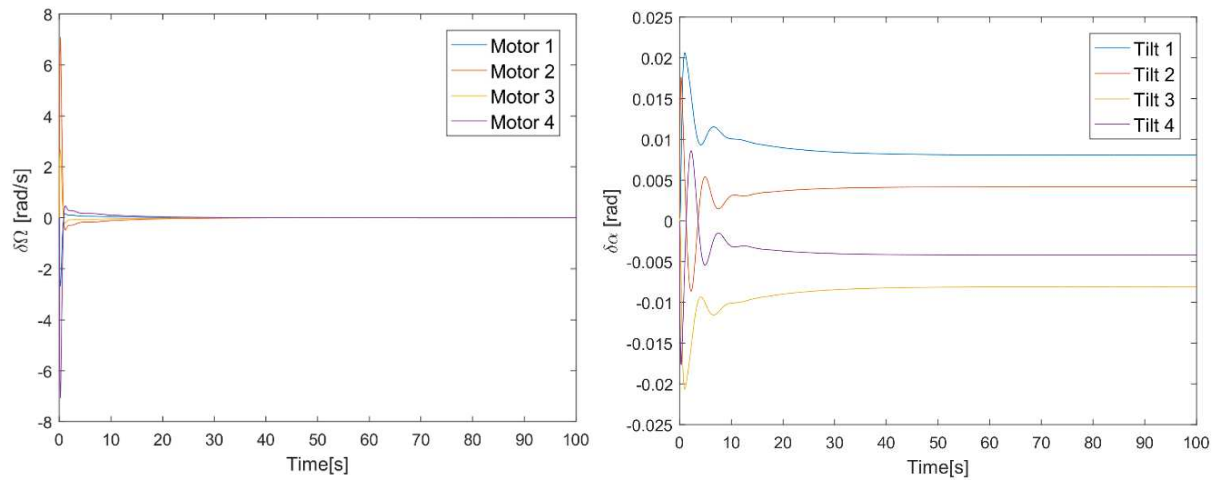
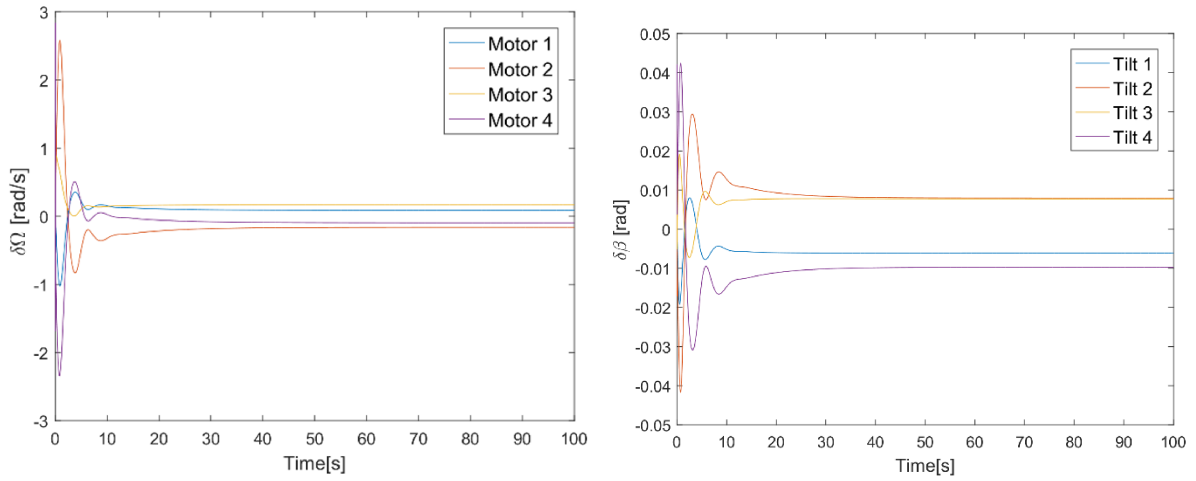


Figure 5.20 - Rotor angular speed (left) variation and tilt angle (right) when the multi-rotor has longitudinal tilting mechanism for a unit step on x, y and z directions



**Figure 5.21 - Rotor angular speed (left) variation and tilt angle (right) when the multi-rotor has lateral tilting mechanism for a unit step on x, y and z directions.**

Lastly, regarding the control effort input on Figs. 5.19, 5.20 and 5.21, it can be concluded that the multi-copter with the tilt mechanism has higher input signals compared to the aircraft without the mechanism. Also, the tilt angle input signals are very small for both tilting mechanisms, showing that the movement is highly dependent from the rotor angular speed. Obviously, the multi-copter response can vary for each choice of weighting matrices; but, if the tilt input gains are too large, the system becomes very susceptible to non-linear effects, principally the gyroscopes. Further, from experiences through simulations, the lateral tilt has proved to be much more susceptible to higher amplitudes than the longitudinal one. This behavior is related to the capacity to control the yaw angle more efficiently.

### 5.3 Ramp Input Signal

After evaluating the system response for a step input, the next step is to exam it for a remap trajectory reference signal. From Table 3.1, the ramp reference input has the differential equation represented by  $\ddot{r} = 0$  with the model parameters  $p = 2$  and  $a_1 = a_2 = 0$ . Similarly, to the step input, the expanded space state matrices  $\tilde{A}$  and  $\tilde{B}$  can be written as presented on Eq. (3.3.8) and (3.3.9). Now, the desired controller will be a second order integrator such that the steady state error for a second order derivative reference signal is zero when  $t \rightarrow \infty$ .

### 5.3.1 Choice of Weighting Matrices

To design a controller for a second order derivative reference signal, the choice of the weighting matrices shall be different from the matrices presented on Eqs. (5.2.4), (5.2.6) and (5.2.7). Again, based on trial and error experience, the weighting matrices for the ramp reference signal will be:

$$Q_k = \text{diag}[0.5 \quad 0.5 \quad 10 \quad 5 \quad 5 \quad 10 \quad 0.1 \quad 0.1 \quad 0.2 \quad 250 \quad 25 \quad 5000 \quad 500 \quad 0.5 \quad 0.5 \quad 10] \quad (5.3.1)$$

$$\rho_k = [0.005 \quad 0.002 \quad 0.0008 \quad 0.0002] \quad (5.3.2)$$

$$\sigma_k = [500 \quad 500 \quad 500 \quad 500] \quad (5.3.3)$$

Comparing with the step weighting values from Eqs. (5.2.4), (5.2.6) and (5.2.7), more 3 lines and columns were added to the  $Q_k$  matrix which represents the error second derivative terms. Also, comparing the weighting values considered with respect to the step input case, it is noted that the weighting values for the motors were decreased allowing higher values of angular input and the tilting values were increased to reduce the instabilities due high tilting angles.

Again, the stability of the system must be checked before making time response analysis. Since the stability variation were already checked for the number of tilting mechanisms, for now on, only three cases will be studied: no tilt, 4 longitudinal tilt, and 4 lateral tilt.

### 5.3.2 Poles and Zeros Analyses

On this case, likewise the analysis performed to the first order derivative controller (step input signal), the pole and zeros mapping has the objective to compare the system stability for the different actuation configuration and seek possible stability problems as the *non-minimum-phase zeros*.

Figure 5.22 illustrates the pole mapping for the three mentioned cases. From the figures, once again it can be observed that the controller was able to place all poles on the left half of the Real/Imaginary plane, guaranteeing global stability. Once again, the lateral tilting mechanism has shifted the poles slightly to the left and, as discussed before, the system is able to respond faster.

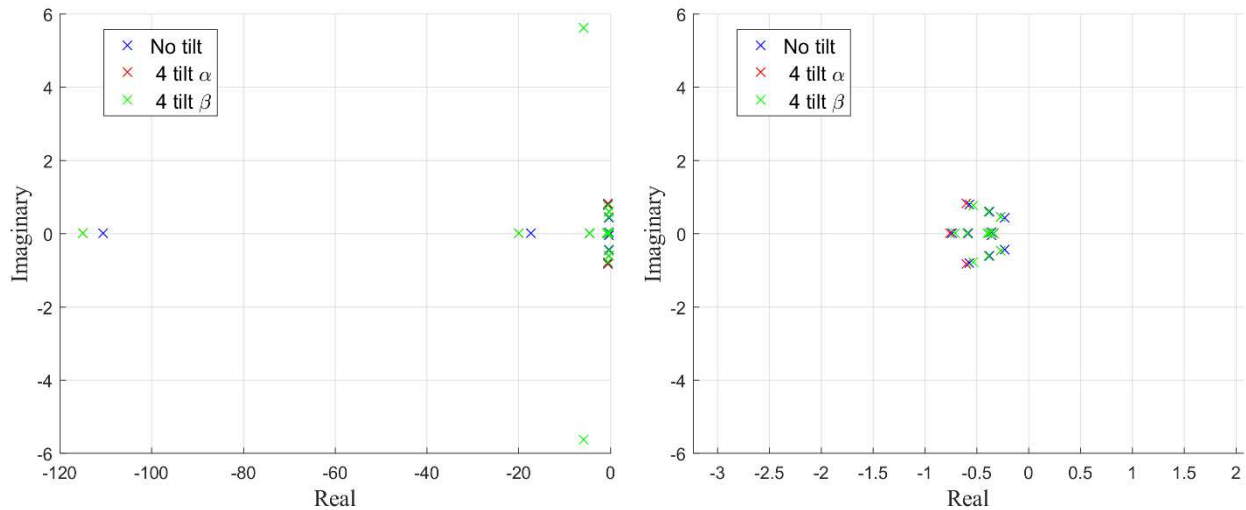


Figure 5.22 - (Left) closed-loop poles for a second order integrator controller (ramp input signal), (Right) poles close to origin, for three actuator configurations: no tilt, 4 lateral tilt and 4 longitudinal tilt.

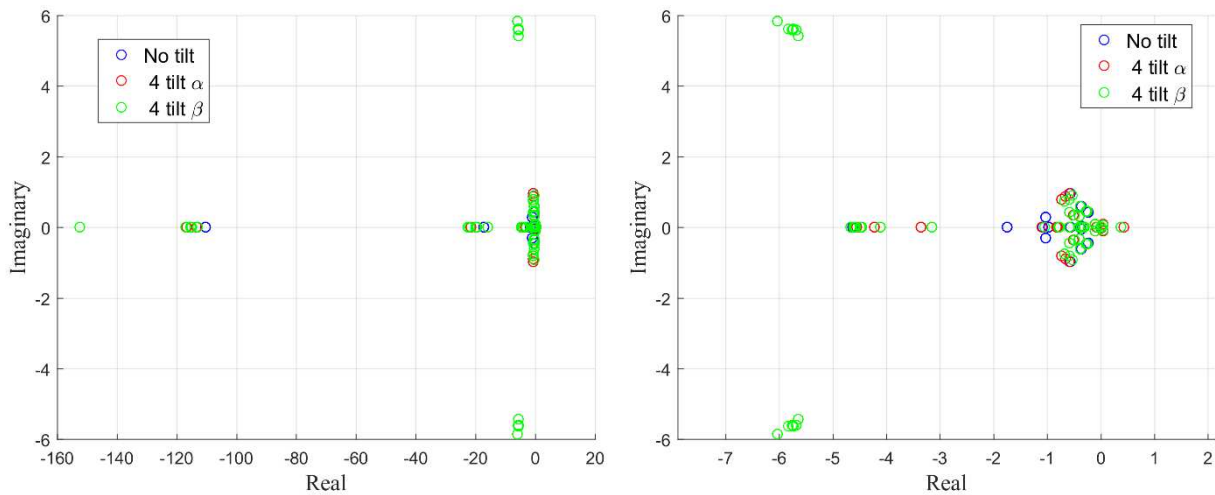


Figure 5.23 - (Left) closed-loop zeros for a second order integrator controller (ramp input signal), (Right) zeros close to origin, for three actuator configurations: no tilt, 4 lateral tilt and 4 longitudinal tilt.

Now, regarding the closed-loop system zeros location on Fig. 5.23, it can be perceived that there are some zeros on the right half of the Real/Imaginary plane. Looking more closely, it can be noted that these zeros are from the systems with the tilting mechanism. Concluding, the system is susceptible to *non-minimum phase* effects and can become unstable on steady state.



### 5.3.3 Time Response Analysis

As soon as the multi-copter's sensibility response for the three-spatial direction has already been tested for a step response, it would be redundant to verify it for other signals since the same discrepancies were presented such as: tilt actuation when performing an ascending flight and less oscillations on x and y directions.

Then, the system behavior will be investigated setting a unit ramp reference command to all three directions simultaneously representing a 3D ramp with 45 deg angle w.r.t. the ground ( $x_E$  -  $y_E$  plane). Once again, the response is studied considering the three different tilting mechanisms as present on Figs 5.24 and 5.25.

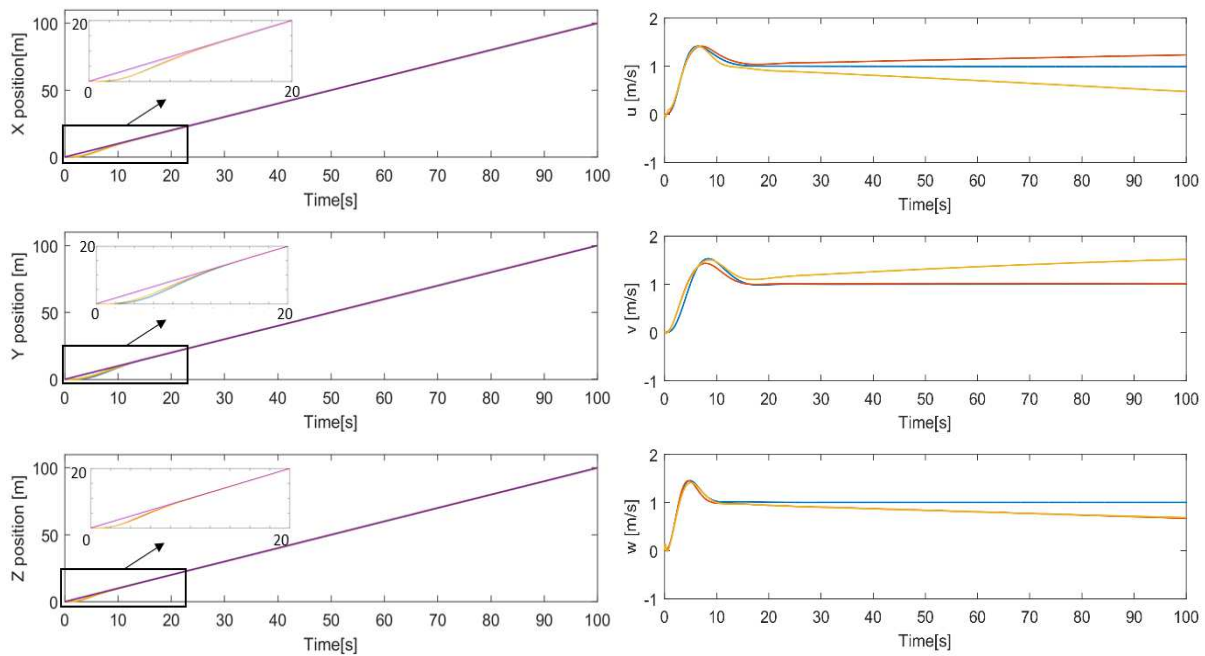


**Figure 5.24 - Multi-copter position (left) and velocity (right) for a unit ramp input signal on the on x, y and z directions (purple) for 3 different configurations: no tilt (blue), 4 longitudinal tilting mechanisms (red) and 4 lateral tilting mechanisms (yellow).**

From Fig 5.24, it can be observed that the system is capable to follow the desired trajectory successfully during the simulation interval. The three directions displacements converge to the reference input signal almost simultaneously (15 seconds). Also, the multi-copter response when

having the tilt mechanism is slightly faster for  $y_E$  and  $z_E$  directions. However, looking at the multi-copter linear velocity (Fig. 5.24 right) and Euler angles (Fig. 5.25 right) it is verified that the signals do not converge to a finite value for the cases where the aircraft is equipped with the tilting mechanism.

This is a classic example of the *non-minimum phase* effect on the system steady state response. Even that the system reaches the reference condition, its input signal continues rising along with the reference input signal, as can be seen on Figs. 5.27 and 5.28. Therefore, the system tends to become unstable as  $t \rightarrow \infty$ . In conclusion, the tilt-mechanism may be used very carefully on unbounded reference signals such as the ramp input since it is a *non-minimum phase* system.

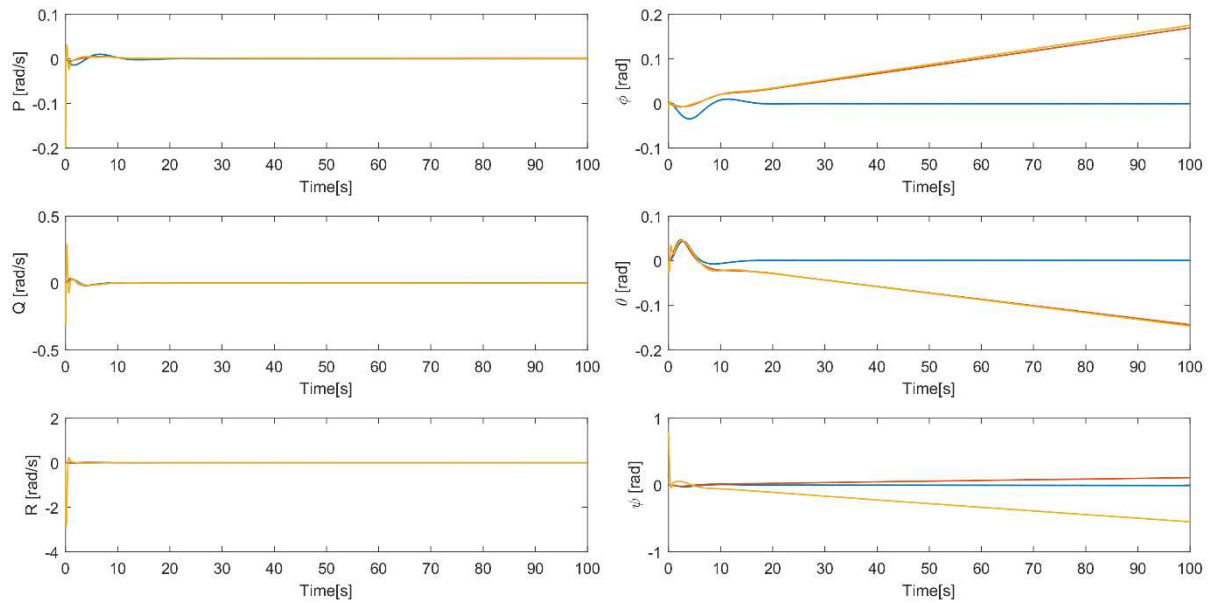


**Figure 5.25 - Multi-copter position (left) and velocity (right) for a unit ramp input signal on the on all three directions (x, y, and z) for 3 different configurations: no tilt (blue), 4 longitudinal tilting mechanisms (orange) and 4 lateral tilting mechanisms (yellow).**

Further, analyzing Fig. 5.26, it is perceived that the *non-minimum phase* effect is visible when the system is not equipped with the tilting mechanism. Also, again the control effort was lower for the system without the tilting mechanism comparing the rotor angular speed input signals amplitudes on Figs. 5.26, 5.27 (left) and 5.28 (left).

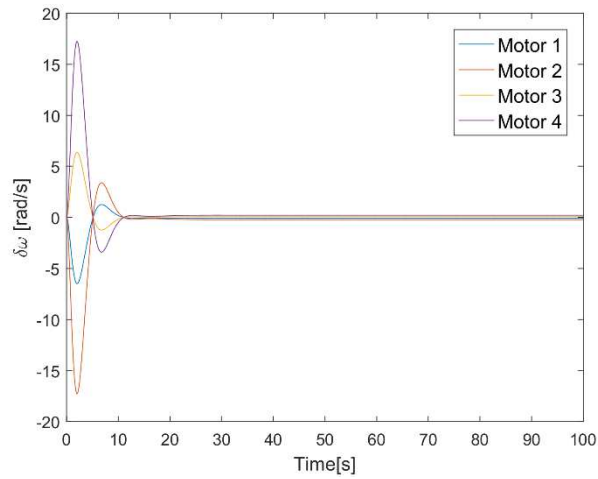


Figure 5.26 - Rotor angular speed variation when the multi-rotor has no tilting mechanism for a unit ramp inputs on x, y and z directions.

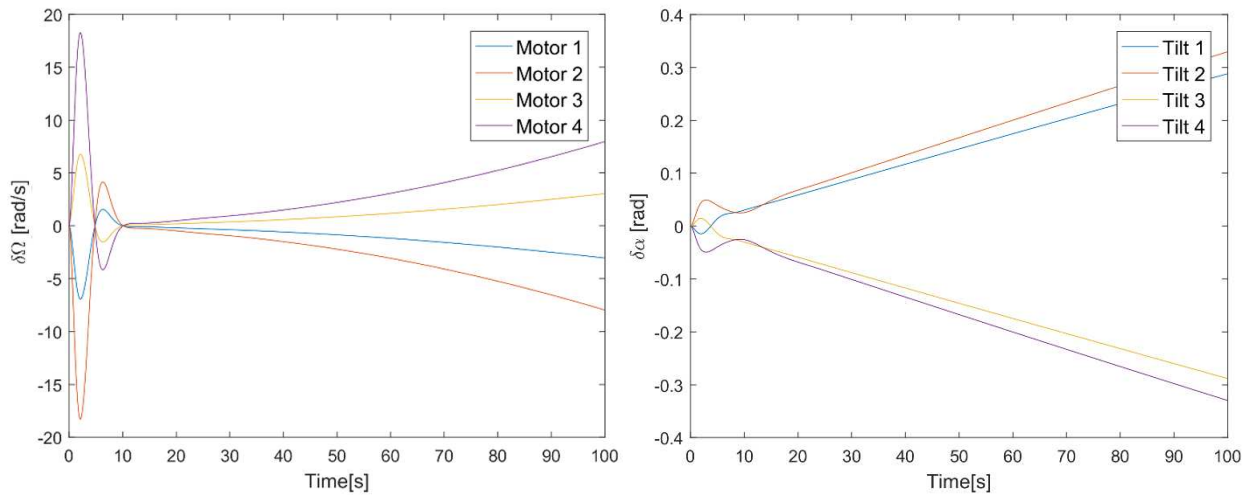


Figure 5.27 - Rotor angular speed (left) variation and tilt angle (right) when the multi-rotor has longitudinal tilting mechanism for a unit ramp inputs on x, y and z directions.

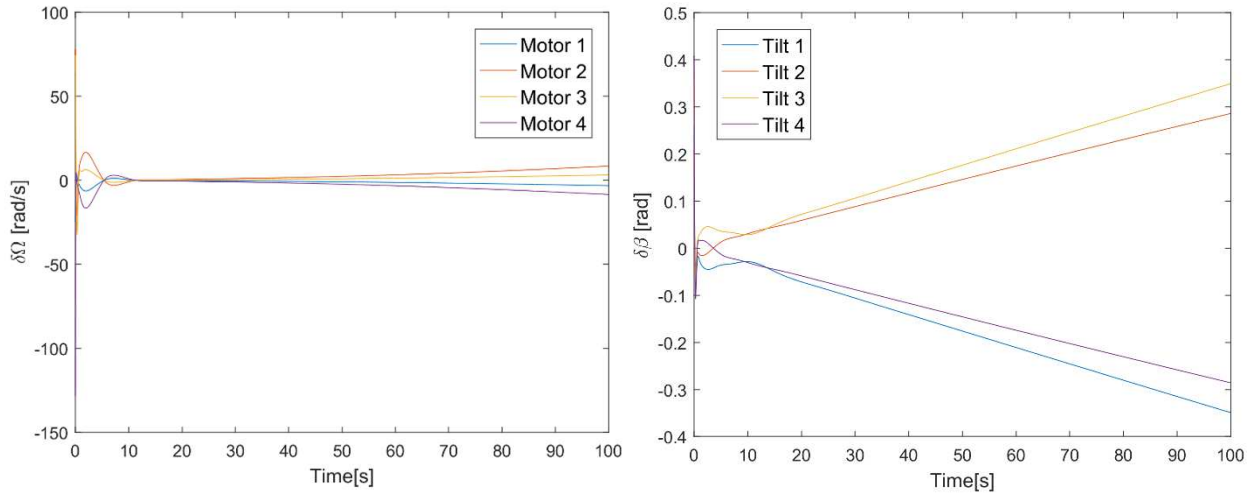


Figure 5.28 - Rotor angular speed (left) variation and tilt angle (right) when the multi-rotor has lateral tilting mechanism for a unit ramp inputs on x, y and z directions.

## 5.4 Sinusoidal Input Signal

The third type of input reference signal to be tested is the sinusoidal or harmonic functions. As stated on Chapter 3, the harmonic signal is also a second order time derivative signal as presented on Table 3.1. The difference from the sinusoidal controller to the ramp input controller is that the term  $a_1 = -\omega_0^2$  is added to the expanded matrix (Eq. (3.3.8)) also in the control loop multiplying the tracking variables output signal in order to correct the phase lag of the system. Thus, on this case, the weighting matrices will be maintained from the previously simulation.

### 5.4.1 Poles and Zeros Analysis

Once more, a brief stability analysis is made mapping the poles and zeros position on the Real/Imaginary plane presented on Figs. 5.29 and 5.30.

Comparing Figs. 5.22, 5.23, 5.29 and 5.30 it is explicit that even the weighing matrices being the same from the ramp input, the poles and zeros positions shift their position. For instance, basically all poles and zeros come closer to the origin and, one of the poles belonging to the 4-longitudinal tilt, goes farer to the origin on the real positive direction. This could be a problem considering the *non-minimum phase* effect discussed before.

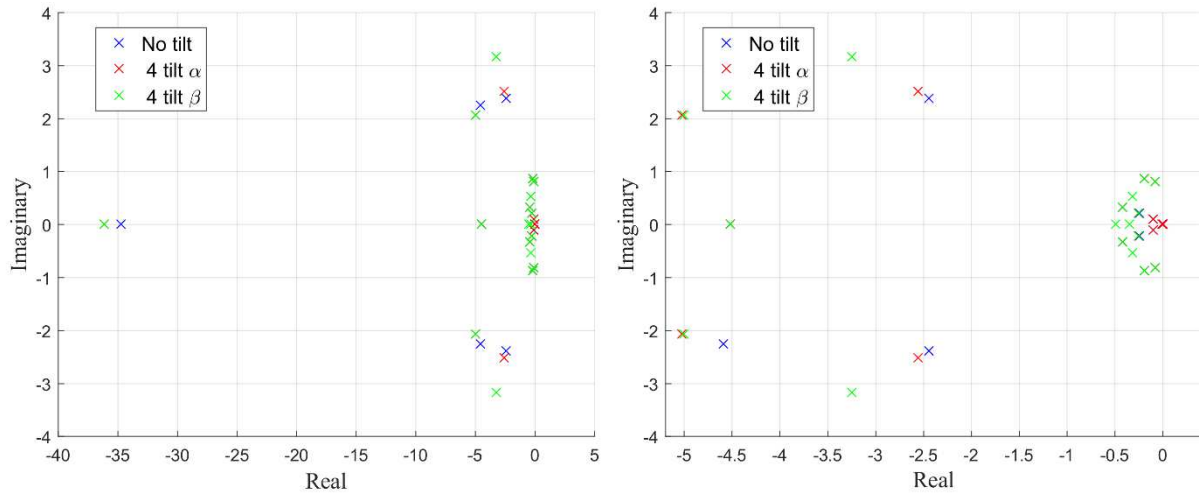


Figure 5.29 - (Left) closed-loop poles for a second order integrator controller (sinusoidal input signal), (Right) poles close to origin, for three actuator configurations: no tilt, 4 lateral tilt and 4 longitudinal tilt.

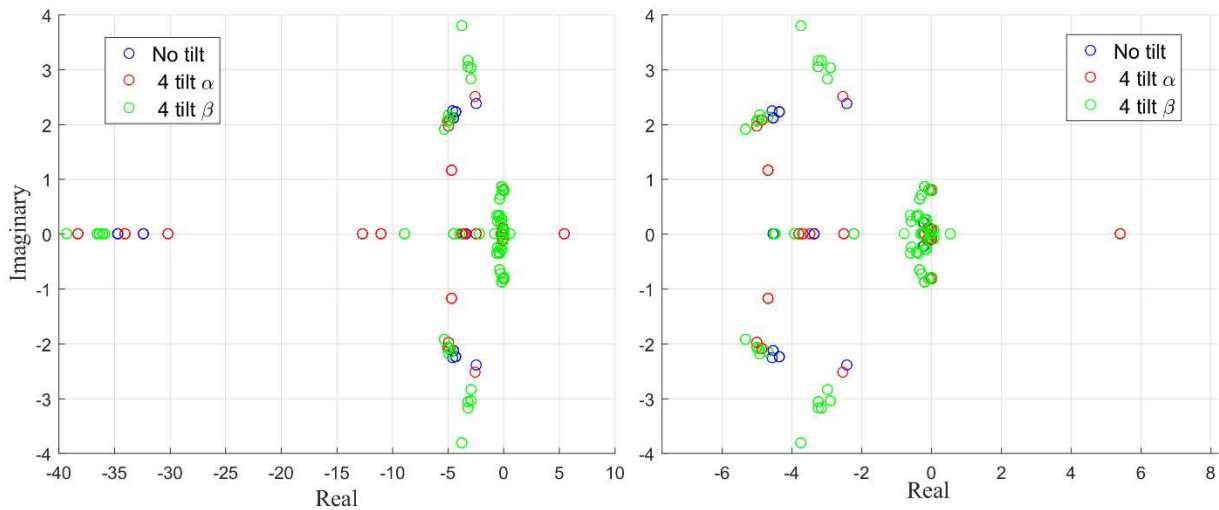


Figure 5.30 - (Left) closed-loop zeros for a second order integrator controller (sinusoidal input signal), (Right) zeros close to origin, for three actuator configurations: no tilt, 4 lateral tilt and 4 longitudinal tilt.

## 5.4.2 Time Domain Analysis

Unlike the other two previous analysis, on this case, it may be interesting to evaluate the system response for a sinusoidal reference input independently on each *ICS* direction since giving an input on all directions simultaneously is practically unfeasible. On this manner, the sinusoidal

input signal equation chosen for the simulations has amplitude and frequency,  $A_0 = 1 \text{ m}$   $\omega_0 = 0.796 \text{ rad/s}$ , respectively, and can be written on the time domain as:

$$r(t) = A_0 \sin(\omega_0 t + \varepsilon_0) \quad (5.4.1)$$

being  $\varepsilon_0$  the phase of the signal. Starting the analysis on the  $x_E$  direction,  $\varepsilon_0$  is set as 90 deg so that the generated signal represents a cosine signal. The initial yaw angle is set as 45 deg or  $\pi/4$  rad in order to evaluate the capacity of the controller to bring system to stability. Finally, the system state responses are presented on Figs. 5.31 and 5.32

Firstly, from Fig. 5.31 it can be verified that all the three cases (no tilt, 4-longitudinal tilt and 4-lateral tilt) the system can follow the harmonic input signal. On the  $y_E$  direction, the oscillations are much higher when the system has none or 4-longitudinal tilting mechanisms. However, the oscillations on  $z_E$  direction was higher when the 4-lateral tilting mechanism is equipped. Further, observing Fig. 5.32 (right), it can be noted that the pitch angle has also higher oscillations for none or 4-longitudinal tilting mechanisms cases. This could be cause of instability to the system for higher amplitude signals. Finally, from Fig. 5.32 (right), it is observed that the controller brings the yaw angle to zero position when the multi-copter has lateral tilting mechanism, while it remains around the initial value (45 deg or  $\pi/4$  rad) for the none or longitudinal cases.

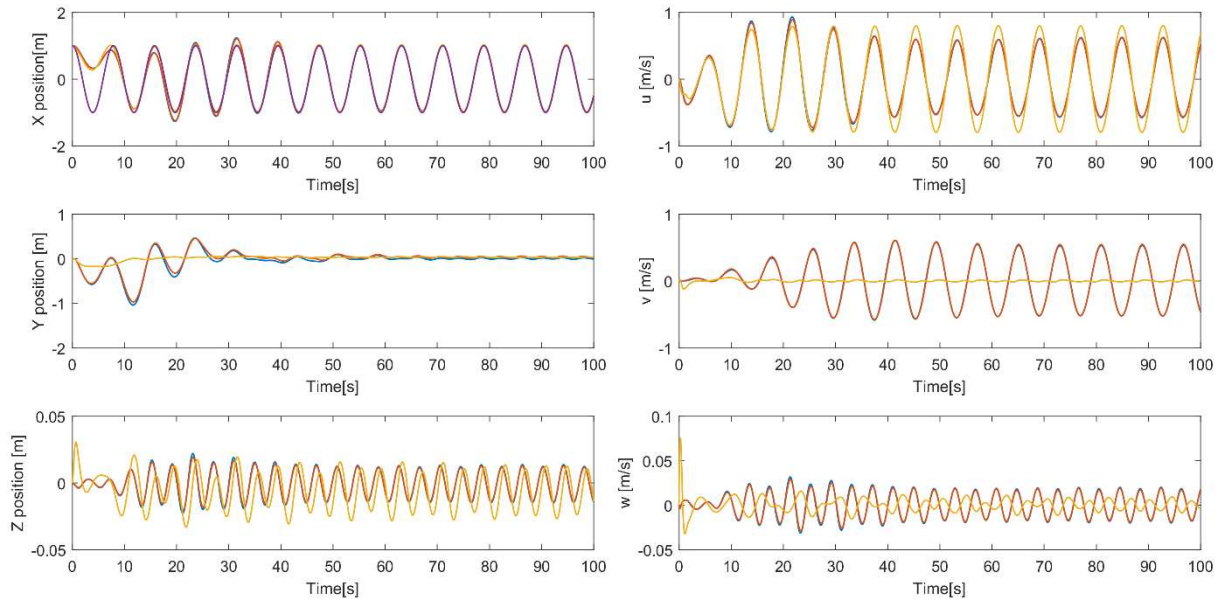


**Figure 5.31 - Multi-copter position (left) and velocity (right) for a sinusoidal input signal (purple) on the x direction for 3 different configurations: no tilt (blue), 4 longitudinal tilting mechanisms (red) and 4 lateral tilting mechanisms (yellow).**

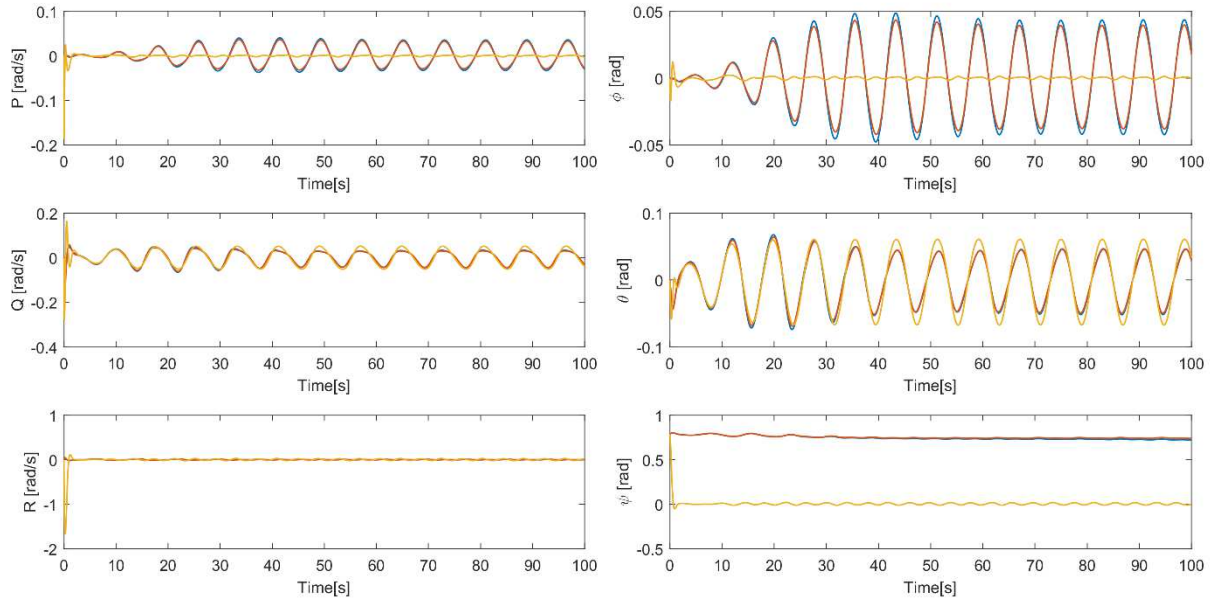


**Figure 5.32 - Multi-copter angular velocity (left) and position (right) for a sinusoidal input signal (purple) on the x direction for 3 different configurations: no tilt (blue), 4 longitudinal tilting mechanisms (red) and 4 lateral tilting mechanisms (yellow).**

Regarding the input signals on Figs. 5.33, 5.34 and 5.35 the rotor angular speed input signals are quite the same for all three cases and that the tilting angles assume small values. This fact can be explained by the high weighting values on  $\sigma_k$ . It must be stated that, trying higher weighting values, the system is very susceptible to gyroscopic effects and tends to destabilize. Further, the peak values at the beginning are explained by the fact that the system departs from the origin ( $x_E = 0$ ), while the reference signal starts at 1.



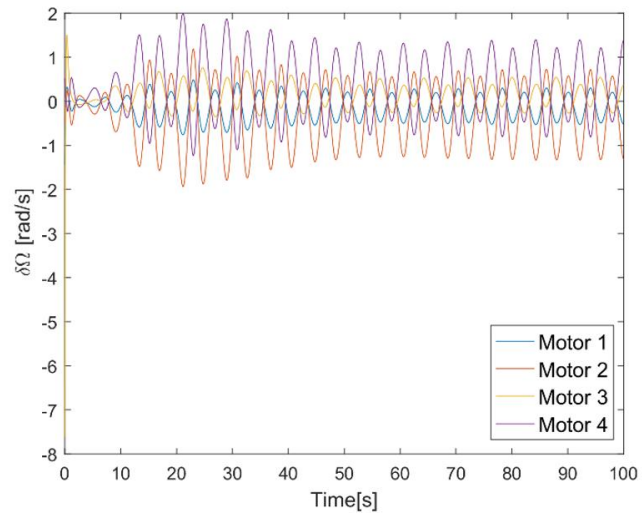


**Figure 5.33 - Rotor angular speed variation when the multi-rotor has no tilting mechanism for a sinusoidal input on x direction.**

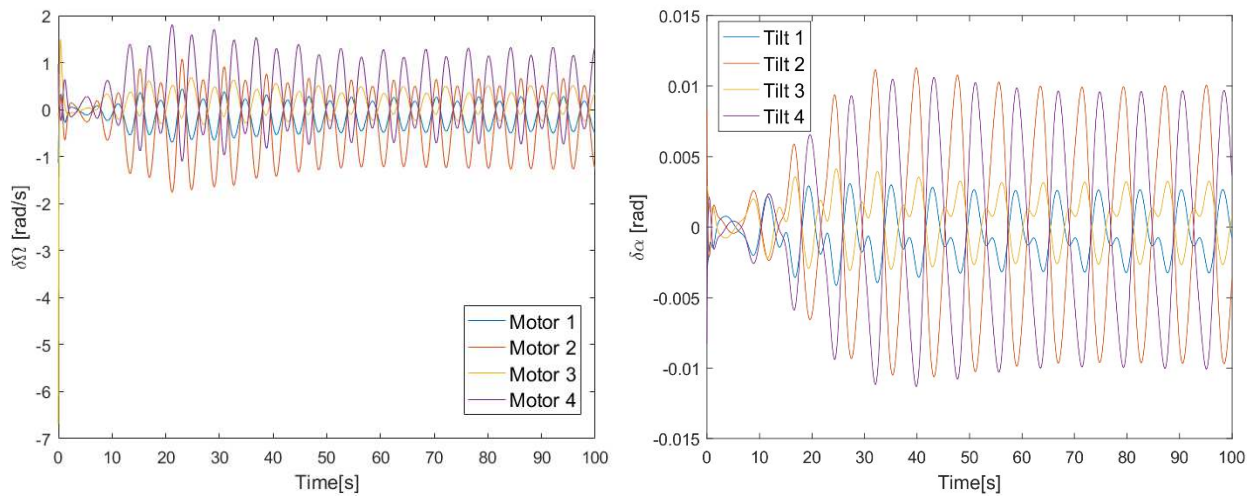


**Figure 5.34 - Rotor angular speed (left) variation and tilt angle (right) when the multi-rotor has longitudinal tilting mechanism for a sinusoidal input on x direction.**



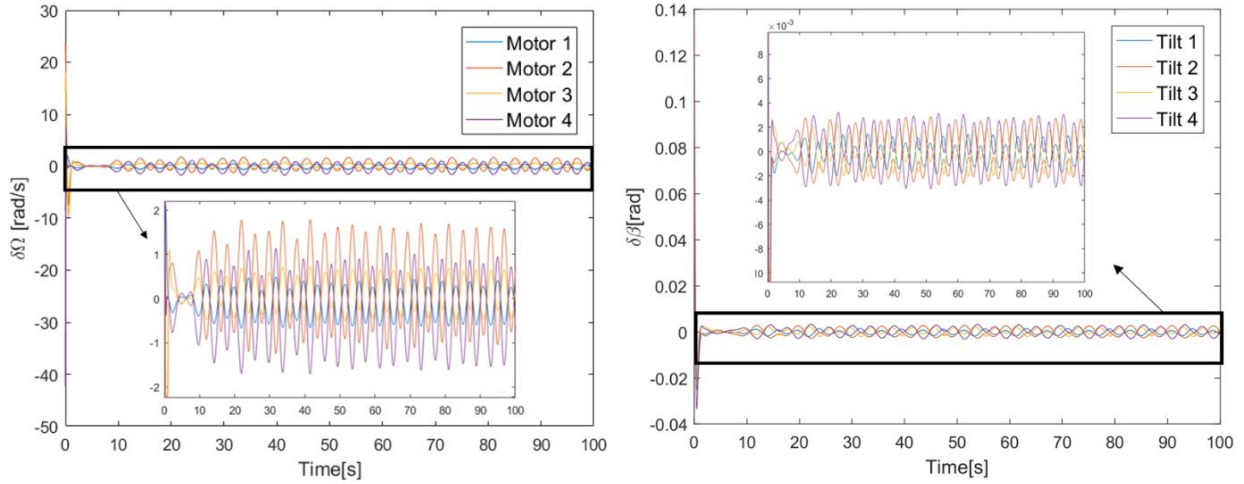


**Figure 5.35 - Rotor angular speed (left) variation and tilt angle (right) when the multi-rotor has lateral tilting mechanism for a sinusoidal input on x direction.**

Also, once again, the system response on the  $y_E$  direction is expected to be the same due to the multi-rotor symmetry. Furthermore, the controller is not able to stabilize the response for a sinusoidal input on the  $z_E$  direction with the same gain matrix.

Later, a circular trajectory reference signal on  $x_E - y_E$  plane is tested considering the designed controller for the sinusoidal input. On this case, the initial yaw angle is set as zero. The circular reference equations on time domain are presented below:

$$r_x(t) = A_{0x} \sin(\omega_{0x}t + \varepsilon_{0x}) \quad (5.4.2)$$

$$r_y(t) = A_{0y} \sin(\omega_{0y}t + \varepsilon_{0y}) \quad (5.4.3)$$

$$r_z(t) = 0 \quad (5.4.4)$$

In order to complete a circle, the parameters are set as  $\omega_{0x} = \omega_{0y} = 0.796$  rad/s,  $\varepsilon_{0x} = \pi/2$  rad and  $\varepsilon_{0y} = 0$ . The multi-copter state responses are presented on Figs 5.36 and 5.37.

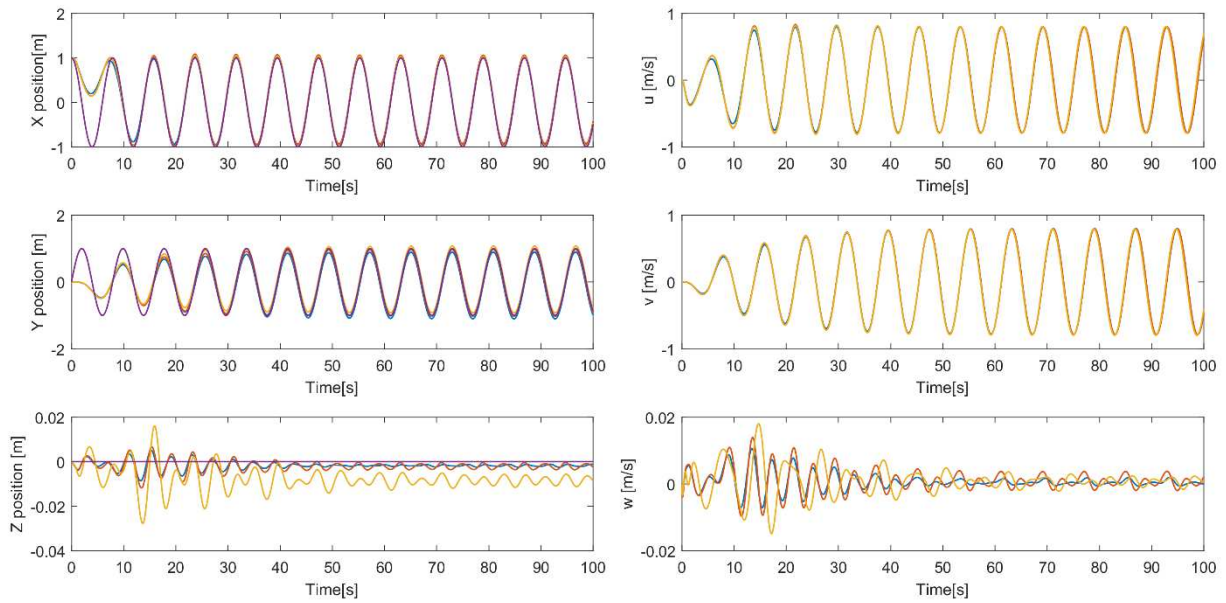


**Figure 5.36 - Multi-copter position (left) and velocity (right) for a sinusoidal input signal (purple) on the x and y directions for 3 different configurations: no tilt (blue), 4 longitudinal tilting mechanisms (red) and 4 lateral tilting mechanisms (yellow).**

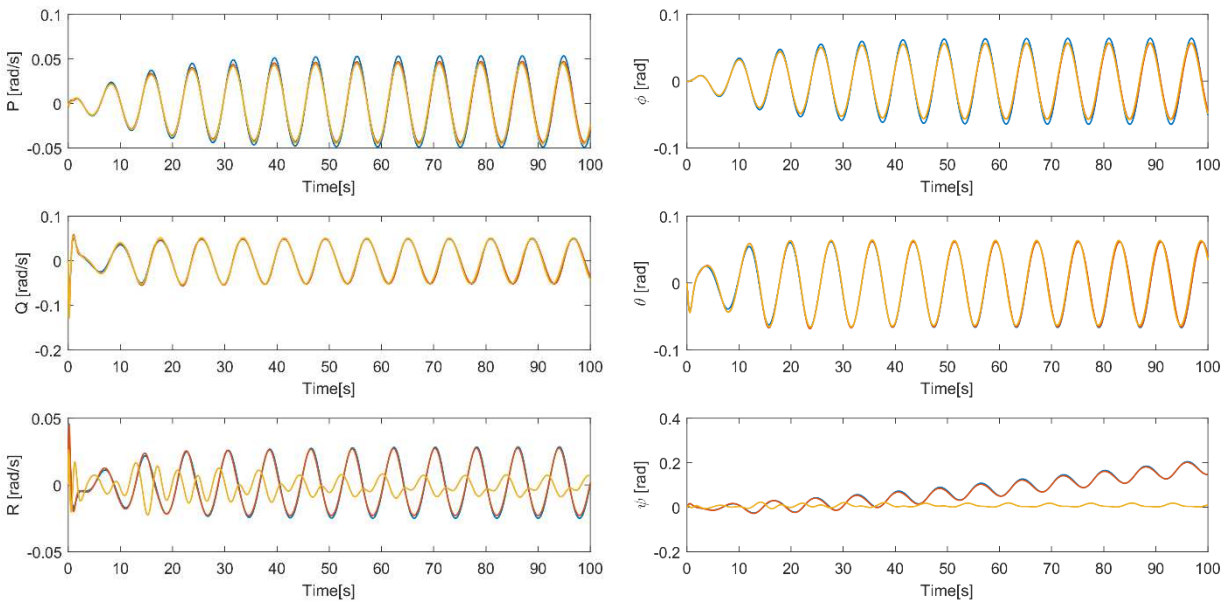


**Figure 5.37 - Multi-copter angular velocity (left) and position (right) for a sinusoidal input signal (purple) on the x and y directions for 3 different configurations: no tilt (blue), 4 longitudinal tilting mechanisms (red) and 4 lateral tilting mechanisms (yellow).**

Regarding Fig. 5.36, it is evident that the system response with the longitudinal and none tilting mechanism are quite the same except for the fact that the position amplitude on  $x_E$  and  $y_E$  directions are closer to the reference for the longitudinal tilt case. Whereas, the response for the lateral tilting mechanism has higher oscillations on  $z_E$  direction but it tends to converge to the steady state response more quickly. Also, the amplitude for the last case is even closer to the reference signal.

Further, observing the angular velocity and the Euler angles values from Fig. 5.37, it can be observed that the oscillations amplitudes are smaller for the system with lateral tilt mechanism, principally the  $R$  angular velocity. Additionally, the yaw response for when the system has none or a longitudinal tilting mechanism has an ascending oscillation while for the lateral case it keeps around zero. The ascending oscillation can be a prediction of instabilities as  $t \rightarrow \infty$ .

Figures 5.38, 5.39 and 5.40 shows the input control variation for all three simulated cases. Comparing the rotor speed variation amplitude for the no tilt (Fig. 5.38 left) and 4-lateral tilt mechanism (Fig. 5.40) it can be noted that the lateral case has higher amplitudes. Once again, the rotor angular speed variation is similar for non-tilt and 4-longitudinal as is the tilt angle amplitude variation for the longitudinal and lateral tilting mechanism.

However, analyzing the states response from Figs. 5.36 and 5.37, it can be concluded that the lateral tilting mechanism is much more effective than the other one since it can keep the yaw angle stable and also converges to the steady state response faster.

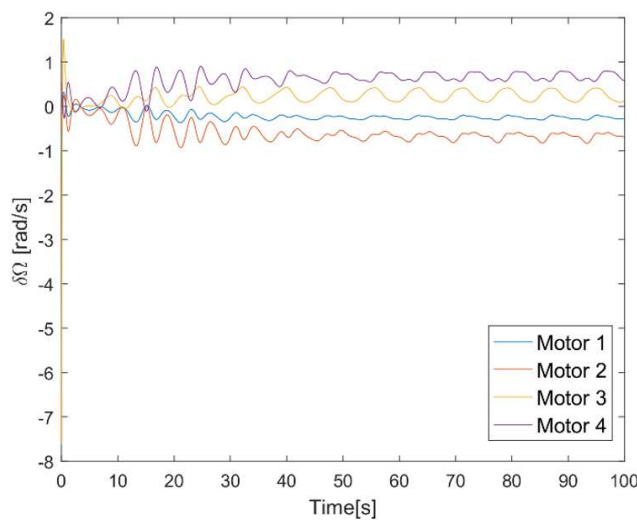


**Figure 5.38 - Rotor angular speed variation when the multi-rotor has no tilting mechanism for a sinusoidal input on x and y directions.**

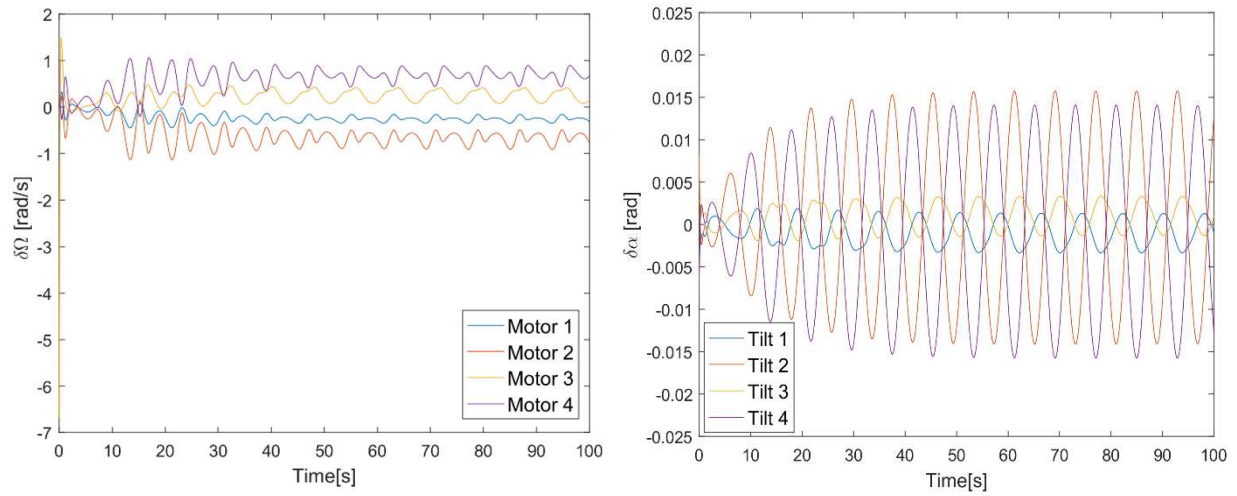


**Figure 5.39 - Rotor angular speed (left) variation and tilt angle (right) when the multi-rotor has longitudinal tilting mechanism for a sinusoidal input on x and y directions.**

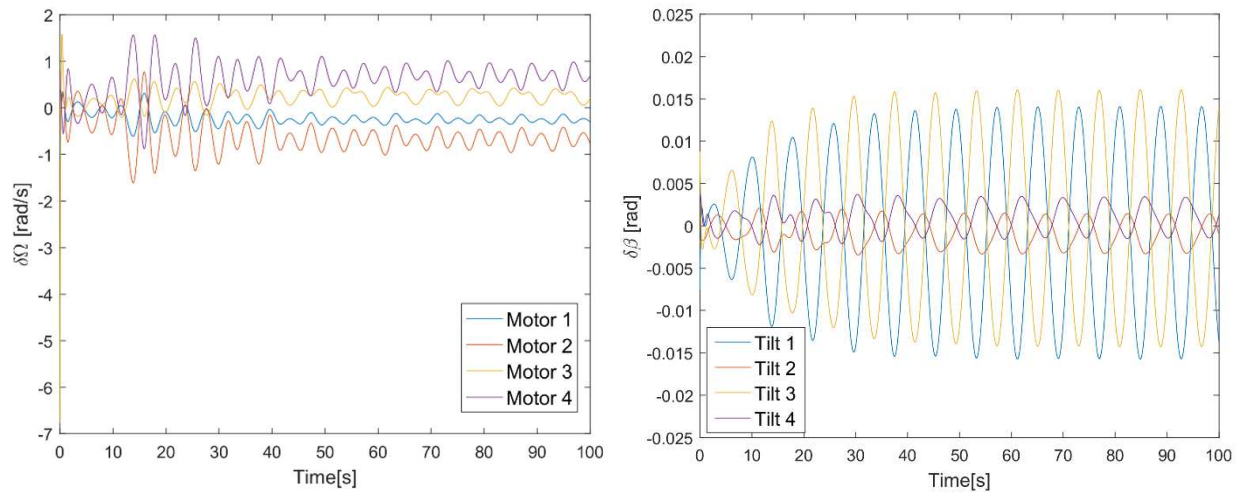


**Figure 5.40 - Rotor angular speed (left) variation and tilt angle (right) when the multi-rotor has lateral tilting mechanism for a sinusoidal input on x and y directions.**

Lastly, Fig. 5.41 illustrates the multi-copter 3D space trajectory when the system is equipped with the lateral tilting mechanism. Since the responses are close to each other, the same result is expected. This picture gives a good overview how the system is able to start from the  $x_E = 1, y_E = 0, z_E = 0$  position and reach the circular steady state trajectory.

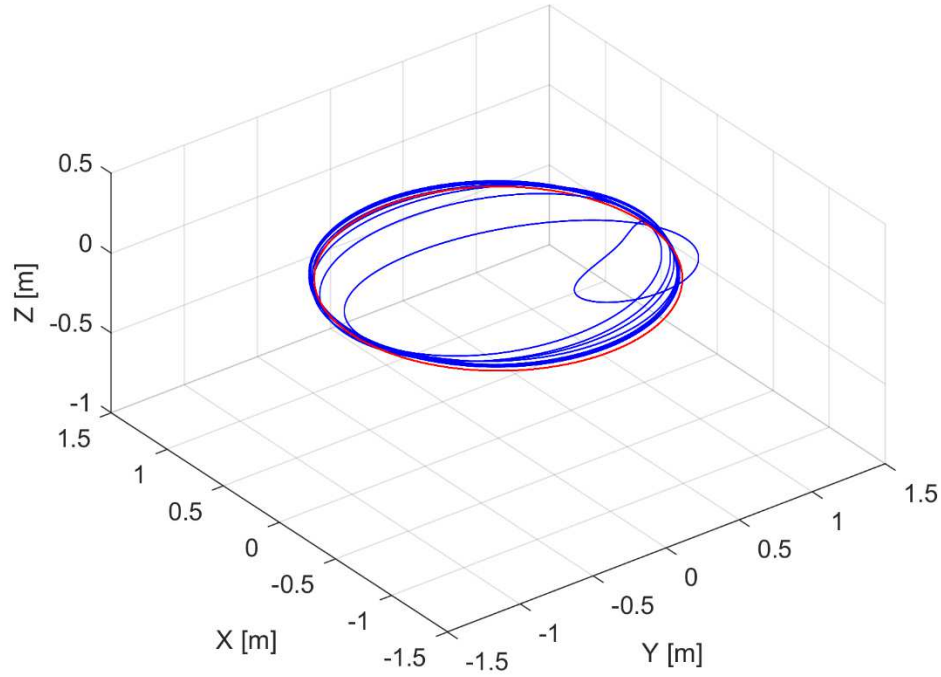


Figure 5.41 - 3D space trajectory for the multi-copter with 4-lateral tilting mechanism (blue) and 3D reference (red).

### 5.5 Random Space Trajectory

After testing the controller stability for three custom reference input signals, the controller is tested for a random 3D space trajectory. The desired reference input signal is a combination of ramp and step inputs as presented on Fig. 5.42. The signal is composed of an ascending-descending ramp input on  $x_E$  direction, an ascending step input on  $y_E$  direction and a step/ascending ramp/descending ramp on  $z_E$  direction. Consequently, for  $x_E$  and  $z_E$  directions the controller is designed as a second order and first order for  $y_E$  direction. The weighting matrices values are chosen the same as the ramp input controller (Eqs. (5.3.1), (5.3.2) and (5.3.3)). Once more, the simulations are made for the no tilt, 4-longitudinal and 4-lateral tilt scenarios.

Regarding the system response for nominal conditions, it can be concluded that they are very similar for the three actuation systems. Thus, on this case a different initial condition is tested ( $\psi = \pi/4$  rad) for all scenario in order to evaluate the multi-copter behavior.

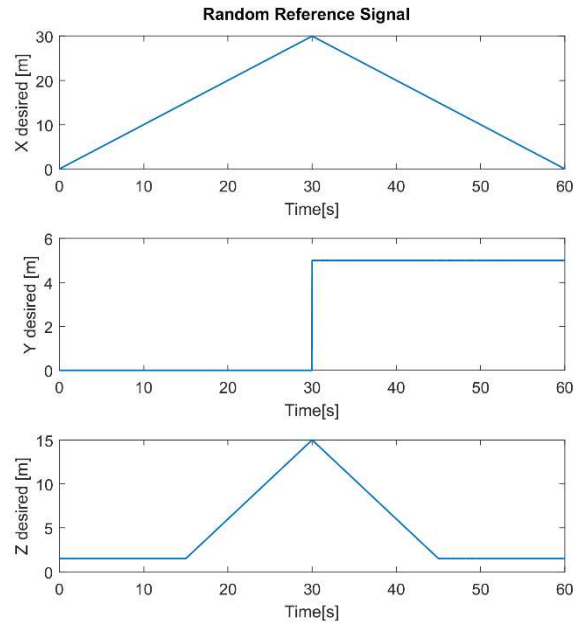
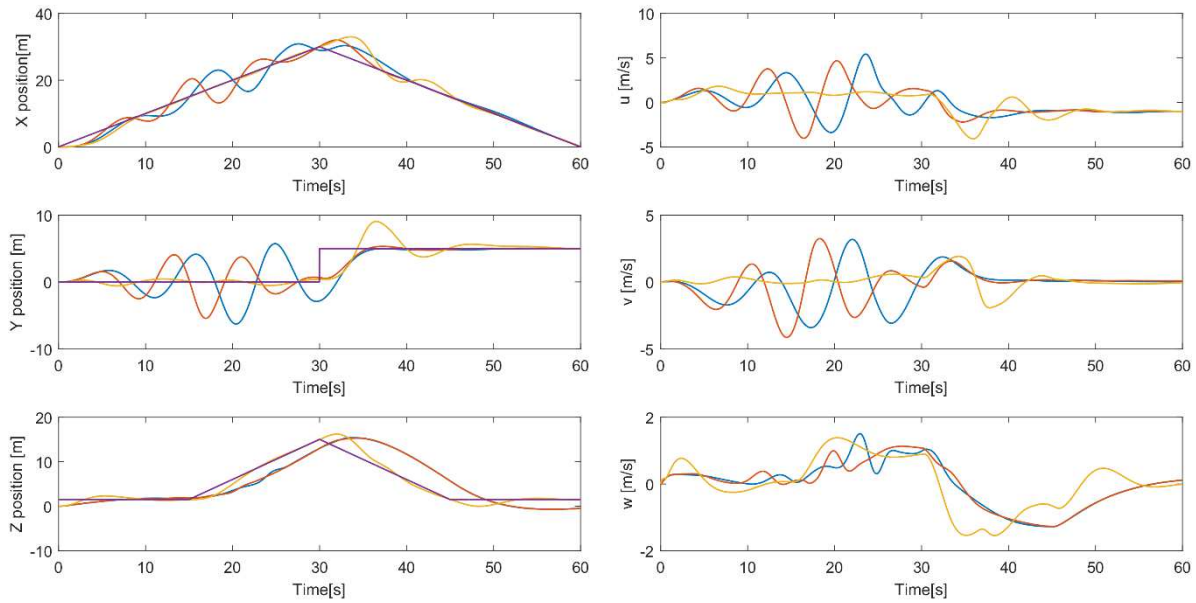


Figure 5.42 - 3D trajectory input signal.

The system state responses are illustrated on Figs. 5.43 and 5.44 while the 3D trajectory for the three cases is illustrated on Fig. 5.48. From Fig. 5.43 (left) it can be clearly seen that the system with 4-lateral tilting mechanism has lower oscillations around the reference signal; hence, it can track the signal with better precision. The oscillations are also seen on the linear (Fig. 5.43 right), angular velocities (Fig. 5.44 left) and Euler angles (Fig. 5.44 right). Thus, the system with the lateral tilting mechanism is able to correct the attitude and complete the trajectory satisfactorily.

Further, regarding the control input signals on Figs. 5.45, 5.46 and 5.47, it can be noted that the system containing the lateral tilt mechanism (Fig. 5.46) has higher values of angular velocity and tilting angles than the other two cases. On the other hand, the multi-copter equipped with the lateral tilt mechanism (Fig. 5.47) has lower angular velocity values compared to the system with no tilt (Fig. 5.45). This behavior is mainly due to the yaw angle correction. Since the yaw angle control is more effective for the tilt rotation than angular speed variation, the system with lateral tilt mechanism can stabilize the yaw rotation more quickly, so the other states responses are less affected. Finally, the effectivity of the tilt angle is observed on the tilt angle amplitude signal on Fig. 5.47 (right). With small values of tilting angle, the system is capable to effectively keep the yaw angle and angular rate stable, enhancing the system stability through the trajectory.





**Figure 5.43 - Multi-copter position (left) and velocity (right) for a 3D random input signal (purple) on the x y and z directions for 3 different configurations: no tilt (blue), 4 longitudinal tilting mechanisms (red) and 4 lateral tilting mechanisms (yellow).**

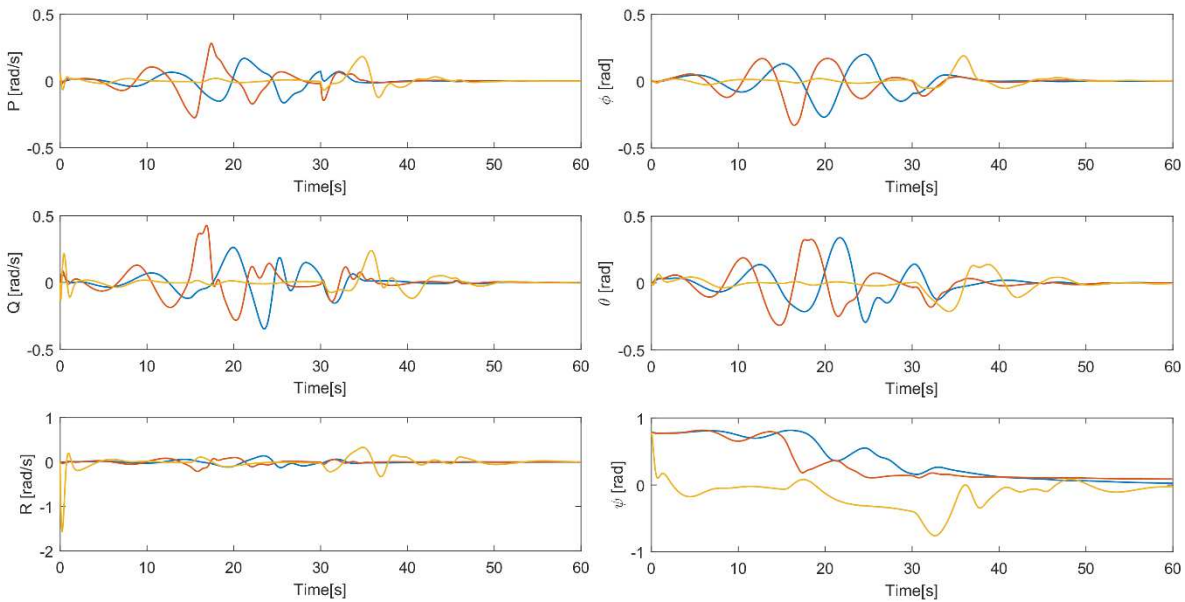


**Figure 5.44 - Multi-copter angular velocity (left) and position (right) for a 3D random trajectory (purple) on the x, y and z directions for 3 different configurations: no tilt (blue), 4 longitudinal tilting mechanisms (red) and 4 lateral tilting mechanisms (yellow).**

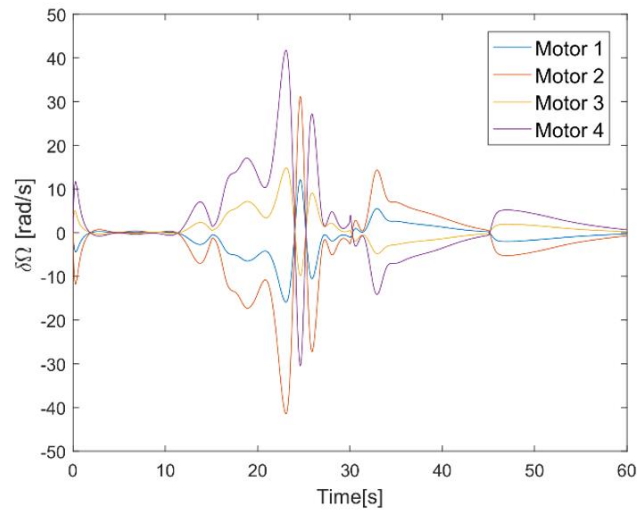


**Figure 5.45 - Rotor angular speed variation when the multi-rotor has no tilting mechanism for a 3D random input signal on x, y and z directions.**

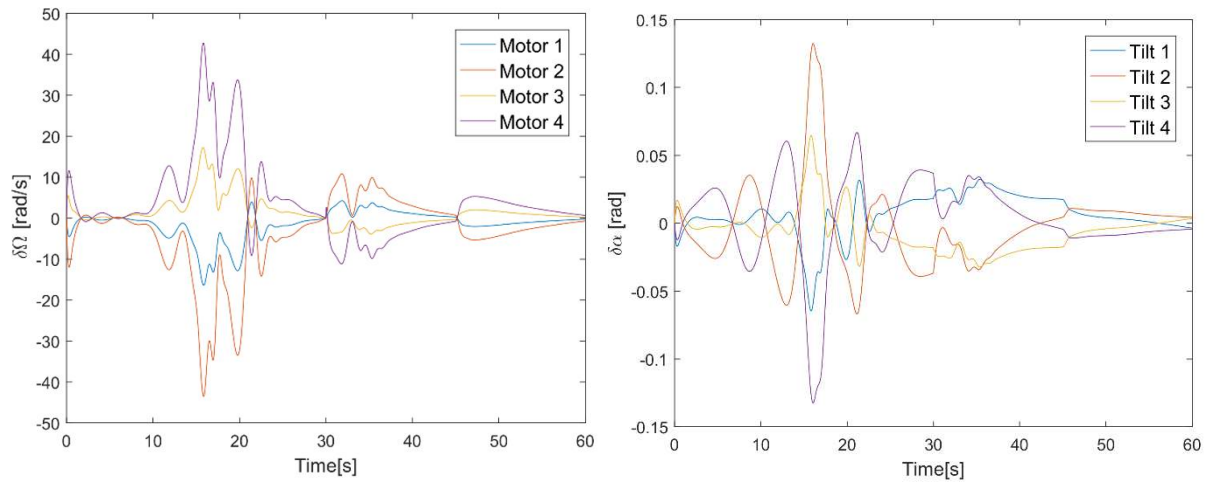


**Figure 5.46 - Rotor angular speed (left) variation and tilt angle (right) when the multi-rotor has longitudinal tilting mechanism for a 3D random input signal on x, y and z directions**



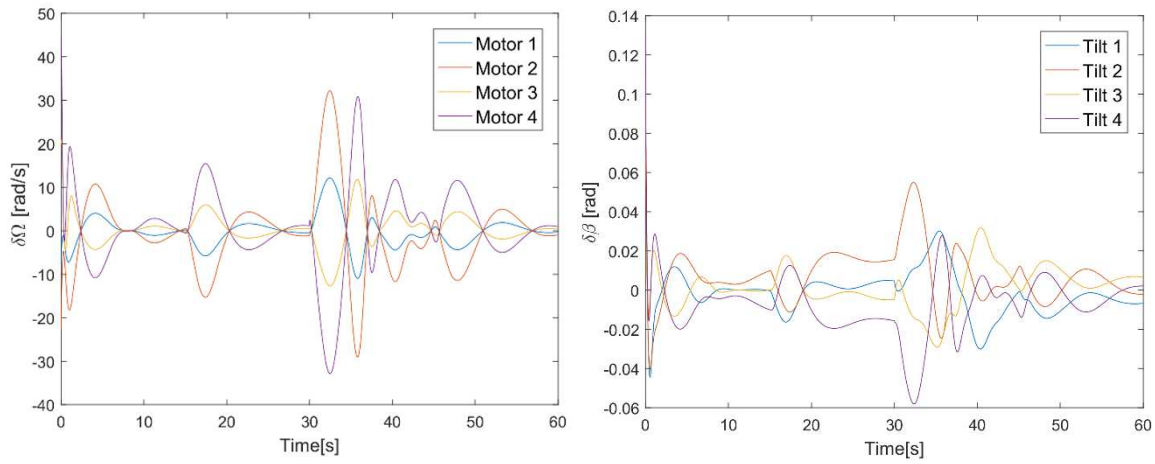


**Figure 5.47 - Rotor angular speed (left) variation and tilt angle (right) when the multi-rotor has lateral tilting mechanism for a 3D random input signal on x, y and z directions.**

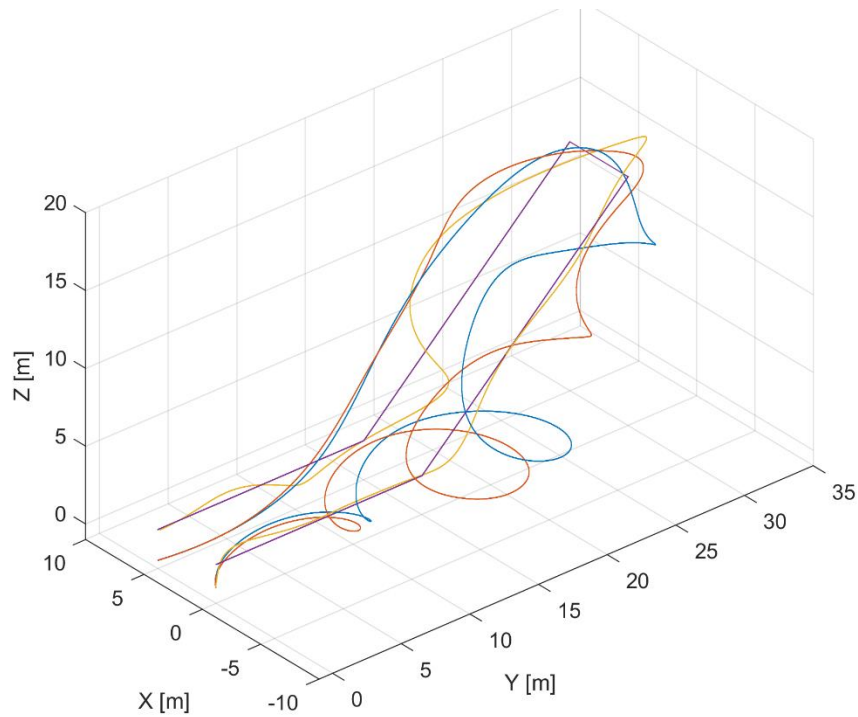


**Figure 5.48 - 3D random trajectory on x, y and z directions (purple) for 3 different configurations: no tilt (blue), 4 longitudinal tilting mechanisms (red) and 4 lateral tilting mechanisms (yellow).**

Figure 5.48 gives a better overview on how the system behaves for the three different simulated scenarios. As previously discussed, the trajectory executed by the multi-copter having the lateral tilting mechanism is closer to the reference and is the only one to reach the final desired

point. Also, it is noted that the aircraft make some loops for the no tilt and longitudinal tilt cases. This enhances the idea that the multi-copter controller is trying to correct its yaw angle along the trajectory.

## 5.6 Conclusions and Highlights

All the simulations and analysis made through this chapter gives a hint on how the addition of a tilt rotor actuation system on a multi-rotor can influence the system stability. Firstly, it was noted that the system with no tilting mechanism does not accomplish the controllability requirements which can compromise the Ricatti equation solution and the steady state response. As discussed, the non-controllability of the system has a relation with the yaw angle dynamics since the angular speed variation effect on the yaw moment is too slow. It was detected that including a lateral tilt mechanism to the system can make the system completely controllable since the yaw response due to the tilt rotation is much faster. This yaw angle controllability influence is evident on time responses simulations, principally on the 3D random trajectory case where the system with lateral tilt mechanism was able to correct its attitude without compromising other states.

Also, since the problem is not well posed, the choice of the weighting matrices is very sensitive since that even if a solution for the Ricatti equation is found, the non-linear system response can diverge on time. This behavior is mostly caused since the linear model, on which the controller design is based, is very simplified compared to the non-linear; thus, some effects are not accounted on the controller design. Consequently, when the tilt mechanisms are added to the system they the gyroscopic effects tend to have a major contribution to the system as presented on Chapter 2. Furthermore, through the simulations experience, it was noted that, due the model linearization, the operational range of the multi-copter is limited, i.e. it works only for small amplitude reference signals and, consequently, small velocities, angular rates and attitude angles.

The tilting mechanism addition affected also the poles and zero positions of the closed-loop system considering the same weighting matrices. In general, when equipped with the tilt mechanism, the poles shift to a further position from the origin on the Real/Imaginary axis as shown on Figs. 5.2, 5.3 and 5.22. Thus, it is expected the system to respond faster. Moreover, similarly to the type of tilting mechanism, the number of tilting mechanism on the multi-copter has also affected the poles position. Further, when having an even number of tilting mechanism or having a pair of actuators that is not opposed, the system response was not able to converge in time. Mainly because the effects are not compensated increasing the non-linear effects contribution.

Furthermore, it was also detected that the closed-loop system has zeros on the right half of the Real/Imaginary plane known as *non-minimum phase zeros*. These zeros can have a major

influence on the steady state response since that, even the system reaching the dynamical equilibrium (zero forces and moments) the plant input signal tends to amplify as one of the states grow. This phenomenon was very clear when analyzing the time response for a ramp input signal (Figs. 5.25, 5.27 and 5.28).

Moreover, it was concluded that for some trajectories as the ascending unit step (Fig. 5.12), the addition of the tilt mechanism made the system behave worst. On this case, the task could be accomplished only using the rotor mechanism but, as the controller is designed, the tilt mechanism is actioned and the multi-copter shifts its position on the other two directions spending more control effort and going closer to the instability region. Nevertheless, for the sinusoidal and 3D random input trajectory, the system with the lateral tilt has shown some enhancements since it was able to control the yaw angle effectively. It is also important to state that better results could be achieved choosing other weighting matrices but, for sake of comparing the system behavior, the matrices were held varying only the actuation mechanism.

Lastly, an adaptive control law could be proposed to profit from the tilt mechanism benefits and also the response characteristic for each input signal. For instance, when a 3D trajectory requires high values of  $z_E$  displacement, the rotors angular velocities should predominate while the tilt mechanism should actuate to correct the attitude position. Also, for long distances travels, the trajectory could be described as a combination of ramp inputs and the second order controller used while the first order could operate for final position correction.

## Chapter 6

### General Conclusion

This chapter contains a brief review of the main contributions of this work, followed by an outlook on future work trying to identify possible upcoming steps to implement the tilting mechanism on a real *MAV* aircraft.

#### 6.1 Overview

The UAV crescent demand on civilian applications during the last years has accelerated incredibly the development of new technologies. Among the UAV aircrafts, the multi-copters have attracted the attention of researchers and community due to their simple mechanics, cost, and their ability to operate autonomously on restricted space environment. Even though there is a large diversity of aircrafts on this class available, there still have some features which can be improved such as: higher endurance, range, better maneuverability and stability.

It is in this context that a non-standard actuation device was proposed in this work, which is the tilting mechanism, giving to the motor propulsive set the ability of rotating about the multi-copter arm longitudinally or laterally. Thus, the system has more control inputs and, as discussed on Chapter 1, the multi-copter underactuation problem can be solved.

#### 6.2 Dynamical Model

An important part of the project was to derive the dynamical model for a multi-copter including the new actuation system considering its physical effects. The equations are derived for a generic configuration and is validated for different tilting mechanisms, structural configuration and mechanical properties. From the developed equations, the addition of tilting mechanisms to the model (either longitudinal or lateral) have a main contribution to the gyroscopic effect which

is sometimes neglected for standard multi-copters. As presented in Chapter 2, the addition the tilting rotors increases the non-linearity level of the external forces acting on the aircraft. Furthermore, the thrust force produced by the spinning propellers can be vectorized on the three directions of the *BCS* giving the aircraft the ability to have an equilibrium position different from hover flight.

Finally, the aircraft equations of motion were linearized around a trimming equilibrium condition so they could be written on state-space format. The model linearization around a hover flight condition has many implications on the control design since the simplifications made hide many of the non-linear effects from the dynamical model. On this manner, the aircraft operational conditions become limited since any condition out the linear region can destabilize the system.

Once the equations of motions were written on state-space model, the modern control techniques can be applied considering the aircraft as a multiple-input multiple-output-system.

### 6.3 Control Design

Regarding the control design, the Linear Quadratic Tracking control technique was chosen for this work since it was desirable that the aircraft is able to follow a given reference trajectory. Then, the control law was derived considering the system as a servomechanism model, so that the control order could be chosen based on the reference input differential equation. The controller gains are calculated from a minimization problem using the Riccati equations in such manner that all the control gains are calculated simultaneously guaranteeing global stability.

The Riccati equations solutions are function of the chosen weighting matrices which will prescribe the time domain system behavior. Their choice can become a hard task since the chosen values may result in a gain combination that makes the system unstable.

### 6.4 The Multi-copter

The object of study on this work is a quad-copter multi-rotor aircraft developed in the Laboratório de Aeronaves Autônomas from the Federal University of Uberlândia. The multi-copter already contains all the required structure to perform flights, however, the control laws are still in development.

It was also designed a tilting mechanism which can be easily attached to the aircraft. The device consists on a longitudinal tilting mechanism having a support bed where the motor set can be installed. The whole set is driven by an actuator fixed to the multi-copter's arm. The system has already been tested but not during flight yet.

An important concern on installing the tilting mechanism is that some microcontrollers, such as the Raspberry Pi, does not have sufficient PWM outputs to control all the motors and actuators together. Thus, the Beaglebone microcontroller was chosen where the control laws are being compiled.

In conclusion, the multi-copter is being design and developed by the group in such manner that all the design, control and signal acquisition parameters can be controlled.

## 6.5 Simulations

Finally, the dynamical equations and control applications could be evaluated via numerical simulations. They were conducted using a Matlab/Simulink environment where different actuation mechanisms and reference input signals could be tested. This task has utter importance before applying the control law on the real system since it must be guaranteed that the system will behave steadily and the response converges.

Hence, firstly the controllability and observability of the state-space model were checked for different actuation mechanisms. The results have shown that the system containing none or longitudinal tilting mechanism could not accomplish to the controllability condition differently from the lateral tilt mechanism case. It was also noted that the uncontrollability is related with the yaw movement dynamics principally due to its slow time response to propeller angular speed variation. Thus, for the cases with none and longitudinal tilting mechanism, the yaw states equations (for  $P$  and  $\psi$ ) were removed from the state-space system so that the controllability conditions were then fulfilled; and a PID controller was designed separately so that the yaw angle could be controlled to keep stability.

Later, the pole and zero mapping has show that the LQR solution was able to find stable closed loop poles (poles on left half of the Real/Imaginary plane) for all situations considered for tilting mechanisms or signal input. However, some of the solutions have placed some zeros on the right half plane, principally when the system is equipped with tilt mechanism, a phenomenon known as *non-minimum phase zeros*. This effect was clearly observed for the ramp reference input simulations. On this case, only the multi-copter equipped with the tilting mechanism had *non-minimum phase zeros* and, observing their time response, it was able to note that the control input signals raised up as the aircraft was following the linear increasing reference signal even that the system was dynamically stable.

Further, when tested the step inputs on  $x_E$  direction, the controller with both tilting mechanisms have shown to have a better performance. However, it operated awkwardly when an

ascending trajectory (step input on  $z_E$  direction) was set as a reference signal since the tilt mechanism actuation made the aircraft to have high lateral oscillations.

Through all the simulated trajectories the system containing the lateral tilt mechanism has shown to be more stable since it was capable to better control the yaw angle. This effect was better evidenced when the sinusoidal and random 3D trajectories containing an initial yaw angle drift were proposed. In conclusion, an aircraft containing a better actuation setup to control the yaw attitude angle can make the aircraft to operate more steadily.

Finally, regarding all the simulations performed, it can be stated that an optimized controller could be designed using the better characteristics from each configuration.

## 6.6 Future Work

For future works, the LQT control technique could be better explored for the tilt mechanism actuation in order to solve the *non-minimum phase* problem. Furthermore, other design control techniques can be tested and compared to the actual designed controller. Finally, an adaptive control could be designed based on a mission trajectory planner combining the different input signals and tilting mechanisms studied in this work.

Further, the control robustness for uncertain parameters and external disturbances could be studied in order to evaluate the system robustness. Hardware-in-the-loop simulations can also be performed in order check the controller behavior when applied on a discrete real microcontroller. Finally, once the control law is validated, it can be applied on a real multi-copter as described on Chapter 4.

## References

Aeroscout, "Aeroscout – Unmanned Aircraft Technology", Aeroscout. Source: <https://www.aeroscout.ch/>. Accessed in: February 7, 2017.

Amiri, N., Ramirez-Serrano, A. and Davies, R. "Modelling of Opposed Lateral and Longitudinal Tilting Dual-Fan Unmanned Aerial Vehicle", Proceedings of the 18th World Congress - The International Federation of Automatic Control, Milano, Italy, 2011.

Asselin, M., 1965. An Introduction to Aircraft Performance. Reston, Virginia: AIAA.

Badr, S., Mehrez, O. and Kabeel, A. E., "A Novel Modification for a Quadrotor Design", International Conference on Unmanned Aircraft Systems (ICUAS), IEEE, 2016. <https://doi.org/10.1109/ICUAS.2016.7502536>

Barnard Microsystems, "Barnard Microsystems – Selection of UAVs", Barnard Microsystems, 2014. Source: [http://www.barnardmicrosystems.com/UAV/uav\\_list/uav\\_list.html](http://www.barnardmicrosystems.com/UAV/uav_list/uav_list.html). Accessed in: February 7, 2017.

Bellman, R.E. Dynamic Programming. Dover, Mineola, 2003

Bouabdallah, S. "Design and Control of Quadrotors with Application to Autonomous Flying". PhD Thesis, École Polytechnique Fédérale de Lausanne, 2007.

Bouabdallah, S. "PID vs LQ Control Techniques Applied to an Indoor Micro Quadrotor", International Conference on Intelligent Robots and Systems, IEEE/RSJ, Sendai, Japan, 2004. <https://doi.org/10.1109/IROS.2004.1389776>

Bristeau, P., Martin, P., Salaun, E. and Petit, N. "The Role of Propeller Aerodynamics in the Model of a Quadrotor UAV", European Control Conference, 2009.

Brown, E., "BeagleBone Green drops the HDMI....and the price", 2015. Source: <http://linuxgizmos.com>. Accessed in: 1/24/2018.

Burns, R. S. Advanced Control Engineering. Oxford: Plant a Tree, 2001



Business Insider. "The Drones Report: Market Forecasts, Regulatory Barriers, Top Vendors, and Leading Commercial Applications", Business Insider, < <http://www.businessinsider.com/uav-or-commercial-drone-market-forecast-2015-2>>. 17. Accessed in: February 9 2017.

Cai, G., Chen, B. M., Lee, T. H. e Dong, M. "Design and implementation of a hardware-in-the-loop simulation system for small-scale UAV helicopters". Elsevier, Mechatronics, 2009.

Cheeseman, I. C. and Bennett, W.E. "The Effect of The Ground on a Helicopter Rotor in Forward Flight", A.R.C R&M, 3021, 1995.

Costa, A. V. O. Projeto Estrutural e Contrução do Braço de um Multirrotor. Trabalho de Conclusão de Curso - Universidade Federal de Uberlândia, Uberlândia, 2016.

Cutler, M., Ure, N. K., Michini, B. and How, J. P. "Comparison of fixed and variable pitch actuators for agile quadrotors", American Intitute of Aeronautics and Astronautics (AIAA), Portland, Oregon, USA, 2011.  
<https://doi.org/10.2514/6.2011-6406>

Davidson, E.J., Copeland, B. "Gain margin and time lag tolerance constraints applied to the stabilization problem and robust servomechanism problem". IEEE Transactions on Automatic Control 30(3), 229–239, 1985.  
<https://doi.org/10.1109/TAC.1985.1103924>

Direct Industry, "Hexa-copter UAV / inspection/ foldable", Skeyetech. Source: <http://www.directindustry.com/prod/skeyetech-sas/product-183168-1906221.html>. Accessed in: 20, 2018.

Fogelberg, J. "Navigation and Autonomous Control of a Hexacopter in Indoor Enviroments". Msc Thesis, Lund University, Lund, Sweden, 2013.

FPV, "Types of Multicopters – The Baiscs", The FPV NZ. Source: <https://thefpvnz.wordpress.com/types-of-multicopters-the-basics/>. Accessed in: February 20, 2018.

Francis, B.A., Wonham, W.M.: "The internal model principle of control theory". Automatica 12(5), 457–465, 1976.  
[https://doi.org/10.1016/0005-1098\(76\)90006-6](https://doi.org/10.1016/0005-1098(76)90006-6)

Giribet, J. I., Sánchez-Pe-a, R. S. and Ghersin, A. S. "Analysis and Design of a Tilted Rotor Hexacopter for Fault Tolerance". IEEE Transactions on Aerospace and Electronics Systems, Vol.52, NO. 4, pg. 1555 to 1567, 2016.

Hintz, C., Torno, C. and Carrillo, L. R. G. "Design and Dinamic Modeling of a Rotary Wing Aircraft with Morphing Capabilities", International Conference on Unmanned Aircraft Systems (ICUAS), IEEE, Orlando, Florida, USA, 2014.

Hoagg, J. B. and Bernstein, D. S. "Nonminimum-phase-zeros -much to do about nothing - Revisited: Part II", IEEE Control System Magazine, vol 27, pp 45-57, 2007.  
<https://doi.org/10.1109/MCS.2007.365003>

Huang, H., Hoffmann, G.M. and Waslander, S. L., Tomlin, C. J. "Aerodynamics and Control of Autonomous Quadrotor Helicopters in Aggressive Maneuvering", International Conference on Robotics and Automation, IEEE, 2009.  
<https://doi.org/10.1109/ROBOT.2009.5152561>

Introbotics, "5 of the Best Examples How to Build a DYP Quadcopter", Introbotics, September 24, 2013. Source: <http://www.intorobotics.com/5-best-examples-of-how-to-build-a-diy-quadcopter/>. Accessed in: February 20, 2018.

K. Nonami, M. Kartidjo, K. J. Yoon and A. Budiyo, Autonomous Control Systems and Vehicles Intelligent Unmanned Systems, Springer, Japan, 2013.  
<https://doi.org/10.1007/978-4-431-54276-6>

Kalman, R. "On the General theory of control Systems". Proceedings of the First International Congress IFAC: Automatic and Remote Control (pp. 481-492.. London: Butterworth & Co, 1961.

Kendoul, F., Fantoni, I. and Lozano, R. "Modeling and Control of a Small Autonomous Aircraft Having Two Tilting Rotors", IEEE Transactions on Robotics, IEEE, Vol. 22, DOI: 10.1109/TRO.2006.882956, 2006.  
<https://doi.org/10.1109/TRO.2006.882956>

Kumar, A., "Single Board Computers – Rapberry Pi vs BeagleBone vs Arduino", 2015. Source: <http://www.thewindowsclub.com>. Accessed in: 1/24/2018.

Lavretsky, E. and Wise, K. A. Robust and Adaptive Control. London: Springer, 2013  
<https://doi.org/10.1007/978-1-4471-4396-3>

Marques, F. M. M. Modelagem, Simulação e Controle de uma Aeronave Multirrotoira, Monografia, Universidade Federal de Uberlândia, Uberlândia, MG, Brasil, 2016.

Oosedo, A., Abiko, S., Narasaki, S., Kuno, A., Konno, A. and Uchiyama M. "Flight Control System of a Quad Tilt Rotor Unmanned Aerial Vehicle for a Large Attitude Change". International Conference on Robotics and Automation, IEEE, Seattle, Washington, USA, 2015.  
<https://doi.org/10.1109/ICRA.2015.7139508>

Pines, D. and Bohorquez, F. "Challenges facing future micro air vehicle development," AIAA Journal of Aircraft, vol. 43, no. 2, pp. 290–305, 2006.  
<https://doi.org/10.2514/1.4922>

Rade, D. L. Cinemática e Dinâmica para a Engenharia. Uberlândia, MG: UFU, 2009

Raffo, G. V., Ortega, M. G. and Rubio, F. R. "Backstepping/Nonlinear H control for Path tracking of a Quadrotor Unmanned Aerial Vehicle", American Control Conference, 3356-3351, 2008.

Rajappa, S., Ryll, M., Bulthoff and H. H., Franchi, A. "Modeling, Control and Design Optimization for a Fully-actuated Hexarotor Aerial Vehicle with Tilted Propellers", International Conference on Robotics and Automation (ICRA), Seattle, Washington, USA, 2015.

Ramp, M. and Papadopoulos, E. "On Modeling and Control of a Holonomic Vectoring Tricopter", International Conference on Intelligent Robots and Systems (IROS), IEEE, Hamburg, Germany, 2015.

<https://doi.org/10.1109/IROS.2015.7353443>

Rich, M. "Model Development, System Identification, and Control of a Quadrotor Helicopter", Msc Thesis, Ames, Iowa, USA, Iowa State University, 2012.

Roskam, J. "Airplane Flight Dynamics and Automatic Flight Controls", DAR Corporation, Lawrence, KS, USA, 2001.

Ryll, M., Bulthoff, H. H. and Giordanno, P. R. "Modeling and control of a quadrotor UAV with Tilting Propellers", International Conference on Robotics and Automation (IEEE), Saint Paul, Minnesota, USA, 2012.  
<https://doi.org/10.1109/ICRA.2012.6225129>

Stevens, B. L. & Lewis, F. L., 1992. Aircraft Control and Simulation. New York: Wiley-Interscience .

Suiçmez, E. C. "Trajectory Tracking of a Quadrotor Unmanned Aerial Vehicle (UAV) Via Attitude and Position Control", Msc Thesis, Middle East Technical University, 2014.

Techject, "The Dragonfly – Biologically inspired UAV", Techject Inc. Source: <http://techject.com/robot-dragonfly/>. Accessed in: February 20, 2018.

Thielicke, W., "Shrediquette – the award-winning multi-totors by William Thielicke", Srediquette blogspot, December 22, 2017. Source: <http://shrediquette.blogspot.com.br/>. Accessed in: February 20, 2018.

Trimble, "Trimble UX5 Aerial Imaging Solution for Agriculture", Trimble. Source: <http://uas.trimble.com/ux5>. Accessed in: February 7, 2017.

Vairdo, "Barinbox: Sensing, Computing and Control – Lunch of the Brainbox", January 22, 2016. Source: <https://vairdo.wordpress.com/2016/01/22/launch-of-the-brainbox/>. Accessed in: February 20, 2018.

Valavanis, K. P. "Advances in Unmanned Aerial Vehicles". Ed. Springer, Dordrecht, Netherlands, 2007.

<https://doi.org/10.1007/978-1-4020-6114-1>

## Appendix A

### Motor Parameters

The motor propulsive group composed by the propeller, the rotor and an ESC “Electronic Speed Control” has been experimented in order to identify its dynamics and parameters, including the thrust factor force, using a test bench.

The test bench consists on a bending load cell fixed on a structure and an infrared sensor fixed on the bed where the rotor with the propeller and ESC are mounted. The propeller is equipped with a reflexive tape so that the infrared wave can be reflected. Then, the motor is attached 10 mm distance from the infrared sensor so that it is able to record the propeller rotational speed. A PIC PIC24FJ64GB002 microcontroller is used to set the PWM (Pulse Width Modulation) signal to the ESC and also receive the signal from the infrared sensor. The microcontroller has a 32MHz processor allowing a 100Hz sampling frequency for data acquisition via a Matlab connection.

Table A.1 summarizes the test bench specifications, and a schematic picture is illustrated on Fig. A.1 containing its components:

**Table A.1 - Test bench specifications.**

Equipment	Specifications
Rotor	DJI212/920KV
Propeller	26 cm diameter
ESC	MARK II E300 [30A]
Load cell	Maximum load: 5 [kg]

For the motor characterization, a steady state experiment is conducted in order to obtain the thrust force constant which relates the force produced by the spinning propeller with the rotor angular speed. The rotor angular speed rotation is set using a PWM input and the thrust value will

be considered as the value after its stabilization with a maximum variation of 1%. Then, the thrust force constant ( $k$ ) is obtained by the following relation:

$$T = k\Omega^2 \quad (\text{A.1.1})$$

Being  $T$  the thrust force and  $\Omega$  the propeller angular speed.

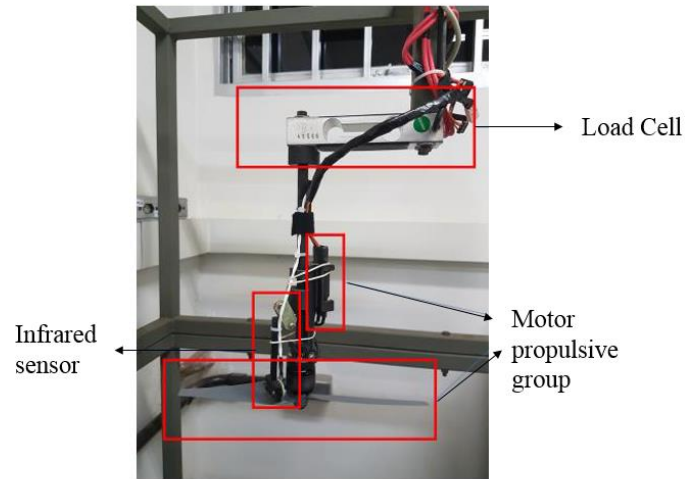


**Figure A1 Motor propulsive group test bench.**

The PWM tested range for the thrust force calculation was from 30% to 70% of its maximum value, allowing a propeller angular speed between 3000 and 7000 rpm. The experimental results are shown on Fig. A.2. The curve presented on Fig. A.2 was interpolated using a curving fitting method in order to determine the constant.

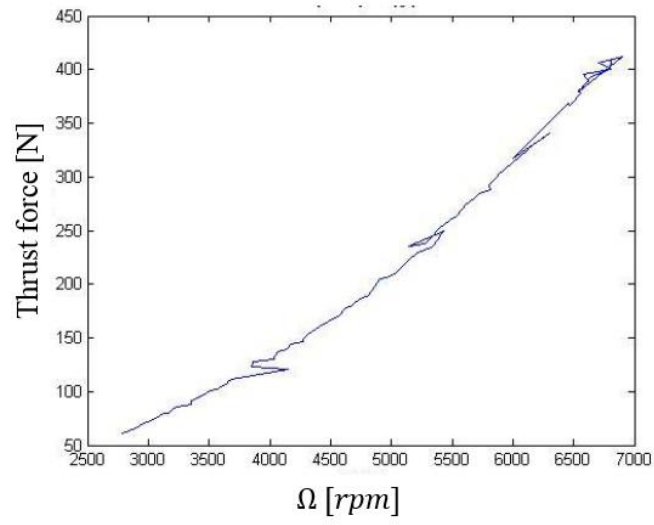


**Figure 2 Thrust vs rotor angular speed for  $k$  calculation.**

So, the thrust force coefficient obtained from the curve fitting is (in  $N/s^2$ ) :

$$k = 8.9013e-6 \quad (\text{A.1.2})$$